MEASUREMENTS OF MOLTEN STEEL/FLUX INTERFACE PHENOMENA IN THIN SLAB CASTING

By

Joseph W. Shaver
B.S. Metallurgical and Materials Engineering
Michigan Technological University, Michigan, USA, 1993

A THESIS SUBMITTED IN PARTIAL FULFILLMENT OF THE

REQUIREMENTS FOR THE DEGREE OF MASTER OF APPLIED SCIENCE

In

The FACULTY OF GRADUATE STUDIES
Department of Metals and Materials Engineering

We Accept This Thesis as Conforming
To the Required Standard

…….

…….

…….

The UNIVERSITY OF BRITISH COLUMBIA

October 2002

ABSTRACT

Several industrial plant trials investigating meniscus behavior and defects in thin-slab casting were conducted at Nucor Steel - Indiana, USA. As some of the first experimental steps in the investigation of the Compact Strip Production (CSP) process, the trials featured mold metal level and meniscus measurements, which resulted in the emergence of a novel and inexpensive method of measuring meniscus steel velocity using nailboards. In addition, caster operating data were collected using a high frequency data acquisition system (for mold events) and the level two information system. Slab and strip samples were collected to investigate the effects of meniscus level fluctuation and fluid flow behavior upon the internal and surface quality of the steel.

Metal level and meniscus measurements were made during ordinary casting operation. Nailboards were used to make the measurements. The nailboard measurements provide a meniscus shape profiles and liquid flux layer depths. An analysis of the nailboard data has yielded information pertaining to the direction and velocity of the steel in the upper recirculation zone and at the meniscus. Through the measurement of meniscus shape and the standing wave, steel flow was determined to be influenced by casting speed, SEN (Submerged Entry Nozzle) submergence and geometry, and mold width. Knowing that present methods of measuring steel stream velocity in the continuous casting mold are costly and not ideally suited for an industrial environment, the nailboard method for measuring mold flux depths was refined. This method can measure meniscus surface velocity in a steel mill setting with reasonable accuracy and agreement with established values for flow velocity.

In conjunction with the nailboard measurements, Fast Fourier Transform (FFT) analyses were performed using caster operation data collected at a frequency of 33.33 Hz. FFT analysis shows that the metal level fluctuates with a characteristic frequency similar to predictions made by mathematical and physical models of similar casting processes. In addition, significant differences between two- and four-port SENs were also observed.

This project has led to some of the first in-plant measurements of meniscus flow velocities for the CSP continuous casting process. In addition to being a very cost-effective way of measuring meniscus shape, flux depths and velocity, the nailboard measurements can be made by operating personnel at very short intervals, thereby offering opportunities for greater process understanding and control. Being made of only plywood, steel nails, and aluminum wire, nailboards are easy to assemble and quite durable in the steel mill environment. Other findings, through FFT analyses, have helped to elucidate the behavior of flow controls, particularly SEN and stopper rod behavior, during casting and their effects upon meniscus behavior and the resulting product quality. It is believed that this research will further the understanding of and contribute to the elimination of mold flux-related defects. It is also expected that this work will lead to additional research in this relatively new area of steel continuous casting.

TABLE OF CONTENTS

LIST OF TABLES

LIST OF FIGURES

Nomenclature and List of Symbols

Vc:	Casting Speed (m/min)
W:	mold width (mm)
SEN:	Submerged Entry Nozzle
θ:	Angle of Incidence of steel on nail (radians)
R_m:	Wave run-up height (also maximum standing wave height)
H_o:	Wave height of initial flow (m)
H_o':	Unrefracted wave height (m)
k:	Ratio of wave height to the wave crest elevation above still liquid level(0.78)
γ:	Euler's Constant (0.5772)
F:	Maximum force of steel against the nail at incidence angle, θ (N)
ρ:	Density of steel (7800 kg/m^3)
D:	Diameter of steel knob on nail following mold immersion
C_m:	Inertia Coefficient (1+K)
t_s:	Sampling time (0.03 s or 33.33 Hz)
t_t:	Total time in FFT analysis (3600 s)
X_{fd}:	Peak Amplitude in the frequency domain (mm/s)
X_{td}:	Magnitude of level fluctuation in the time domain (mm)
f:	FFT-generated frequency (Hz)
t:	Empirical Period of Theoretical Maximum Frequency Wave (0.030 s)
g:	Acceleration due to gravity (9.8 m/s^2)
δ:	Fluid Flow Constant ($3\pi/8$)
ω:	Wave frequency
L:	Depth of nail immersion (0.060 m)
U:	Horizontal Velocity of Steel flowing Nail (m/s)
C:	Force Coefficient Corresponding to the Total In-line Force (=6)

ACKNOWLEDGEMENTS

I would like to extend my sincere thanks to Mary Jansepar, Gary Lockhart, Joan Kitchen, and Nancy Oikawa, whose assistance and general help have been indispensable throughout the course of this project. Without them, I would not have survived the first and last months of this endeavor.

Also, the utmost gratitude goes to my advisers, Dr. Indira Samarasekera and Dr. Brian Thomas. Their confidence in me and all of the knowledge and advice passed on will never be forgotten.

Many thanks also go to John Scheel, Steven Wigman, Daniel Larson, Mary Alwin, Dan Edelman, Clay Gross, and Sam Commella at Nucor for their unselfish cooperation during the plant trials. Special thanks go to all of the guys in production, especially Steve Stout, Montgomery Keyt, and Mickey Thompson.

Thanks also to my fellow students, especially Dr. J.K. Park, Leo Colley, Simon Jupp, Cindy Chow, and Joydeep Sengupta for their friendship, assistance and support. And special thanks also to Eric and the granite at Squamish. And finally my most heartfelt thanks to Jane.

Joseph Shaver

October 2002

CHAPTER 1: INTRODUCTION

Thin-slab casting has dramatically changed the face of the world flat-rolled steel industry. With the commercialization of SMS-Schloemann Siemag's Compact Strip Production (CSP) in 1989 at Nucor Steel - Crawfordsville, IN USA, it became possible to produce low-cost flat-rolled steel in a continuous melting/casting/rolling operation with quality acceptable to all except the most aesthetically demanding applications. The industry has seen an economic revolution as profits rose, and capital, labor, and maintenance costs have plummeted because of the continuous nature and relatively small sizes of these casting and rolling operations [1]. Thin-slab casting, and the CSP technology (which is only a segment of thin-slab technology) in particular, now accounts for a significant share of world production of flat-rolled steel products. As of late 1999, CSP steel production consisted of 29 casting machines at 19 plants worldwide with a combined per annum capacity of approximately 31 million metric tons [2].

Continuous casting has become the primary method of producing flat steel products over the past 35 years because of low cost, high yield, and high quality in comparison with ingot-cast steel. As the name implies, continuous casting allows cross sections to be cast continuously. Steel flow is regulated from ladle to mold by passing through a tundish, which provides a reservoir of steel in case of upsets in the process and also a place for non-metallic inclusion flotation to take place. Regulation of steel flow from the tundish into the mold and metal level control in the mold is accomplished by the use of stopper rods or slidegate systems used in conjunction with a refractory submerged entry nozzle (SEN). All slab casters consist of an oscillating water-cooled copper mold in which solidification begins. As the strand is extracted from the mold by drive rolls located at the machine exit, further solidification takes place in a zone of spray water cooling.

CSP casting operates along the same fundamentals as conventional thick slab casting. However, instead of producing semi-finished slabs that are often more than 250 mm thick (a feature of conventional slab casting), a CSP caster produces 50 mm thick slabs. Conventional slab casting is done at much lower speeds than thin-slab casting, about 1-2

m/min compared with 3-6 m/min for thin-slab casting. The size of the casting machine in thin-slab casting is much smaller, as the three- to fivefold reduction in slab thickness results in thin-slab casters being three

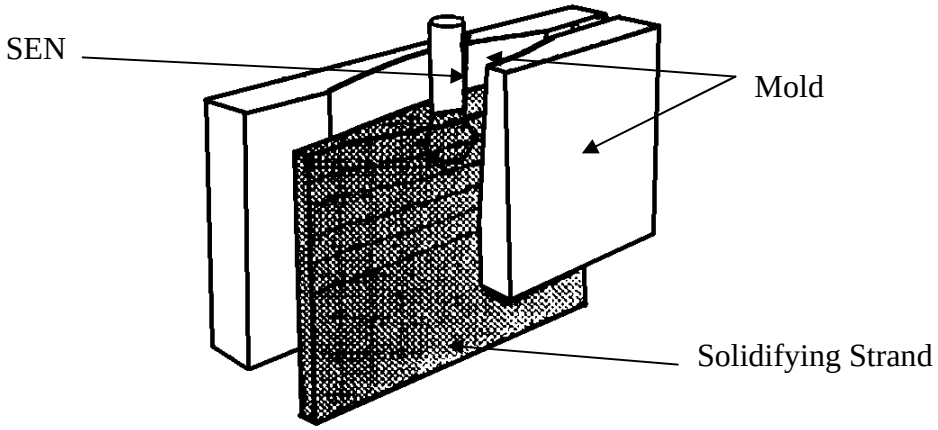

Figure 1.1: Schematic Representation of the SMS Schloemann-Siemag Mold and SEN [3].

to five times smaller than conventional casting machines. In addition to size differences, the upper portion of the CSP mold is funnel-shaped and not rectangular as in conventional slab casting and other thin-slab processes (Figure 1.1). The funnel gradually tapers down from a maximum thickness of 170 mm to 50 mm at a point 750 mm below the top. The length of the mold is 1100 mm, which is about 200 mm longer than most conventional slab casters. This additional mold length is to extract more heat and to support the thinner shell formed at high casting speeds, which are required to obtain reasonable productivity [4]. Perhaps the most important difference between conventional and thin slab casting is that conventional casting has advanced with the benefit of decades of research.

While economic factors such as reduced capital and a smaller workforce have resulted in the widespread use of the CSP casting technology, the higher casting speeds and unique mold design associated with this technology have made it apparent that there are many quality issues to be solved before the most demanding applications (e.g. exposed automotive) can be produced. Arguably, the most serious defect associated with this technology is mold flux entrapment. Mold flux entrapment is known throughout the steel

industry as a major cause of both internal and external defects in continuously cast steel. While much is known about the defect, relatively little is understood as to how flux properties and flux/steel interactions affect the formation of the defect. Most previous work on mold flux entrapment defects has been confined to conventional slab casting since thin slab casting is a relatively new technology [1,5-17].

In both conventional and thin-slab casting, the metal transfer systems are much alike and mainly differ only in scale and minor points of geometry. Figure 1.2 shows schematically the continuous casting mold, the location of the submerged entry nozzle (SEN), the solidifying shell, and the location of the mold flux regions. Curved arrows show approximately two distinct areas of molten steel flow. The upper region, known as the upper recirculation zone, is defined by the clockwise arrows and the lower region, the lower recirculation zone, is defined by the counterclockwise arrows. This kind of pattern is known as the "double roll" flow pattern. It should be noted that this is not the only type of possible flow pattern. A "single roll" flow pattern is also possible where there is only one recirculation zone. In the "double roll" pattern the upper recirculation zone interacts with the molten mold flux and, depending upon local steel flow and velocity and flux properties, the area where mold flux slivers most often form [5,6,18-19].

At the meniscus there are at least two ways to entrap flux. One is by shear across the molten steel/flux interface and the other is by level fluctuations at the meniscus. Importantly, slivers do not form exclusively from flux entrapment at the meniscus. Sometimes mold flux is carried by the flow deep into the liquid core of the solidifying strand, being trapped at depths of 1-3 meters below the meniscus [20].

Mold flux entrapment defects, or slivers, as they are commonly called in the final rolled product, originate at the meniscus in the mold. When mold powder is introduced to the surface of the steel, it melts, and three distinct regions of mold flux form over time. The uppermost region consists simply of powder flux (as received from the supplier). The middle layer is known as the sinter layer where the powder flux has begun to adhere together. These

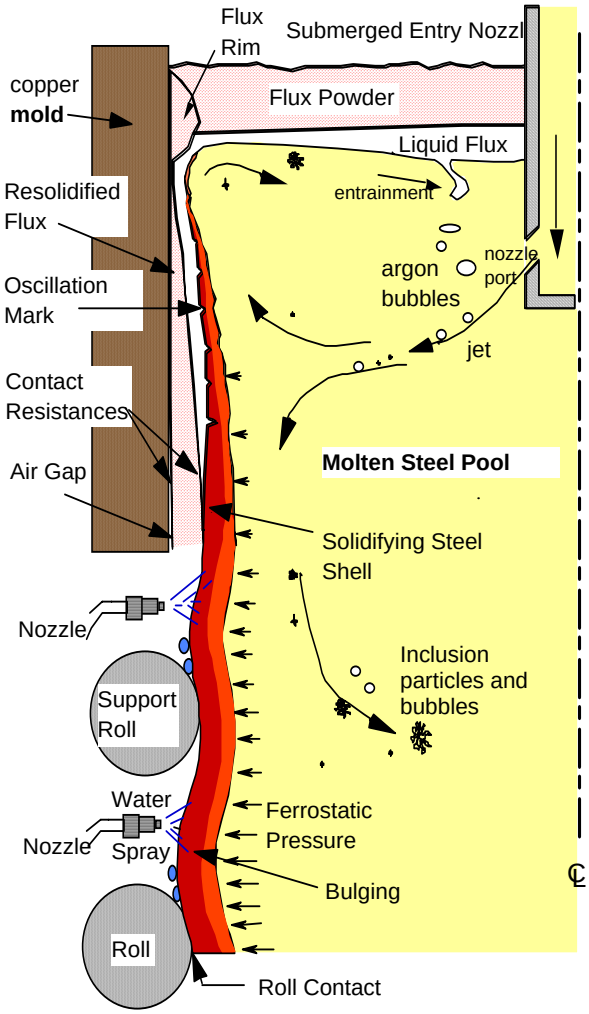

Figure 1.2: Schematic showing physical interaction of flux and steel in a continuous casting mold [19].

two layers provide thermal and chemical insulation from the atmosphere. The third and lowest region consists of a molten flux pool, which contributes to the removal of non-metallic inclusions from the steel. This molten flux also flows into the gaps between the solidifying steel shell and the mold walls, providing lubrication and allowing for slow, uniform heat transfer that is critical in the production of high quality steel [18]. However, the molten flux layer also makes mold flux entrainment possible.

The flow of steel near the meniscus can entrap flux by "dragging", or "emulsifying" droplets of molten flux into the recirculating steel stream [16]. Previous research has shown that the likelihood of slag emulsification/entrapment depends on the physical properties of

the molten flux and also on the velocity of local steel flow [9,10,12,15]. While the effects of molten slag properties are studied elsewhere, the measurement of steel velocity remains difficult. The likelihood of flux entrapment greatly increases when the flow velocity past the interface exceeds a critical value that creates shear forces necessary to draw flux into the steel. To date, most methods for obtaining steel stream velocity are costly and very sensitive to the surroundings, which makes them somewhat impracticable to measure velocity in an industrial setting [21-24].

An interesting method using nailboards (normally used for measuring mold flux depth) was thought to show some potential as a tool for indirectly measuring/calculating flow velocity in molten metals [18]. It was believed that with some novel additional measurements and application of flow phenomena, the "nailboard" technique could yield meniscus steel flow velocities that could aid in the prediction of slag emulsification. Together with high-frequency operating data, a review of literature on mold flux emulsification and defect generation, and these measurements, this work aims to allow CSP operators to measure and understand velocity and flow-related aspects of the process. Most importantly, this work was undertaken with the aim to improve the understanding of defect formation by correlating measured operating parameters with each other and with defects and process conditions.

CHAPTER 2: LITERATURE REVIEW

This chapter discusses the necessary background information critical for understanding fluid flow, refractory behavior, slag emulsification, and defect generation during the continuous slab casting of steel. The vast majority of existing literature has been based upon the operation of conventional slab casters, which operate at low casting speeds (<0.2 m/min) and aspect ratios of about ten. This information provides a solid foundation for studying thin slab casters, which operate at high speed (3-6 m/min) with aspect ratios as high as fifty.

2.1 Inclusions in Continuously Cast Steel

Inclusions in continuously cast steels are classified into two distinct groups, indigenous and exogenous. Indigenous inclusions are unavoidable byproducts of large-scale steel production and refining processes. Exogenous inclusions, on the other hand, are introduced during liquid metal handling, transit, and casting processes. This type of inclusion is often more deleterious to product quality. The best way to avoid exogenous inclusions is to prevent their creation in the first place, but unfortunately situations often are encountered where their formation is inevitable. Therefore, their removal (if possible) becomes key to achieving acceptable product quality.

The amount of indigenous inclusions is roughly indicated by tap oxygen content. More oxygen is required to produce low carbon steels than high carbon steels, as more carbon in the charge must be oxidized. In a typical basic oxygen furnace (BOF) process a tap carbon level of 0.03 wt. % corresponds to approximately 750 PPM of oxygen whereas a tap carbon level of 0.06 wt. % corresponds to approximately 450 PPM of oxygen [25]. Accordingly, more indigenous inclusions are encountered in low carbon steels. In Al-killed steel, the overwhelming majority of indigenous inclusions consist of alumina (Al_2O_3), which is created during steel deoxidation. These inclusions are ubiquitous in the steel grades being studied, but they usually do not cause serious problems if during ladle refining processes sufficient stirring time is allowed for them to float up into the slag [14].

Exogenous inclusions are often more deleterious to steel quality and are minimized by developing and following clean steel practices. This is an enormous undertaking, as every facet of steelmaking, from primary refining to continuous casting, is a potential source of exogenous inclusions. The carryover of slag from a BOF can lead to the formation of inclusions [14]. Ladle and tundish treatments, such as calcium wire or Ca-Si wire additions, can lead to the formation of calcium aluminates and silicates. Poor ladle and tundish shrouding can lead to air aspiration and reoxidation of the steel. Similarly, poor or improper use of ladle, tundish, and mold fluxes can lead to reoxidation inclusions being formed. Not only can these exogenous inclusions be entrapped but they also can cause flow disturbances in the submerged entry nozzle (SEN) and the casting mold and lead to the entrapment of slag [14,26]. It has been shown that slag entrapment is the result of emulsification due to fluid flow, and that all slags can be emulsified [15,16].

Together with efforts to prevent the formation of exogenous inclusions (e.g.. better shrouding), much has also been done to prevent the entrapment of inclusions that do form. Argon stirring has been used for the purpose of floating inclusions out of the steel and into the slag and electromagnetic braking (EMBR) is being increasingly used in the mold to modify fluid flow patterns in the casting mold with the goal of preventing inclusion entrapment and slag emulsification [14,26,27].

2.1.1 Indigenous Inclusions

As previously mentioned, indigenous inclusions are either deoxidation or reoxidation products. Deoxidation alumina forms when aluminum is added to the steel following tap. Refining practices can have a large impact upon the amount of indigenous inclusions present in the steel. Vacuum degassing is one method by which the average inclusion level can be significantly reduced due to decreased oxygen content. Argon bubbling and electromagnetic stirring (EMS) are also commonly used to transport deoxidation products to the slag so they can be removed. Argon bubbling has an advantage over EMS in that the argon bubbles contribute to the attachment, agglomeration, and flotation into the slag of the inclusions. A long period of gentle argon stirring ought to be performed in order to provide sufficient time for the inclusions to reach slag or vessel surfaces. A long period of gentle stirring is

preferable to a short period of vigorous stirring because, while the vigorous stirring yields more inclusion collisions, the resulting larger inclusions do not have sufficient time to be transported to the slag [26]. Such larger inclusions, especially those larger than 50 microns are unacceptable in exposed applications.

In addition, stirring should never be so vigorous as to form an "eye" on the slag surface as such an occurrence exposes the steel to air, which greatly increases the likelihood of the formation of reoxidation alumina [26].

In aluminum-killed steels, the second kind of indigenous inclusion is alumina formed by reoxidation. The source of aluminum in this case is the aluminum dissolved in the steel following deoxidation. These inclusions can be formed if the steel is exposed to air, whether it is due to poor ladle or tundish shrouding, extremely vigorous argon stirring, or insufficient coverage of the steel by ladle, tundish, or mold fluxes [26]. In addition to those reactions, the aluminum present in the killed steel may reduce oxides in the refractory materials or fluxes, or it may also reduce water. Lehmann et al have shown that the reactions are primarily the following [28].

$$3SiO_{2(s)} + 4Al_{(s)} \rightarrow 3Si_{(s)} + 2Al_2O_{3(s)} \quad (2.1)$$

and

$$3H_2O_{(g)} + 2Al_{(s)} \rightarrow 3H_{2(g)} + Al_2O_{3(s)} \quad (2.2)$$

Indigenous alumina inclusions, whether deoxidation or reoxidation products, can be problematic as defects in the steel and are the main reason for clogging of tundish SEN's [14,26,29]. The alumina very often adheres to the SEN refractory in large agglomerations that periodically break away to form large alumina inclusions in the cast product. Figure 2.1 shows that these inclusions can be in excess of 100 microns in size [30]. For applications such as deep drawing, where the maximum permitted inclusion size is approximately 50 microns, this type of inclusion is unacceptable [14]. Even if the agglomerations of alumina in an SEN do not break away and end up as large inclusions in the finished product, they can adversely affect the steel flow through the SEN and result in fluctuations of the metal level in the mold (Figures 2.2 and 2.3). As a clog forms and grows it creates transient flow

conditions that favor slag emulsification and slag entrapment in the mold and will be discussed later[15,16,26].

Höller has stated that alumina inclusions a few microns in size do not noticeably affect steel quality. Hence, it becomes apparent that a key approach to reducing the adverse effects of alumina must deal with the prevention of large alumina agglomerations. The two main efforts at preventing this agglomeration are the optimization of argon gas injection and

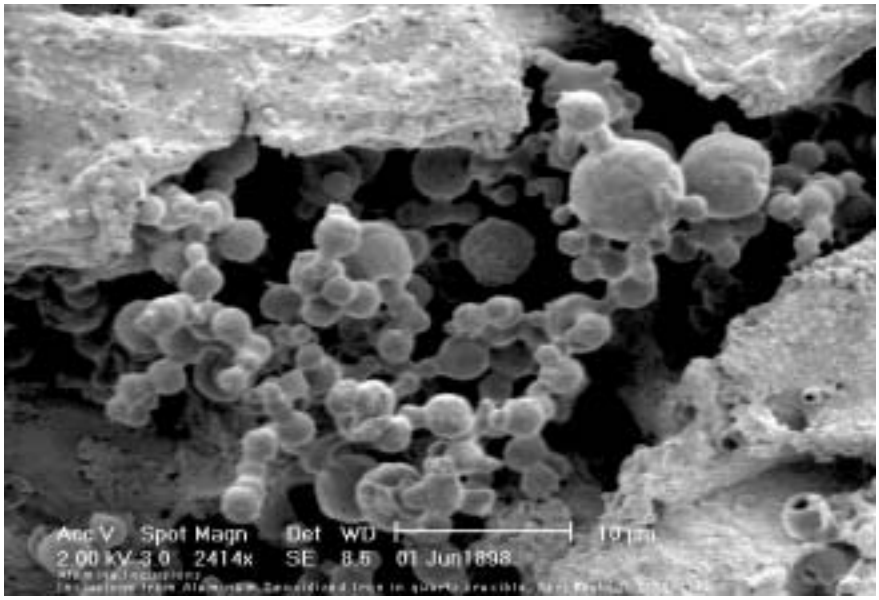

Figure 2.1 SEM Image of Reoxidation Alumina Inclusion [30].

the development of carbon-free inner bore surfaces of SEN's [29]. With respect to argon injection, Thomas and Bai cite five possible mechanisms by which it is believed argon may prevent nozzle clogging and alumina agglomeration [26]. They are as follows:

1) An argon gas film forms on the nozzle wall to prevent inclusion contact. This is likely only at high gas flow rates, which tend to cause flow disruptions in the mold.
2) Argon bubbles attach to the alumina inclusions and carry them into the slag.
3) Argon bubbling increases turbulence, which causes the delicate inclusion network to break away from the nozzle wall. However, this may be detrimental due to the increased likelihood of particle contact with the nozzle wall.

4) Argon injected into porous slits or joints in the refractory reduces air aspiration and reoxidation by instead causing argon aspiration.
5) Argon retards chemical reactions between the steel and the refractory.

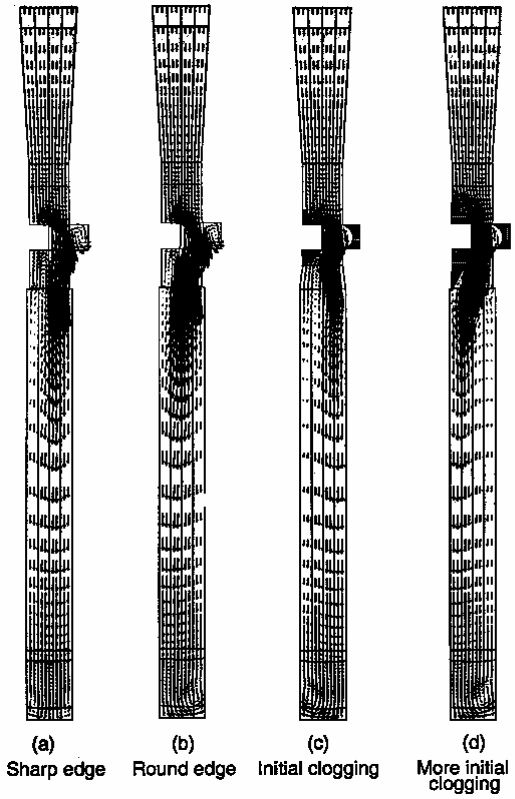

Figure 2.2. Effect of initial clogging and rounded edges on nozzle flow pattern [31].

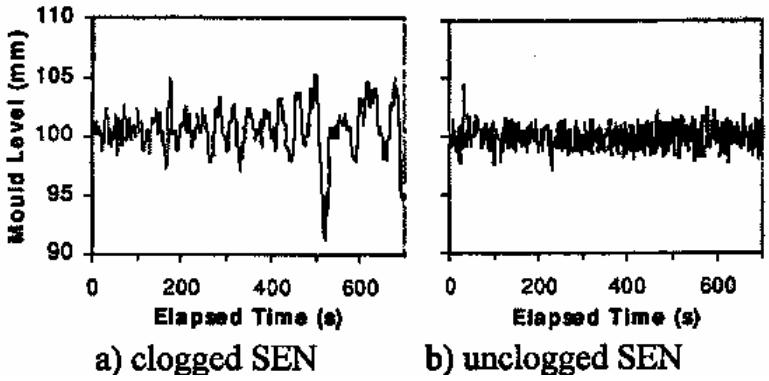

Figure 2.3. Effect of clogging upon severity of mold level fluctuations [14]

Furthermore, it is noted that argon can greatly change the steel flow patterns in the mold, often leading to transient metal level fluctuations and the formation of exogenous inclusions [26].

Modification of the inner bore surface to make the surface less wettable for alumina deposition is attractive because it may lessen mold metal level fluctuations associated with argon. Various protective coatings (including non-wettable nitride materials) for the inner bore have been tried, but their application is complicated by their peeling during preheating. These protective coatings are particularly sensitive to peeling as they tend to be very brittle and do not adhere well to the substrate refractory. In addition, the application of such coatings is very expensive. Despite these disadvantages, a promising method to combat alumina adherence is the creation of a carbon-free layer [29]. A major obstacle to the use of carbon-free layers is that carbon-free materials have rougher, more porous surfaces than the carbon-bearing refractory. Therefore, while chemically the material retards wetting by alumina, the rough nature of the surface provides sites for deposition of alumina [29].

2.1.2 Exogenous Inclusions

As indigenous inclusions can lead to the entrapment of exogenous inclusions due to fluctuations of metal level in the mold, it should also be noted that metal level fluctuations in the tundish are also a source of exogenous inclusions. Exogenous inclusions consist of mold, tundish, or ladle fluxes; products of calcium or calcium-silicon wire treatments; and products of reactions between indigenous alumina inclusions with MgO, CaO, and SiO_2, which are commonly found in refractory materials and fluxes [14,26]. For purposes of clarity and organization, exogenous inclusions will be divided into three areas: 1) inclusions formed due to emulsification and entrapment of steelmaking fluxes, 2) inclusions created during wire- or other ladle treatments, and 3) inclusions created as the result of reactions of the steel or indigenous inclusions with steelmaking refractory.

Emulsification of Slags

An important concept to understand entrapment of exogenous inclusions is the emulsification of steelmaking slags. Several researchers, most notably Cramb and Thomas,

have shown that slag emulsification occurs due to shear forces generated by the flow of liquid steel at the steel/liquid flux interface in the direction toward the SEN.

All slags can be emulsified, but the physical properties of the mold flux and the nature of the steel flow dictate the relative ease/difficulty with which a given slag may be emulsified. Slag viscosity, differential density, slag density, slag depth, and interfacial tension have been identified as the influencing physical factors upon emulsification [12,13,15,16]. Cramb has identified five processing conditions in which slag emulsification can be expected to occur [12].

1) Vessel filling (associated with high pouring energies existing in the steel and pouring through slag)
2) Vessel drainage (e.g. vortexing)
3) Excessive turbulence at the metal/slag interface because of wave motion or stream impingement
4) Gas injection rates that exceed critical values
5) Interfacial level fluctuations that exceed critical levels

In addition to this, it is known that emulsification is a common cause of inclusions that are larger than 20 microns in diameter [12,14]. Table 2.1 shows how such large inclusions can be problematic when attempting to produce sheet for high-end applications[12].

Harman and Cramb carried out a study of the effect of fluid physical properties upon emulsification using a silicon oil and water model ***not*** to model emulsification in a real casting system, but to model a mechanism of emulsification and entrapment with the goal of understanding the effects of fluid properties upon emulsification.

Table 2.1. Requirements for high purity and ultra-clean steels [12].

Product	**Purity**	**Cleanliness**	**Notes**
Automotive Sheet	C < 30 PPM N < 30 PPM	T[O] < 20 PPM d < 100μm	Ultra-deep drawing applications
Drawn and ironed cans	C < 30 PPM N < 30 PPM	T[O] < 20 PPM d < 20μm	Two-piece beverage and battery cans

Emulsification velocities and particle inclusion diameters were measured using particle image velocimetry (PIV). Measurements were taken at varying interfacial tensions and water densities. The interfacial tension of the oil/water system was measured using the DuNuoy ring method. A detailed discussion of this method is contained in the literature. First, changes in interfacial tension due to additions of a photographic chemical were measured and then the tensions were plotted versus percent of the photographic chemical. Photoflo is the trademark name of the chemical and small amounts result in a lowering of interfacial tension. This showed that the interfacial tension is very sensitive to small additions of the chemical, which contains surface-active ethyl alcohol and propylene glycol. Figure 2.4 shows clearly that the interface reaches saturation at approximately 0.5%. Interfacial tensions were then measured versus different water densities, the water density being changed by additions of potassium carbonate. As the water density approaches 1.5g/cc, the interfacial tension reduction becomes more pronounced than at lower water densities. Finally, experiments with oil viscosities of 0.5, 1, and 5 poise were performed to observe the effects of viscosity upon the entrainment velocity and initial entrained particle size [15].

The initial experiment was carried out varying only the silicon oil thickness. From this, it is apparent that emulsification velocity decreases with increasing oil thickness (Figure 2.5) and *initial* droplet diameter does not change with oil thickness (Figure 2.6). The decrease of emulsification velocity with increasing oil thickness is expected as it is easier to

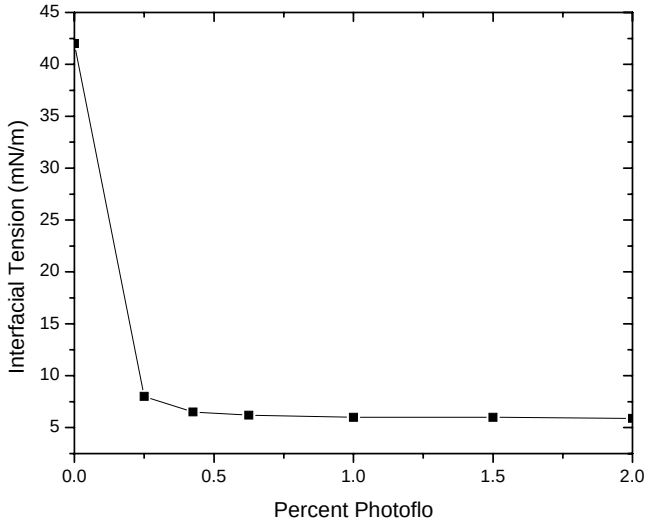

Figure 2.4. Interfacial Tension of Silicon Oil/Water as a Function of Photoflo [15].

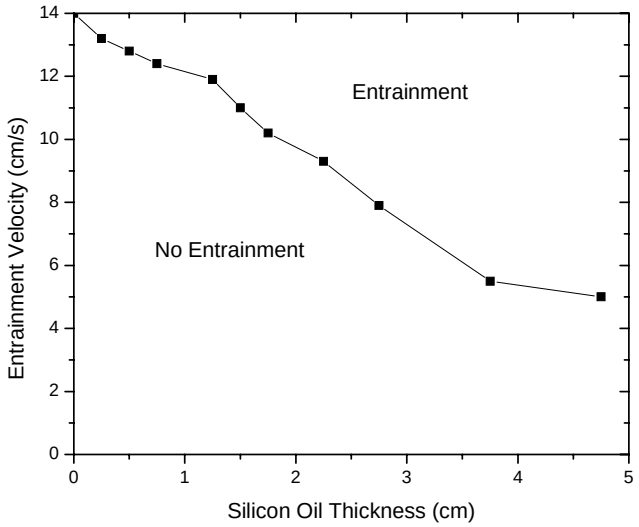

Figure 2.5. Emulsification Velocity as a function of Silicon Oil Thickness [15].

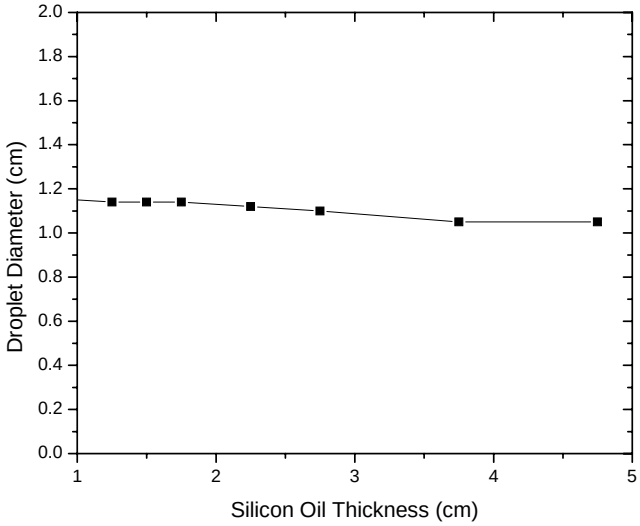

Figure 2.6. Intial Droplet Diameter as a Function of silicon oil thickness [15].

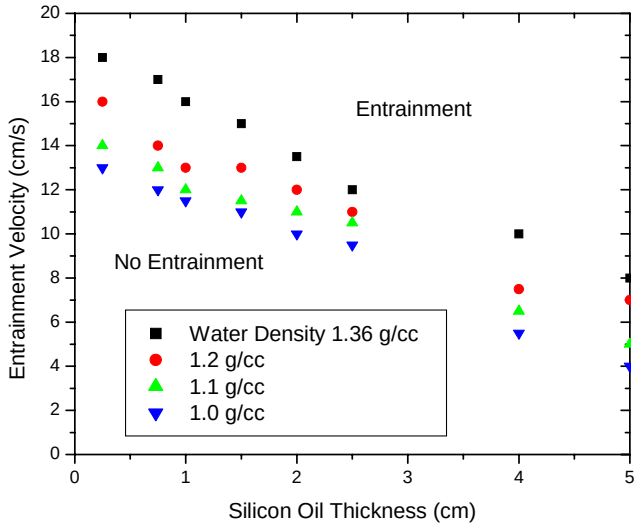

Figure 2.7. Emulsification velocity profile vs. silicon oil thickness and density [15].

entrap a particle of oil if there is more oil present. The authors do note that at an oil thickness of 4 cm the emulsification velocity levels off - this is the point where the silicon oil completely covered the surface of the water. The size of emulsified droplets was observed to decrease as the velocity exceeded the critical velocity.

The experiments carried out with varying water density, and therefore varying differential density, revealed a marked effect of density upon the emulsification velocity. As the density of water increases, the entrapment/emulsification velocity increases. This means it is more difficult to entrain/entrap particles as the differential density increases (Figure 2.7). Thus, the entrapment of slag in steel systems is expected to be much more difficult than oil-in-water models because the density of steel is about 2.5 times greater than that of slag. It was also observed that the initial entrapped particle diameter decreased with increasing differential density (Figure 2.8). The authors stress, however, that this data is confounded by a decrease in interfacial tension that accompanies the density difference increases.

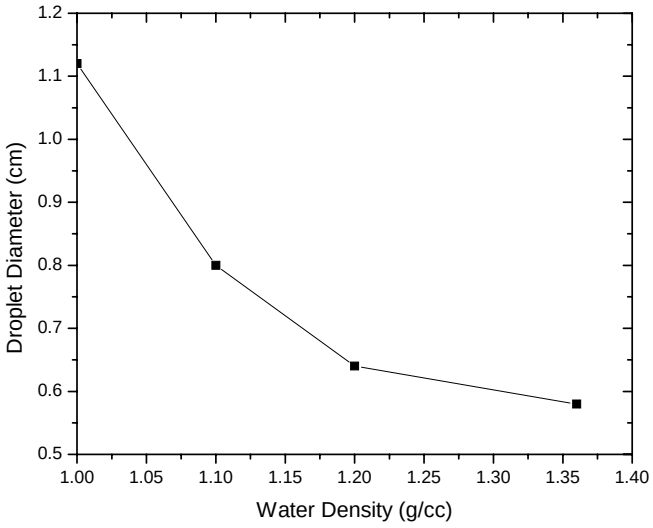

Figure 2.8. Silicon oil droplet diameter as a function of water density [15].

The third set of experiments consisted of emulsification velocity and initial particle diameter measurements versus interfacial tension. This showed very large decreases in emulsification velocity with small decreases in the interfacial tension (Figure 2.9). The experiments also showed that the initial entrapped particle size decreases with decreasing interfacial tension (Figure 2.10).

Increasing the viscosity of the slag (oil) shows an increase in the entrainment velocity and an increase of the initial particle size. Thus, it is apparent that it is more difficult to entrain droplets of larger size (Figures 2.11 and 2.12) [15].

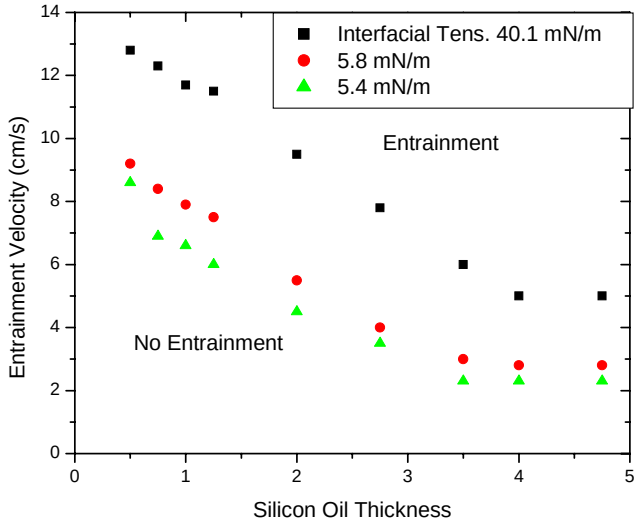

Figure 2.9. Emulsification velocity vs. interfacial tension [15].

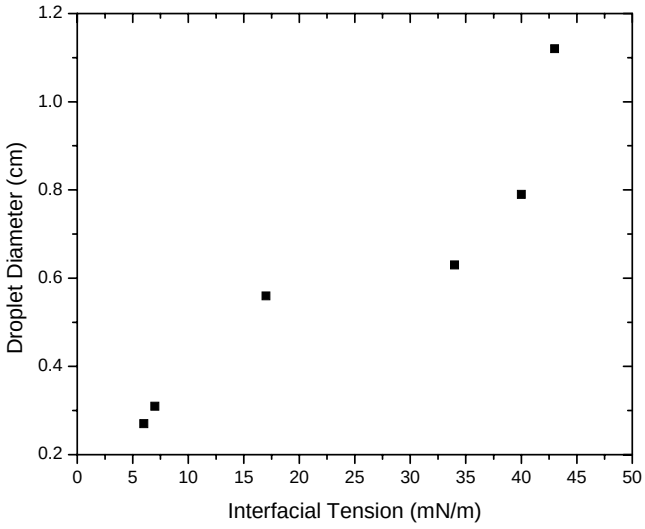

Figure 2.10. Silicon oil droplet diameter vs. interfacial tension [15].

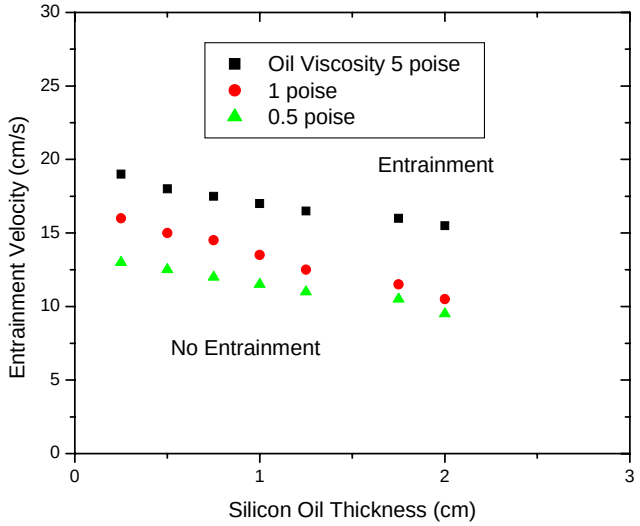

Figure 2.11. Emulsification velocity vs. silicon oil thickness and viscosity [15].

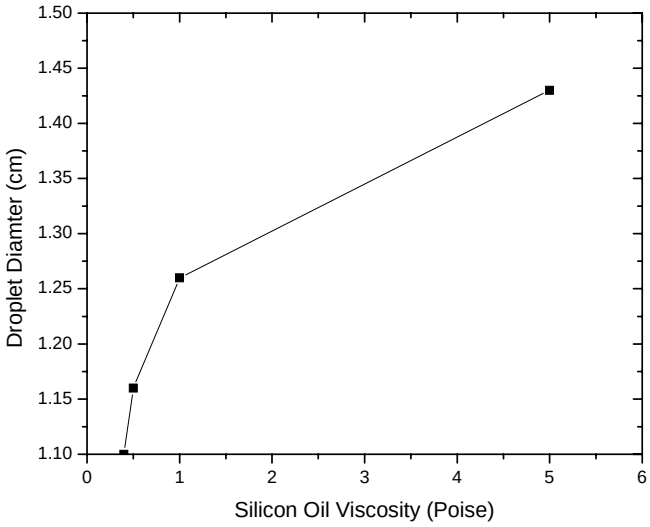

Figure 2.12. Silicon oil droplet diameter vs. viscosity [15].

As previously noted, Harman and Cramb encountered difficulties when quantifying differential density variation effects upon particle entrainment due to accompanied changes in interfacial tension. As a result of these difficulties Cramb et al endeavored to elucidate the

effect of interfacial tension upon emulsification and entrainment of particles in the molten steel/slag system. It was observed that slag is drawn out in a long tendril in the direction of the steel flow. At some significant distance from the interface, a capillary instability arises and, if the critical entrainment velocity is surpassed, droplets are emulsified and entrained continuously [14]. Building on previous research [15], oxygen and sulfur, both surfactants and known to decrease the surface tension of liquid iron with increasing concentrations, were used to analyze interfacial tension in a slag/steel system. It is evident that, at typical total oxygen and sulfur levels (25 PPM and 100 PPM, respectively) observed in low carbon aluminum-killed (LCAK) steels, the interfacial tension of liquid iron is not appreciably reduced [12,14-15].

This, however, matters little in light of the fact that interfacial energies of steel/slag systems, where slag is added to a predominantly iron alloy are 200 to 300 mN/m less than the surface energies of the corresponding iron alloy. This behavior is due to an associative interaction between the slag and metal. This resulting reduction in slag/steel interfacial tension leads to the wetting of the slag upon the steel. This behavior shows that the very presence of the slag encourages emulsification [12,14].

An excellent point brought up in this research deals with the effect of slag composition upon the slag/steel interfacial tension. Mold slags used to cast industrial LCAK steels were analyzed from two companies (1 and 2). Table 2.2 shows the compositions of four mold fluxes and slags at company No. 1. From an analysis of the interfacial tension results, it is stated that mold slag compositions with the most fluorine and Na_2O result in the lowest interfacial tensions. Similar information for company No. 2 can be found in Table 2.3. As industrial mold slags consist of more components than their parent fluxes, it becomes more difficult to analyze which components have the greatest effects upon interfacial tensions. Fortunately, it has been observed that if the total amounts of Na_2O, F, Fe_2O_3, and MnO are considered, the interfacial tension is found to be a strong function of the total content of reducible oxides in the mold flux. In addition, it was observed that those fluxes exhibiting the largest increases in alumina from the unused flux to the used slag showed an increase in surface tension. It should be noted that if ladle or tundish slag finds its way into the mold, the interfacial tension of the slag could be altered. From this information, it

appears that increases in the alumina content of fluxes, coupled with reductions in Na_2O and CaF_2, are efficient in increasing the interfacial tension in industrial mold fluxes and therefore effective at discouraging slag emulsification [12].

Table 2.2. Mold flux compositions from company 1. Compositions are in weight percent and basicity is dimensionless [12].

	Flux A	Flux B	Flux C	Flux D
CaO	**27.7**	**29**	**32**	**35.9**
SiO_2	**33.1**	**34.6**	**33**	**39.9**
F	**8.3**	**9.3**	**6.8**	**7.3**
Na_2O	**12.3**	**11.7**	**10.5**	**2.3**
MgO	**1.2**	**1.3**	**0.7**	**5.6**
C	**6.4**	**4.1**	**6.6**	**3.8**
Basicity	**0.84**	**0.84**	**0.9**	**0.97**

Table 2.3. Mold Flux and slag compositions from company 2 [12].

	Flux 1	Slag 1	Flux 2	Slag 2	Flux 3	Slag 3	Flux 4	Slag 4
CaO	**37.6**	**40.8**	**30.5**	**31.7**	**33.6**	**33.7**	**34.7**	**36.9**
SiO_2	**37.6**	**32.6**	**36.3**	**35.9**	**38.5**	**35.2**	**37.5**	**35.6**
F	**10.6**	**12.2**	**5.4**	**4.7**	**6.6**	**5.6**	**8.7**	**8.9**
Na_2O	**4.6**	**6**	**4.6**	**5.02**	**4.9**	**5.05**	**1.9**	**2.28**
MgO	**0.8**	**1.47**	**6**	**6.32**	**7.8**	**7.24**	**5.2**	**9.5**
C	**3.4**		**2.7**		**1.9**		**0.9**	
Al_2O_3	**2.7**	**7.7**	**5.2**	**10.9**	**6**	**11.2**	**6.8**	**8.9**
Fe_2O_3	**3.06**	**0.9**	**1**	**0.65**	**0.6**	**0.57**	**1.5**	**0.85**
MnO	**4.72**	**3.81**	**3.5**	**2.3**	**0.6**	**0.87**	**0.04**	**0.93**
TiO_2	**0.07**	**1.93**		**2.02**		**0.47**	**0.2**	**0.47**
Li_2O			**0.7**					
K_2O	**0.14**	**0.11**	**0.5**	**0.71**	**0.7**	**0.92**	**0.4**	**0.54**
ZrO_2		**0.73**		**0.35**		**0.48**		**0.23**
Bascicity	**1.09**		**0.84**		**0.87**		**0.93**	

2.1.3 Mold Flux and Mold Slag Properties

From the previous discussion it is quite apparent that the properties of mold fluxes and slags are very important not only for heat transfer, lubrication, and insulation, but for quality in very complex ways. Feldbauer has conveniently listed five purposes that mold fluxes serve in continuous casting molds [10].

- Provide lubrication between solidifying steel shell and the mold
- Moderate heat transfer between the shell and mold
- Prevent reoxidation
- Provide thermal insulation
- Act as reservoir for the absorption of inclusions, liquid and solid, from the molten steel

Also listed are seven problems caused by inappropriate mold flux application. Three of the these are applicable for this project.

- Sub-surface cleanliness problems in the cast product
- Slag patches on the surface of continuously cast sections
- Chemical interaction between the liquid steel and the liquid flux pool [10].

This list of flux functions and potential problems illustrates, along with the emulsification discussion, that mold flux and mold slag design must be performed very meticulously to produce fluxes that facilitate the production of clean steel. Of particular interest in the work of Feldbauer is the claim that interfacial tension increases with increasing amounts of CaF_2 and Na_2O [10]. This contradicts the results of Cramb, et al, which claim the opposite behavior [12]. One possible reason for this is that Feldbauer measured interfacial tensions with slags containing between 30 and 60% CaF_2 and Na_2O while Cramb dealt with slags containing less than 20% of those compounds. With the exception of fluorospar and soda, Feldbauer recommends that a flux have a high viscosity, high interfacial tension, and small amounts of reducible oxides (most notably FeO and MnO) to avoid slag emulsification. It is noted that such fluxes may lead to a greater likelihood of sticking in the mold and therefore, to costly breakouts. Therefore, the utmost care must be taken by the flux manufacturer to balance the properties of the flux to be both somewhat resistant to emulsification while fulfilling all of its necessary functions [10]. Figure 2.13 shows how a typical sliver may appear.

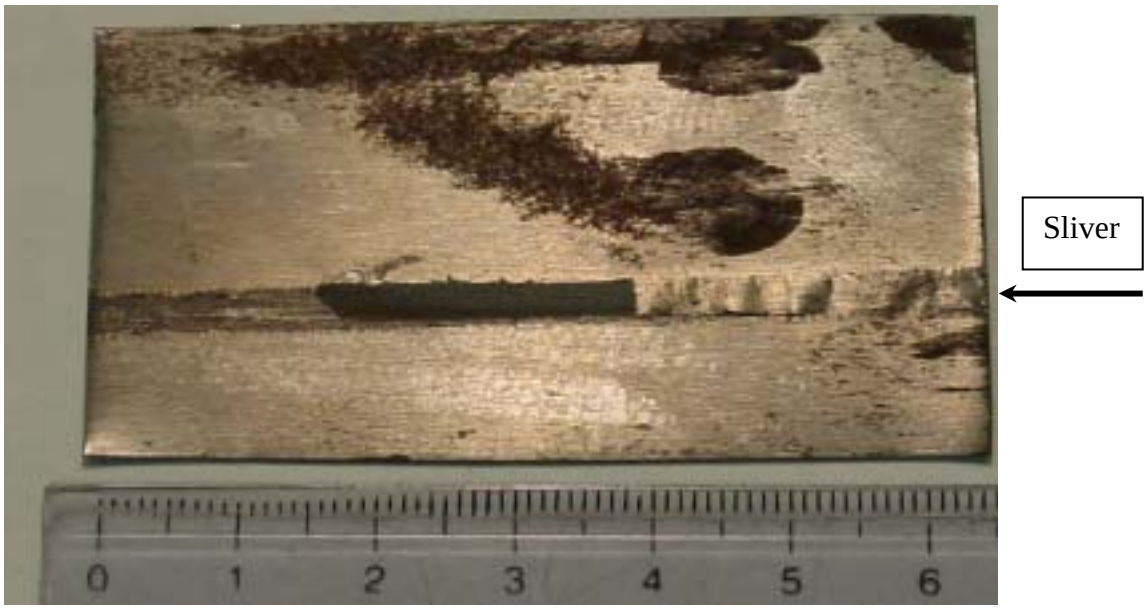

Figure 2.13. Typical mold flux sliver.

A different mechanism, referred to as slag adhesion by Bommaraju, et al, can also result in sliver defects [11]. This adhesion can be related to meniscus hook formation. The meniscus can frequently freeze because of local undercooling of the steel due to high heat transfer in the meniscus region. This condition is naturally exacerbated at low superheats. It is postulated that if the molten mold flux adheres to the solidified meniscus, it can be trapped at the base of the oscillation mark. A sliver then becomes visible after subsequent hot and cold rolling. Figure 2.14 illustrates a possible mechanism for the creation of a sliver in this manner. To combat this flux adhesion, it has been discovered that decreased amounts of soda lead to less flux adhesion to the solidified meniscus. In a trial with fluxes with no Na_2O present, preliminary results report a decrease in the number of observed mold flux sliver defects while no significant changes were observed in either attainable cast speed or heat transfer. Unfortunately, the system used to rate the sliver quantity and severity appears quite subjective and does little to prove the effectiveness of the trial mold fluxes [11].

2.1.4 Effects of Fluid Flow and Flow Transients upon Exogenous Inclusion Formation in the Mold

Fluid flow and transient flow phenomena, with no surprise, play an important role in the creation of exogenous inclusions. In particular, these phenomena play an integral role in the

emulsification of slags. Again, for purposes of scope and relevance, only the flow behavior of the casting mold will be discussed. While flow behavior is different near the slag/steel interfaces in ladles and tundishes, the concepts of the relationship between fluid flow and inclusion formation are the same. Huang and Thomas have shown, through 3-D 2-phase modeling, that biased flow (one port of SEN with more flow than the other) gives rise to vortices in the lower recirculation zone of the strand. Figure 2.15 shows that a stream of higher flow (right side) entrains more liquid than the stream on the other side of the mold. The stronger stream increases the size of the recirculation zone because the momentum entrainment by the stream is proportional to the square of stream velocity. This leads to a strong downward flow in the strand, resulting in deep penetration of inclusions and bubbles, which will predominate on the right side of the strand [32].

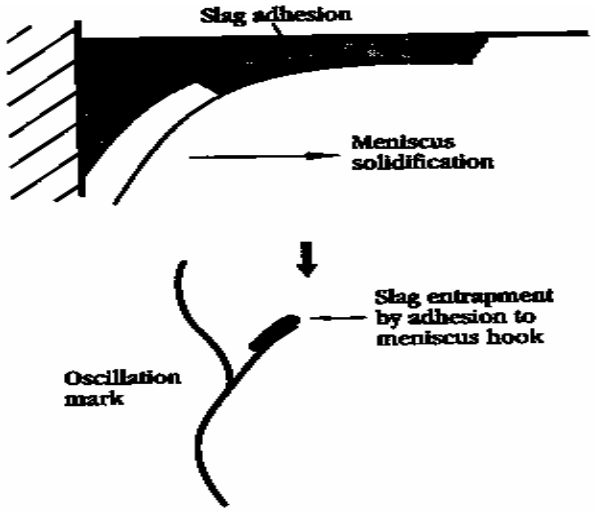

Figure 2.14. Schematic of meniscus hook formation and slag adhesion to the oscillation mark base [11].

Both Huang and Thomas [30] and Honeyands and Herbertson [6] have shown that SEN submergence depth has a marked effect upon surface turbulence in slab and thin slab molds. In Figure 2.18 it can be seen that level fluctuations decrease by almost 50% with an increase in SEN submergence depth from 100mm to 180mm [32]. With such an increase in submergence depth, the flow streams are located significantly lower in the mold. Submergence and casting speed have also been shown to have a strong effect upon the period of metal level oscillation in the mold (Figure 2.17). This kind of behavior may help in

describing the periodic nature of mold flux related defects as it is widely believed that transient events such as these lead to the entrapment of mold slag [6].

With the knowledge of how exogenous inclusions may be entrapped in the continuous casting mold, a significant challenge is encountered when trying to use these concepts to evaluate steel quality. Milone, et al have used the thermal analysis of the meniscus region to evaluate the occurrence of inclusions in continuously cast slabs. Through Fourier analysis of mold metal level data, a striking pattern was observed with respect to SEN clogging. Figure 2.4 shows a low frequency oscillation of metal level between 0.01 and 0.03Hz in the Fourier power density spectrum. Also seen is the progressive increase in metal level fluctuations due to decreasing flow rates and the subsequent metal level response [31]. Such behavior can lead to vortexing with a likelihood of slag entrapment [32]. The Fourier power analysis, used in this manner, can indicate when alumina agglomerations break away from the clog and enter the steel. It is also noted that sudden speed changes and slidegate/stopper rod changes exacerbate the problem. Used correctly, this method is useful for linking defect formation with events in the mold [31].

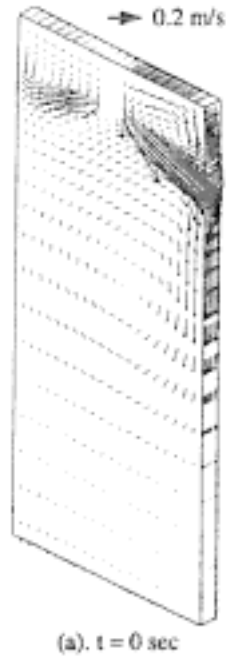

Figure 2.15. Predicted flow velocities in simulation involving biased flow [32].

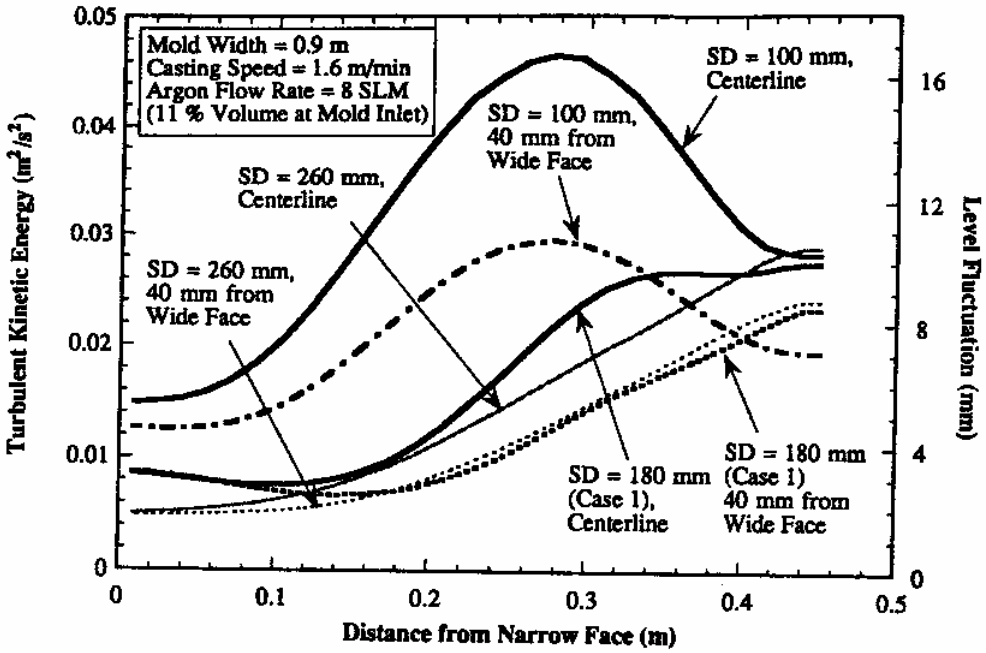

Figure 2.16. Effect of submergence depth on predicted turbulent kinetic energy and correlated surface level fluctuations [32].

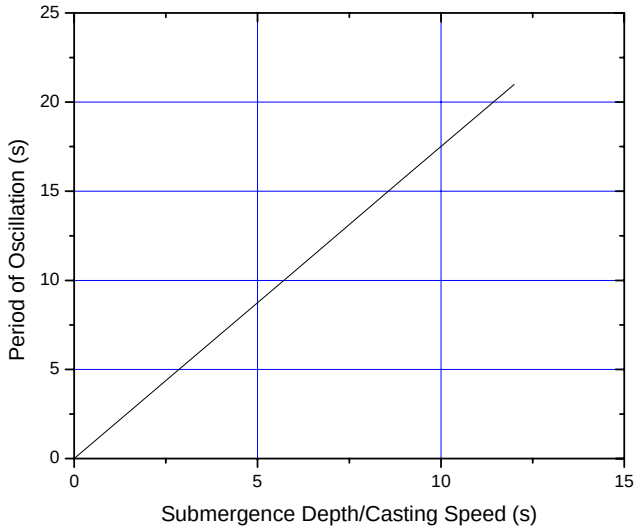

Figure 2.17. Period of oscillation vs. Average Residence Time in Upper Recirculating Region [Adapted from Reference 6, Figure 4].

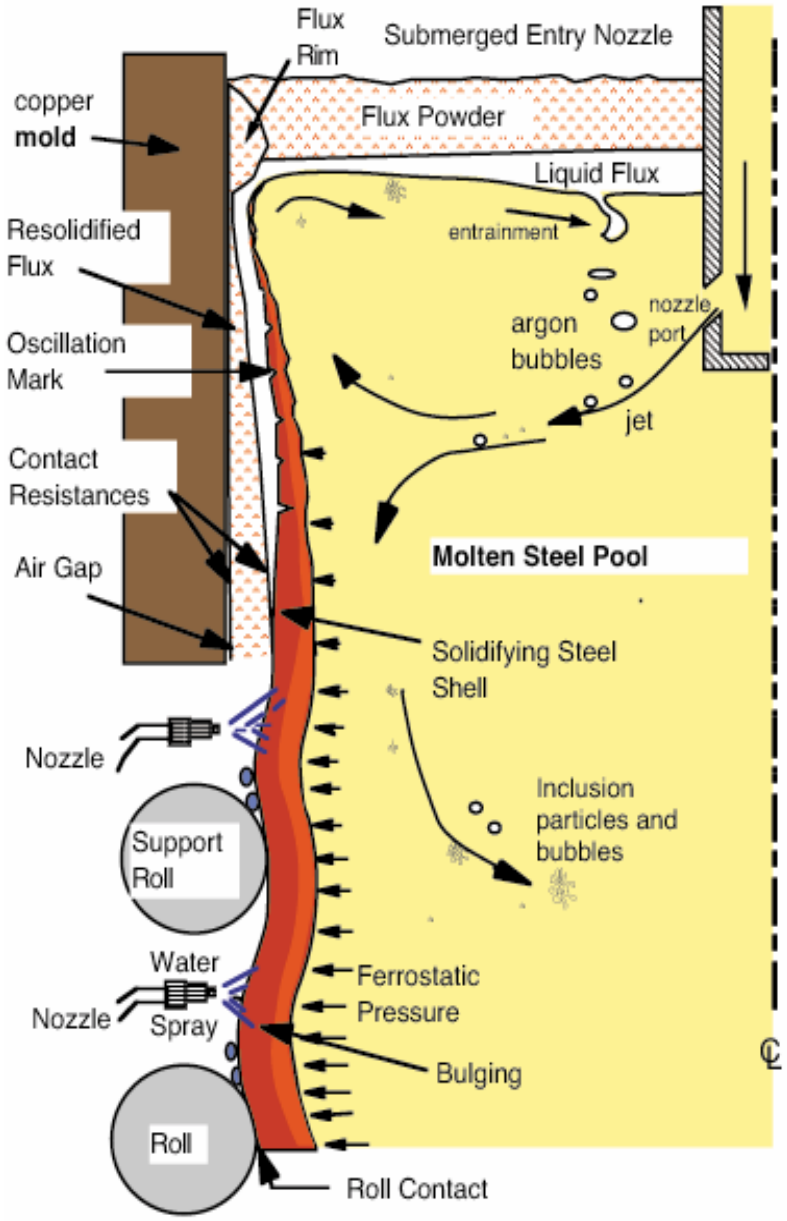

Figure 2.18. Schematic showing physical interaction of flux and steel in casting mold [19].

McDavid and Thomas have modeled the flow and thermal behavior of the top surfaces of both the liquid flux pool and steel in a slab mold. It has been found that the shear forces generated by the steel flow near the steel/slag interface create a large recirculation zone in the liquid flux pool. This zone's depth increases with increasing casting speed,

increasing mold flux conductivity, and decreasing mold flux viscosity. Figure 2.18 shows a schematic of the physical interaction of flux and steel in a generic continuous slab casting mold. The purpose of the modeling was to quantify the phenomena of powder melting and liquid flux behavior in an operating caster. It is interesting to note that the flux domain based on thick-slab measurements in the research is similar in shape to one found in the present work, taking into account the shape of a standing wave (Figure 2.19) [18].

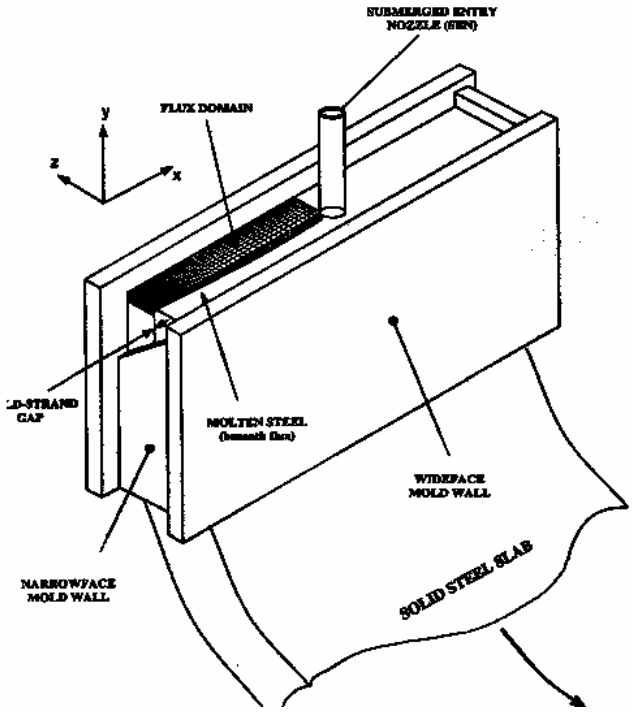

Figure 2.19. Schematic of CC slab mold showing flux simulation domain [18].

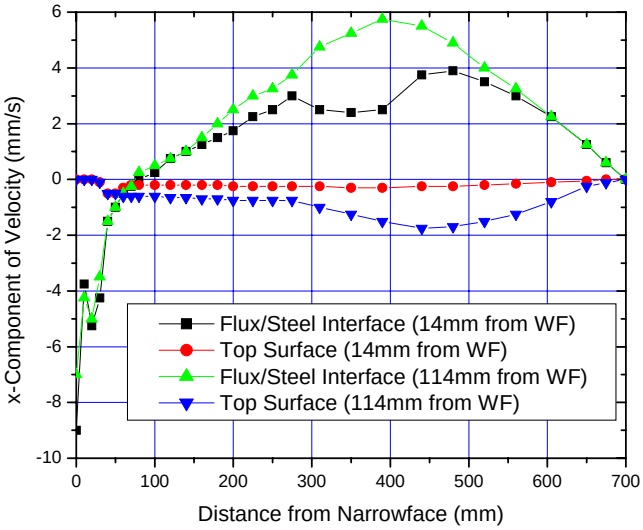

Figure 2.20. Top surface and flux/steel interface velocity distribution as a function of distance from the narrow face [18].

The velocity differences across the width of the mold seen in Figure 2.20 are present due to the formation of the recirculation zone. The velocity decreases in each area with the maximum velocity observed at the steel/flux interface and the minimum at the top surface. This behavior, together with the formation of a separation point where shear forces reach a maximum (shear is zero at the narrow faces and SEN), results in a wide distribution of liquid flux layer depths in the mold (Figure 2.21) [18]. Such differences in flux layer thickness are known to affect the ability of a slag to be emulsified (Harman and Cramb [15]). Temperature distributions across the liquid flux layer were also calculated. Temperatures range from about 325°C near the narrow faces to about 800°C near the SEN. These temperatures indicate that the temperature gradients through the flux layer near the narrow faces are much greater than near the SEN [18]. Such variation in temperature will undoubtedly lead to wide viscosity variations within the liquid flux, thereby making some areas of the liquid flux pool more susceptible to emulsification [15,18]. Validation of the model comprised the measurement of the depths, positions, and flow direction in the mold using nailboards. The nailboard consists of steel nails coupled with aluminum wires, which melt at different distances and temperatures, thereby identifying the steel/flux and flux/powder interfaces,

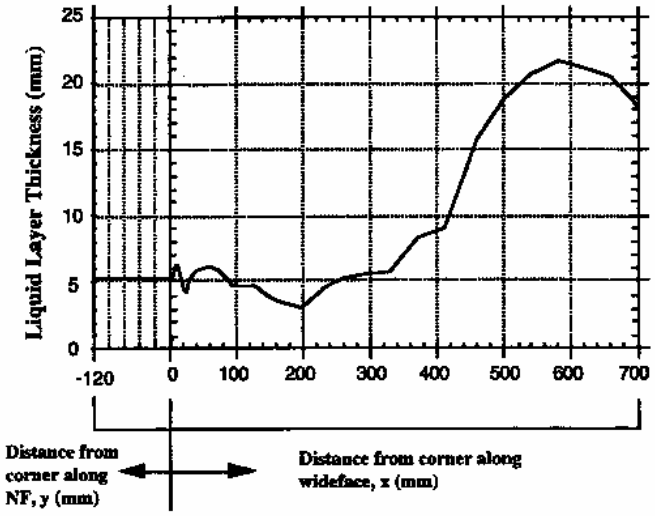

Figure 2.21. Liquid layer thickness around mold perimeter (standard condition) [18].

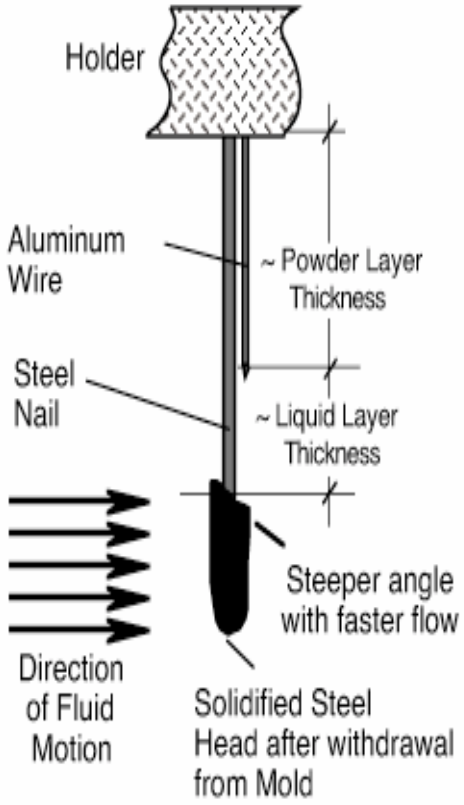

Figure 2.22. Close-up of cross section through a nailboard [19].

Figure 2.22 presents a schematic of a nailboard used for determining the locations of the interfaces.

One way to modify flow conditions in the casting mold is the use of electromagnetic braking (EMBR). EMBR works by applying a static magnetic field perpendicular to the casting direction across the mold. As liquid steel moves through the mold the flow, through a static magnetic field, induces electric currents, which generate forces opposite to the flow direction. These forces have a braking effect upon the steel. In plant trials, use of the EMBR has shown significant reduction in steel flow velocity below the meniscus (Figure 2.23). The method for obtaining the flow velocity in Figure 2.23 consisted of a cylindrical refractory body immersed in the steel, but the method is not discussed as it is proprietary [27]. In addition, use of the EMBR has shown reductions in metal level fluctuations (Figure 2.24) and reductions in standing wave height (Figure 2.25). Such accomplishments are promising in that smaller shear forces are generated due to decreased flow velocities and a more uniform liquid flux pool is maintained due to the smaller standing wave and smaller deviations of the metal level. These three things all make it more difficult for mold slag emulsification to occur and may result in fewer slab defects. One item is troubling, however. The literature shows that with the EMBR on, there is little circulation near the narrow face (Figure 2.26). A concern is that the meniscus may freeze in this area, leading to hangers and possible breakouts [25].

2.1.5 Tundish Fluid Flow and Effects upon Inclusions

Fluid flow in the tundish also has a tremendous effect upon steel cleanliness. Tundishes exist for several reasons. They provide a buffer between the ladle and mold which allows ladle changes to be made with minimal effect upon cast speed. Tundishes also serve to assist in clean steel production due the fact that many inclusions generated during steel refining are able to float out into the slag while in the tundish. In addition, the tundish acts as a mixer of sorts, resulting in consistent temperatures and steel composition. While this mixer effect is beneficial while casting only one grade of steel, it can increase the amount of mixed steel when making grade changes [33]. It is desirable to minimize grade intermix to avoid downgrading of material and, to do this, the level in the tundish must be taken to a low level. Such level fluctuations expose the tundish to air, thereby increasing the amount of oxygen

entrained, and they also provide good opportunities for slag to be entrained into the steel [14,33].

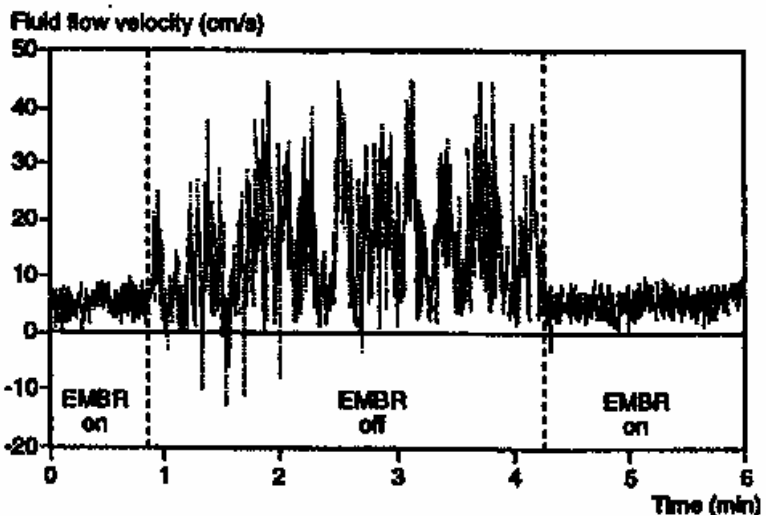

Figure 2.23. Reduction in steel velocity and turbulence below meniscus with EMBR [27].

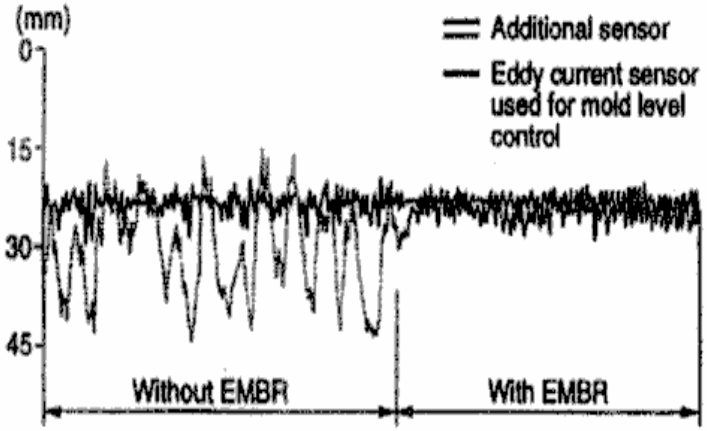

Figure 2.24. Mold level variations in middle and narrow side of mold with EMBR [27].

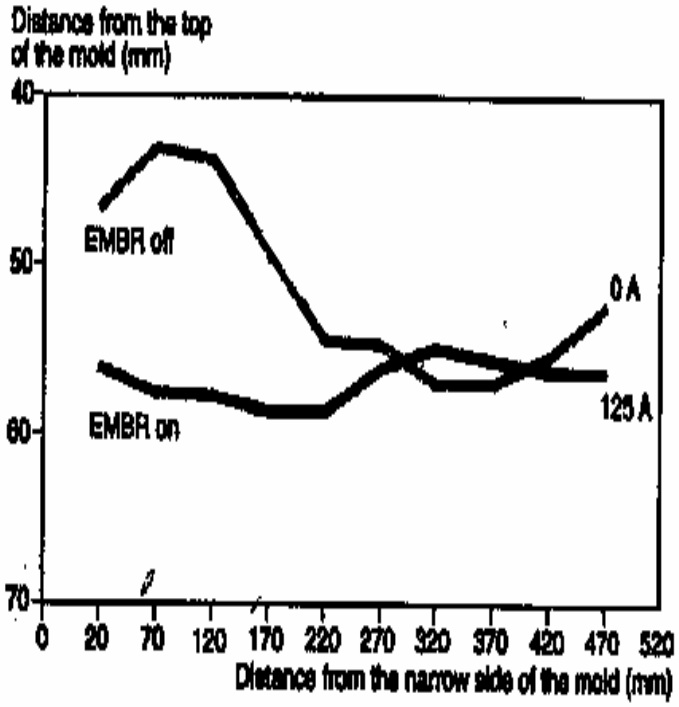

Figure 2.25. Reduction in standing wave near narrow side of a thin slab mold with EMBR [27].

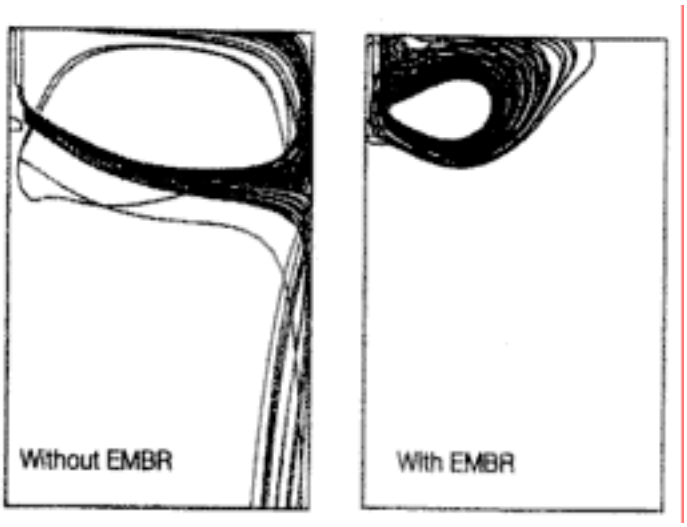

Figure 2.26. Simulation showing movement of non- metallic inclusions (200μ) toward the meniscus [27].

Four sources of exogenous inclusions in the tundish include: [14].

- Open Pouring
- Steel pouring at low tundish levels
- Operation of the tundish with a slag covering over the turbulent region around the ladle shroud
- Pouring using a ladle shroud that is not submerged (pouring through slag)

Open pouring results in a large amount of oxygen and alumina being introduced into the tundish. Steel pouring at low tundish levels can be thought of much the same way as decreased SEN submergence in a mold. Slag emulsification is more likely to occur when the submergence is decreased [6,13,32]. Operation of the tundish with turbulence near the ladle shroud will lead to emulsification of the slag in much the same way as pouring at low levels. Pouring through slag, on the other hand, causes slag to be entrained immediately. Only a very large tundish, which is very well designed with respect to flow modifying devices, will assist in floating the entrained slag. Pouring through slag is arguably the worst occurrence in casting with respect to inclusion formation [14,33].

Tundish size plays a significant role in the incidence of inclusions in steel. The larger a tundish is, more time is available for inclusion flotation. A compromise must be made in designing a tundish - the tundish should be large enough so as to provide sufficient time for inclusion flotation, but it must not be so large that cost and yield concerns become prohibitive [33].

Tundish flow modifying devices, commonly referred to as "furniture", are key in the design of a tundish. Short-circuiting of flow directly from the ladle shroud to the SEN is to be avoided, as inclusions do not have time to float into the slag. Figure 2.27c shows an example of short circuit flow in a tundish. It is desirable to maximize the time an inclusion spends in the tundish and to ensure it passes near the slag covering from time to time so that inclusions have short distances to travel to reach the slag (Figure 2.27a,b). It is in this manner that a tundish becomes an effective tool in the manufacture of clean steel [14,33].

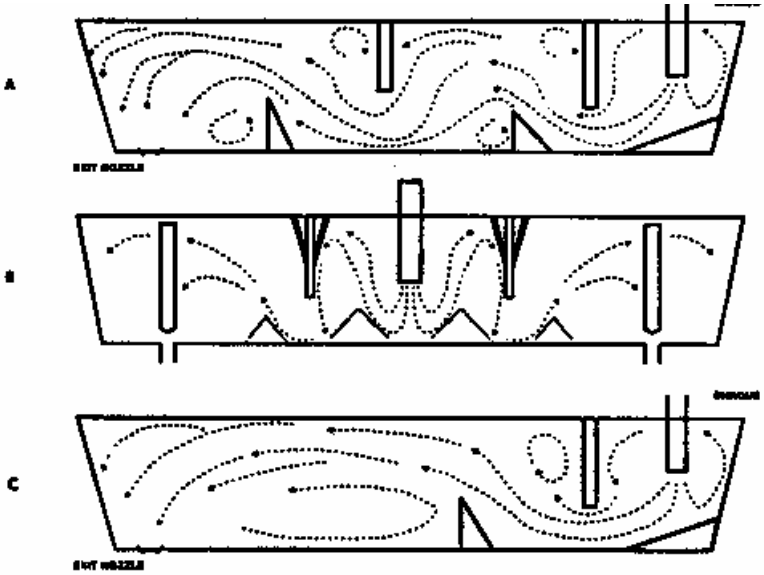

Figure 2.27. Schematic of tundish designs [33].

2.1.6 Inclusions Formed During Ladle Treatment and Reactions with Fluxes and Refractory

Exogenous inclusions that form during ladle treatment are mostly the products of reactions between calcium and indigenous alumina inclusions. Calcium aluminates comprise the majority of these inclusions, although calcium sulfides are also commonly formed (depending upon sulfur level at time of Ca treatment). Calcium treatment is carried out for two reasons: 1) calcium will react with alumina to form liquid calcium aluminates, which can be floated into the slag and 2) to modify the shape of manganese sulfide inclusions in the rolled product for formability purposes.

At steelmaking temperatures, there are two species of calcium aluminate that exist in the liquid state. $3CaO\text{-}Al_2O_3$ has a melting point of 1535°C and a density of 3.04 g/cc. $12CaO\text{-}7Al_2O_3$ melts at 1455°C and has a density of 2.83 g/cc. The $C_{12}A_7$ inclusion exists at about 50-53% Al_2O_3 in the binary system with calcia (Figure 2.28). These less dense $C_{12}A_7$ is reported in sizes of 10-15 microns when the aluminum content of the steel is greater than 0.020 wt.%. These inclusions are generally considered more desirable than alumina inclusions, as the liquid aluminates will not clog the SEN if they are not floated into the ladle or tundish slag and thereby removed from the steel. This is a great development, provided these liquid inclusions do not react further with refractory or fluxes to form solid inclusions

that stick to stopper rod and SEN refractory, resulting in clogging. In addition, great care must be taken to ensure that sulfur levels are low (<0.008 wt.%) so that calcium sulfides will not form. Calcium sulfide is solid at steelmaking temperatures and is notorious for causing SEN clogging [34].

Calcium aluminates are also believed to form during reactions with ladle, tundish, and mold slags, especially those with high CaO contents. Carryover slag from the ladle to tundish provides oxygen for the reoxidation of aluminum present in the steel. It is a calcium aluminate inclusion with traces of magnesium that is widely thought to result in cracking. This inclusion may be the result of carryover slag, buildups on the ladle walls, or poor tundish practice (poor level control, excessive slag, and open pouring). Magnesium is picked up either by ladle slag or by reaction of alumina with tundish refractory, leading to alumina-silicate slags with varying amounts of Mg and Ca (depending on slag carryover and refractory composition) [33,34]. Tundish coverings high in silica (e.g. rice hulls) exacerbate this problem as the rice hulls are fluxed by the slag, leading to an acid slag [33].

Mold powders and slags may react with the steel or existing inclusions to generate deleterious inclusions that are unacceptable in cast steel. McPherson and McIntosh have found that black spot defects found on exposed automotive sheet consisted of a calcium aluminate with 70% alumina and 30% CaO along with small amounts of manganese, silicon, and sodium [13]. From the analysis, it is evident that mold flux was the source of the defects. Through water modeling, it was evident that the mold slag was being entrained by the steel streams exiting the SEN. It was decided to increase the SEN submergence depth in an attempt to reduce the frequency of the defect. Following this change, calcium aluminate incidence on the strip surface dropped dramatically. It was also discovered that the practice of raising the tundish (and SEN) at the end of cast caused the defect to appear. The practice was discontinued and the defects disappeared [13]. Submerged entry nozzles also contribute to the formation of exogenous inclusions. Oxidation, physical erosion, and reactions with pre-existing inclusions all play a role in the wear of SEN's, and thereby the entrapment of inclusions in the steel. Excessive oxidation can be encountered if air is aspirated. In addition to alumina clogging due to air aspiration, the carbon present in the alumina-graphite refractory (most common material for SEN) will react with oxygen, resulting in degradation and disintegration of the refractory [29]. The most damaging effects upon SEN refractory

and the subsequent generation of inclusions are due to the action of mold fluxes and slags upon the refractory material. Some of the CaO present in the flux reacts with the alumina present in the refractory, leading to the formation of calcium aluminates which are washed away by the steel flow. High fluorine contents, in the form of CaF_2, exacerbate the problem because, as the fluorine is emitted as a gas or reacts with silicon, more calcium becomes available to attack the refractory. The addition of boron nitride to the refractory (to increase wear resistance) resulted in the formation of low- melting B_2O_3-Al_2O_3 compounds that are carried away with the flowing steel even faster than calcium aluminate [29].

A common slag band material used in SEN applications is MgO-stabilized zirconia. The zirconia is able to withstand slag attack better than alumina graphite. The MgO in the slag band reacts with silicon in the mold slag to form magnesium silicate, which then settles at the ZrO_2 grain boundaries. As the MgO is consumed, the zirconia becomes destabilized and a martensitic phase transformation occurs. A volume expansion accompanies this transformation. During this change from a cubic to a monoclinic crystal structure, microcracks form. The microcracks expose more material to slag attack and erosion of the slag band continues. Inclusions containing zirconia are then released into the mold and some of these, in turn, become entrapped in the solidifying steel [35].

Of particular interest with respect to this project is the effect of boron on the SEN and the quality of the steel. In the area of thin slab casting, boron is being increasingly used to aid with the uniformity of physical properties of cold-rolled LCAK steels. Many mini-mills produce steel with nitrogen levels of 95-110 PPM (compared with about 50 PPM in BOF operations) [25,36]. Added to such steel, boron reacts with nitrogen to form boron nitride. Boron nitride acts in much the same way as aluminum nitride, pinning grain boundaries. This grain boundary pinning leads to a more uniform grain size across the width of a cold-rolled strip as opposed to typical low carbon steel. A common problem with low carbon strip was that physical properties (Rockwell hardness, in particular) were inconsistent across the width of the strip. These inconsistencies are believed to have led to such processing problems as edge wave on the coils. The addition of boron, and the subsequent formation of boron nitride, caused this problem to go away. At the same time, however, mold powder related defects rose dramatically. These defects appeared as elongated dark areas on the strip surface where the steel appeared to blister or delaminate completely from the strip. Analysis

has shown these defects to contain calcium, silicon, magnesium, aluminum, and sodium [36]. The appearance of the defects and the analysis results are corroborated by similar results in numerous other sources, particularly Cramb [14]; and McPherson and McIntosh [13].

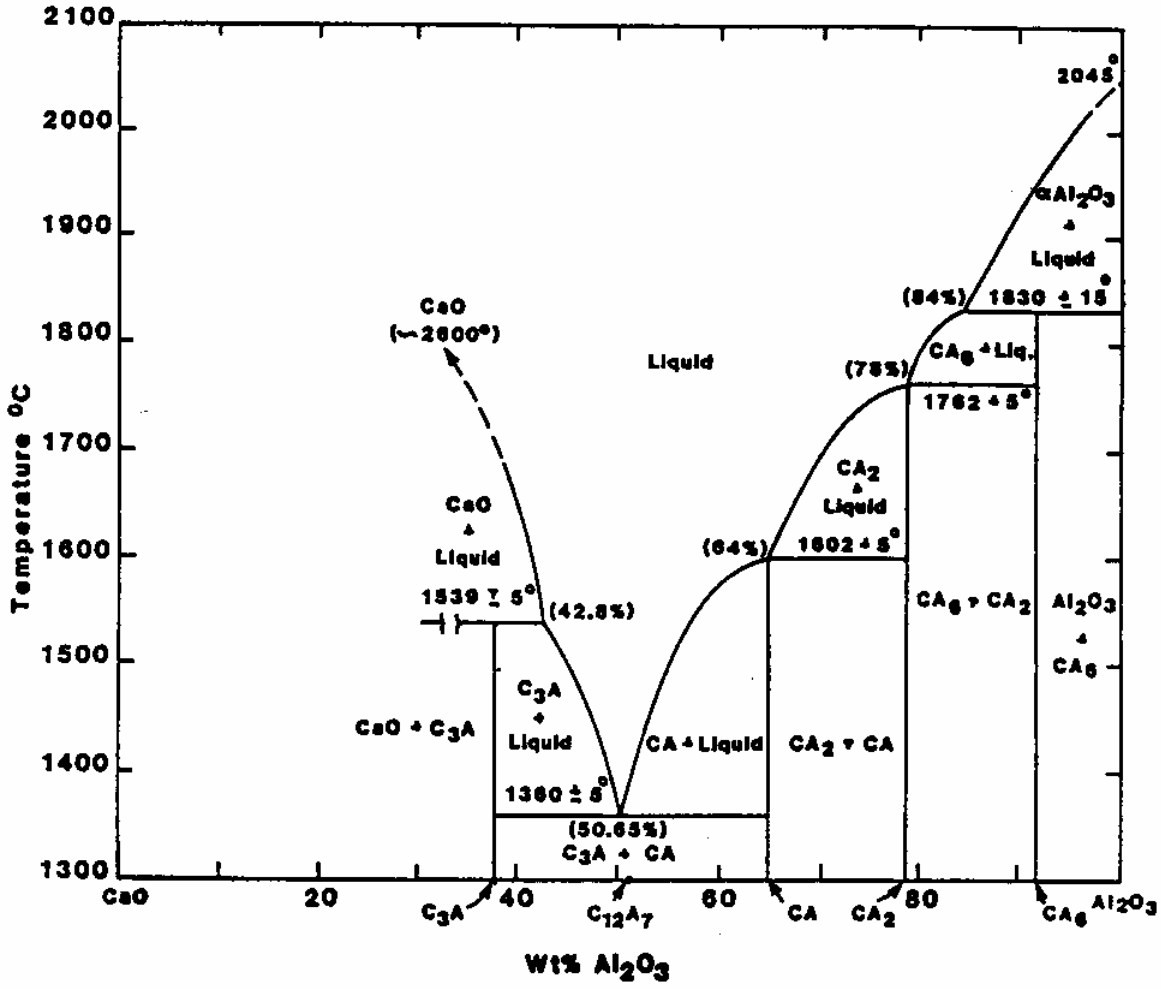

Figure 2.28. Binary phase diagram of CaO-Al_2O_3

Other observations made with respect to boron-bearing grades were that SEN life was about half that observed with typical low carbon steels and that boron addition was about 75-80% efficient. Moreover, in this plant, a ladle shrouding system that incorporates no argon injection, obsolescent bayonet-type shrouds, and a simple lever-type shroud manipulator was in place. Such a shrouding system is very susceptible to air aspiration. It is well documented that poor ladle shrouding is a prime source for picking up oxygen in the tundish

[10,14,26,33]. Taking this into account, it is thought very likely that unreacted boron in the steel reacts with oxygen in the tundish to form boron oxide. As a casting sequence progresses, B_2O_3 continually reacts with the alumina-graphite refractory of the SEN, resulting in fairly rapid erosion of the refractory due to the formation of low melting B_2O_3-Al_2O_3 compounds [29]. These compounds may lead to slivers and appear similar to mold flux defects. A typical SEN used in thin slab casting is bifurcated with a flow-controlling device positioned at the interior bottom of the nozzle. This device acts to direct the steel flow into the ports smoothly. It is postulated that as this flow-controlling device is eroded, a biased fluid flow pattern arises. This process is believed to lead to inclusion formation in the steel and preliminary in-plant observations support this as increased mold turbulence in the form of flux "rolling" was seen later in casting sequences (after approximately 5 hours).

2.2 Metal Level and Meniscus Behavior in the Thin Slab Casting Mold

Metal level and meniscus control in the casting mold is a critical aspect of steel continuous casting. It is at the meniscus that many inclusions/defects are drawn into the steel. Extensive research has been conducted regarding meniscus behavior and it has been shown that insufficient and/or erratic control of the metal level in the mold can lead to poor meniscus behavior and defect formation. This research has been driven by the move towards technologies that incorporate high-speed casting (especially thin slab casting) and makes the understanding and control of metal level and meniscus behavior critical [7-9,17-18,31,37-43].

Most of the research consists of analysis of fluid flow effects upon metal level. This has been done mainly through mathematical and physical modeling. As casting speeds have increased from 1.5-2 m/min on conventional slab casters to 5-6 m/min with the CSP technology, it is evident that steel flow in the CSP mold is much faster and more turbulent than in conventional slab casting. This is because there is a similar amount of steel flowing through a much smaller mold in approximately the same amount of time [1-2,5-6,27,39,42,49-50].

Two other effects upon mold metal level are bulging and SEN clogging. While well known to cause metal level fluctuations, they are still encountered frequently. Clogging is the more serious of the two and has been discussed previously. Bulging, however, is not

always very serious if the amount of bulging between containment rolls is small and the grade being cast is not susceptible to core cracking [4,43]. Bulging can be identified easily. The requisite information for diagnosing and eliminating bulging consists of casting speed, containment roll diameter and pitch, and metal level data acquired at a sufficient frequency - usually 5 Hz or higher [43]. It should be noted that the effects of bulging on metal level fluctuations is not well understood and is the subject of continuing study.

Inclusions formed in the tundish can have a large effect upon SEN clogging. In studying clog material, Byrne, Cramb, and Fenicle [14] have found a complex oxide surrounding a core deoxidation/reoxidation product. The complex oxide was discovered to contain all the components of mold powder and the deoxidation/reoxidation core was found to be either alumina or magnesium aluminate. Upon further analysis, it became evident that upon cooling, the complex oxide formed large calcium silicate crystals in a matrix of mold flux. This observation indicates that the clog was liquid at steelmaking temperatures.

These results suggest a different mechanism for SEN clogging. It is thought that when a mold flux reacts with SEN refractory, it coats the SEN with a thin film on both the interior and exterior surfaces that are immersed in the steel [14]. Following the film formation, deoxidation and reoxidation products present in the steel attach to the film and begin to dissolve in the slag film. It is in this manner that the slag layer increases in thickness. This coating then acts like glue and will enhance the adhesion of the clog to the shroud. Even clean steels with little alumina are susceptible to this type of clog, as any alumina present will adhere to the clog. If the steel contains a lot of alumina, an alumina-type clog will then form. Liquid calcium aluminates, unlike alumina, cause the clog material to become less viscous, resulting in wash-throughs and increased SEN erosion (e.g. with Ca-Si treated steels). This type of clog will periodically break away during turbulent flow events in the mold and lead to inclusions in the cast product [14].

2.2.1 Steel Stream Velocity Measurements in the Meniscus Region

One of the most intriguing, yet difficult, tasks in the research of steel continuous casting is the measurement of velocity in the mold. Steel stream velocity has been measured in conventional slab casting molds using several different techniques. Argyropoulos has classified seven such techniques according to their advantages and disadvantages. With the

exception of the sphere-melting technique, the methods commonly used for measuring fluid flow velocity in a cavity are unsuitable and somewhat impractical for used in the harsh steel mill environment [22]. Another method exists for measuring velocity through the detection of Karman vortices, which are generated by fluid flow past a submerged refractory cylinder. While this method is quite accurate for measuring velocity, it cannot be continuously used for mold monitoring because of the sensitivity of the requisite apparatus to heat and dirt [21-24].

The sphere-melting, Karman vortex, and MFC (from AMEPA) sensor methods have produced results that agree very well with the stream velocities predicted by many mathematical simulations and physical models [17-24,32,38-39,42,48-51]. Despite these promising results, none of the methods has been used extensively for the measurement of steel flow velocity in the meniscus region on any casters under normal operating conditions and hence, there is little real data in existence for flow velocity of continuous casting molds. Considering only the CSP technology, there is currently no existing real data, only data generated by mathematical and water models [42].

A different method for measuring velocity is the nailboard. The nailboard operates upon the same concept of the flux depth measurement; a series of steel nails are driven through a board marginally smaller than the mold thickness and an aluminum wire is set parallel to each nail. Upon submergence (about 10 seconds) in the mold, the nails and Al wires melt to distinguish the meniscus line and the thickness of the liquid flux layer. Also available is the depth of the powder/sinter flux layers. McDavid and Thomas have also used nailboards to show the direction of flow in the mold since a knob of steel is left on the end of each nail. The highest point of each knob shows from which direction flow predominated. It has also been hypothesized that this method could also be used for measuring velocity in the mold, but this has not yet been attempted [18].

CHAPTER 3: SCOPE AND OBJECTIVES

It is apparent from the preceding chapter that most of the scarce literature on CSP casting consists mostly of mathematical and physical modeling results. Constructing numerical models is very challenging with such a mold [40]. In addition, there has been little validation of models with in-plant experiments. Most experimental results are from conventional casting operations. When the CSP technology was commercialized in 1989, it was envisioned as a low capital venture aimed at making inroads into the bottom end of steel markets. This was quickly realized and increasingly there has been demand for higher quality steel to be produced by the CSP technology. Researchers have attempted to apply results from conventional casting to CSP casting with some success, but there have been more failures than successes in this respect. The funnel-shaped mold is too different from conventional molds to be compared on an equal basis and the high casting speeds and fluid flow rates introduce challenges never before encountered in slab casting. These factors, as well as the demand put forth by customers (mainly in the automotive market) have induced steel companies that use CSP technology to begin extensive research into the improvement of surface quality. The financial success of this technology, based on low production costs and resultant favorable profit margins (even with lower selling prices than conventionally cast steel), has contributed significantly to this development. To achieve the quality level necessary for exposed automotive applications, extensive research into this technology is required so it can be developed to the fullest extent possible. To be useful, this research must begin on a basic level, much as research on conventional casting did over thirty years ago [1-4].

To date, there have been three plant trials conducted at Nucor Steel in Crawfordsville, Indiana USA. The current project is just the first step in understanding this emerging casting technology. The scope is somewhat broad, but necessary as there is no existing body of work of this type that has been performed on CSP technology. Performing such in-plant experiments on a relatively little-known technology is difficult as obstacles often arise and must then be overcome - the learning curve regarding CSP casting is yet steep.

This project was initiated to provide a solid base of knowledge and real casting data that will be relevant in subsequent studies of fluid flow behavior and defect generation in CSP continuously cast sheet steels. The objectives of the project were:

1a) To evaluate available literature to establish the current level of knowledge with respect to flow behavior and related defects during CSP casting.
1b) To investigate flow phenomena in the CSP mold.
1c) To measure simultaneously many different plant data.
2) To perform plant trials on an operating CSP caster (Nucor Crawfordsville) aiming to evaluate the nailboard method as an inexpensive and physically robust tool for measuring and elucidating meniscus behavior, primarily in the determination of flux depths, flow direction, and flow velocity.
3) To investigate a possible relationship between meniscus velocity results and surface defect generation.
4) To compare the meniscus velocity calculations of this project to those generated by mathematical and physical models. This will determine to what extent the results of this project are compatible/relevant to previous understanding.
5) To develop correlations between the nailboard/meniscus data and high-frequency casting data.
6) To use all the methods employed in the project to evaluate meniscus flow differences between casting with two-port and four-port submerged entry nozzles.

As one of the first phases in CSP research, it is believed that this project will encourage further research into the fluid flow, mold flux, and refractory behavior in this new and rapidly growing sector of the steel casting industry.

CHAPTER 4: EXPERIMENTAL PROCEDURE - INDUSTRIAL TRIALS

As part of this project studying the mold flux entrapment during the CSP thin-slab casting, three extended plant trials were conducted at Nucor Steel - Crawfordsville, IN USA. The trials took place in June 2000, February 2001, and June 2001. As the project unfolded and new information acquired, measurement techniques and emphasis changed accordingly. This chapter will summarize the casting conditions and measurements made in this work.

4.1 Casting Machine and Operating Practices

The Nucor-Crawfordsville CSP caster produces slabs that are 50 mm thick and 985-1460 mm wide for various hot-rolled and cold-rolled sheet applications. The plant has two casters of one strand apiece. The trials were all conducted on Caster #2 on 125-ton heats cast at speeds between 3.3 and 5.5 m/min.. This caster consists of an 1100 mm-long CSP mold with a funnel width of 985 mm and a funnel depth of 165 mm at the top of the mold. The funnel gradually flattens out, with the mold becoming parallel 850 mm from the top of the mold. Tundish capacity is 20 tons and flow from tundish to mold is controlled via a stopper rod and SEN system. The stopper rod controls flow by seating into the head of the SEN, which cannot be exchanged during casting. The specifications of the casting machine are presented in Table 4.1.

4.1.1 Trial Casting Parameters

Experimental parameters varied during the trials include steel composition, casting speed, mold width, and metal level setpoint and nozzle design. Experiments were conducted during casting to simultaneously measure processed metal level signal, stopper rod position, pinch roll speed, pinch roll current, and the raw output from the radioactive source /receiver used for metal level control. Ranges of each measured variable are given in Table 4.2 to elucidate their effects upon fluid flow in the mold and the resulting quality of finished product. In addition, other nailboard measurements, slag samples, steel samples analyzed for defects after subsequent processing stages were collected. Operating details pertaining to the four experimental parameters are presented in Table 4.3. The compositions for all of the heats involved are listed in Table 4.4.

Table 4.1: CSP Caster Specifications at Nucor-Crawfordsville

Machine Type	SMS
Number of Strands	1
Slab dimensions	50 mm thick x 985-1460 mm wide
Mold Details	
Type	Funnel
Material	Cu-Ag
Width / Taper Adjustment	Variable (4 RAM Drives)
Mold Length	1100 mm
Wall Thickness	25 mm
Metal Level Control	Cobalt-60 Berthold Source
Metal Level (from top of mold)	40-189 mm
Casting Speed	3.3-5.5 m/min
Tundish Flow Control	Stopper Rod/SEN
Tundish Level Control	Load Cells
Reoxidation Protection	Refractory Shrouding/Fluxes
Oscillation	Electromechanical
Stroke	6 mm
Oscillation Frequency	66 cycles/meter of cast length
Mold Lubrication **Consumption** **Powder Type**	Mold Powder 0.5 kg/ton cast FMP LMP-3s

Table 4.2: Experimental Casting Parameters

Operating Variable	**Experimental Operating Range**
Aluminum Content	.020 to 0.060 wt % Al
Boron Content	0 to 0.0087 wt % B
Casting Speed	3.55 to 5.21 m/min
Metal Level Setpoint	50 mm to 90 mm from top of mold

4.2 Data Acquisition

For all 27 heats of this study, the casting speed, actual metal level, metal level setpoint, stopper rod position, pinch roll speed, pinch roll current, and raw signal data from the radioactive source were collected with a Process Data Acquisition (PDA) analyzer connected directly to the mold and process PLCs (process logic controllers) and processed with a

Table 4.3: List of Plant Trial Heats and Operating Parameters. Heat flux values are mold totals.

Heat Number (Case #)	Carbon Content (%)	Boron Content (%)	Casting Speed (m/min)	SEN Depth (mm)	Heat Flux (MW/m^2)	Comments
114376 (1)	0.032	0.0071	4.57	n/a	7.68	PDA off
114377(1)	0.033	0.0071	n/a	n/a	7.48	PDA off
114378(1)	0.038	0.0068	n/a	n/a	7.64	PDA off
114379(1)	0.028	0.0070	5.08	272.5	7.56	
114380(1)	0.030	0.0081	5.08	285	7.57	
114381(1)	0.031	0.0087	4.69	297	7.62	
114382(1)	0.035	0.0086	3.81	283.7	7.23	
114405(2)	0.046	0.0003	4.45	278.9	8.40	
114406(2)	0.048	0.0003	4.45	n/a	7.57	
211246(2)	0.050	0.0002	4.47	263.6	7.56	
211247(2)	0.045	0.0002	4.19	276.3	7.36	
211248(2)	0.054	0.0002	3.84	289.6	7.17	
211249(2)	0.054	0.0002	4.39	293.6	7.53	
211408(3)	0.029	0.0062	4.69	n/a	n/a	PDA down
211409(3)	0.036	0.0042	4.69	n/a	n/a	PDA down
117004(4)	0.055	0.0002	5.08	278.4	7.76	
117005(4)	0.062	0.0002	4.06	290.6	7.45	
117006(4)	0.059	0.0002	4.45	n/a	8.81	
117021(4)	0.036	0.0002	4.57	292.1	6.76	
117022(4)	0.038	0.0002	4.57	295.4	7.88	
117023(4)	0.033	0.0002	4.57	282.9	7.85	
117024(4)	0.033	0.0002	4.57	270.6	8.01	
117025(4)	0.036	0.0002	4.57	262.9	7.52	
117026(4)	0.034	0.0002	4.57	275.2	7.52	
213760(4)	0.057	0.0001	5.13	267.2	7.61	
213763(4)	0.055	0.0002	5.08	282.7	7.53	
213782(4)	0.045	0.0002	4.06	280.9	6.78	
213783(4)	0.043	0.0002	4.57	n/a	8.39	
213784(4)	0.055	0.0002	4.57	n/a	8.20	

Table 4.4: Chemical Compositions of Heats Studied in the Project.

Heat	Grade	C	Mn	P	S	Si	Cu	Ni	Cr	Mo	Sn	Al	V	Nb	Pb	Ti	Ca	B	Zn	N	Sb	Co	Mg
114376	**B1**	0.032	0.25	0.009	0.007	0.017	0.09	0.05	0.05	0.014	0.007	0.042	0	0	0	0.003	0.0006	0.0071	0.011	0.0095	0.0023	0.004	0
114377	**B1**	0.033	0.23	0.01	0.004	0.024	0.08	0.05	0.06	0.016	0.01	0.044	0	0	0	0.002	0.0005	0.0071	0.009	0.0102	0.0025	0.005	0
114378	**B1**	0.038	0.24	0.011	0.003	0.021	0.08	0.05	0.06	0.015	0.008	0.044	0	0	0	0.002	0.0009	0.0068	0.007	0.0100	0.0022	0.004	0
114379	**B1**	0.028	0.24	0.008	0.003	0.023	0.08	0.05	0.05	0.016	0.007	0.048	0	0	0	0.002	0.0008	0.007	0.010	0.0103	0.0023	0.004	0
114380	**B1**	0.03	0.23	0.009	0.002	0.024	0.08	0.04	0.04	0.015	0.007	0.046	0	0	0	0.003	0.0006	0.0081	0.001	0.0097	0.0022	0.004	0
114381	**B1**	0.031	0.24	0.009	0.005	0.022	0.08	0.05	0.04	0.014	0.008	0.048	0	0	0	0.002	0.0006	0.0087	0.009	0.0095	0.0021	0.004	0
114382	**B1**	0.035	0.24	0.008	0.004	0.023	0.08	0.05	0.04	0.014	0.007	0.044	0	0	0	0.002	0.0007	0.0086	0.007	0.0103	0.0019	0.004	0
211246	**A3**	0.05	0.37	0.009	0.005	0.021	0.05	0.03	0.04	0.011	0.003	0.049	0	0	0	0.002	0.0007	0.0002	0.007	0.0095	0	0.005	0
211247	**A3**	0.045	0.36	0.01	0.009	0.024	0.05	0.03	0.06	0.011	0.004	0.044	0	0	0	0.002	0.0008	0.0002	0.004	0.0093	0.0001	0.004	0
211248	**A2**	0.054	0.37	0.01	0.005	0.027	0.05	0.03	0.06	0.013	0.005	0.042	0	0	0	0.002	0.0008	0.0002	0.005	0.0093	0	0.004	0
211249	**A2**	0.054	0.36	0.012	0.007	0.023	0.07	0.03	0.06	0.018	0.007	0.047	0	0	0	0.002	0.0008	0.0002	0.005	0.0100	0	0.004	0
213760	**W3**	0.057	0.64	0.006	0.011	0.013	0.05	0.04	0.08	0.017	0.005	0.022	0.048	0.002	0.001	0.001	0.0012	0.0001	0	0.0139	0.0001	0.005	0.0001
117004	**W3**	0.055	0.61	0.005	0.002	0.016	0.04	0.02	0.04	0.011	0.002	0.026	0.046	0.002	0.001	0.001	0.0008	0.0002	0	0.0139	0.0014	0.003	0.0002
117005	**W3**	0.062	0.6	0.006	0.008	0.012	0.06	0.02	0.04	0.01	0.004	0.025	0.046	0.002	0.001	0.001	0.0009	0.0002	0	0.0132	0.0014	0.003	0.0001
117006	**W3**	0.059	0.64	0.007	0.004	0.017	0.04	0.03	0.04	0.012	0.002	0.021	0.048	0.003	0.002	0.002	0.0008	0.0002	0	0.0134	0.0014	0.007	0.0002
213763	**W3**	0.055	0.62	0.012	0.004	0.028	0.04	0.02	0.05	0.007	0.009	0.035	0.052	0.002	0.001	0.002	0.0012	0.0002	0	0.0148	0	0.003	0.0001
117021	**T1**	0.036	0.23	0.004	0.008	0.03	0.09	0.03	0.04	0.013	0.006	0.044	0.001	0.001	0.001	0.024	0.0007	0.0002	0.011	0.0095	0.002	0.001	0.0001
117022	**T1**	0.038	0.24	0.004	0.003	0.025	0.07	0.03	0.03	0.012	0.006	0.048	0.001	0.001	0.001	0.022	0.0005	0.0002	0.012	0.0082	0.0017	0.003	0.0001
117023	**T1**	0.033	0.21	0.004	0.005	0.022	0.08	0.05	0.03	0.014	0.006	0.048	0.001	0.001	0.001	0.021	0.0004	0.0002	0.013	0.0092	0.0017	0.004	0.0001
117024	**T1**	0.033	0.23	0.004	0.006	0.023	0.09	0.04	0.04	0.014	0.008	0.047	0.001	0.001	0.001	0.02	0.0005	0.0002	0.014	0.0091	0.0016	0.004	0.0001
117025	**T1**	0.036	0.23	0.004	0.005	0.022	0.09	0.05	0.04	0.014	0.006	0.047	0.001	0.001	0.001	0.021	0.0005	0.0002	0.013	0.0096	0.0014	0.004	0.0001
117026	**T1**	0.034	0.23	0.004	0.004	0.024	0.08	0.04	0.03	0.013	0.006	0.049	0.001	0.001	0.001	0.022	0.0006	0.0002	0.014	0.009	0.0014	0.003	0.0001
213782	**T7**	0.045	0.84	0.007	0.004	0.029	0.05	0.02	0.03	0.012	0.005	0.033	0.004	0	0.001	0.096	0.0006	0.0002	0	0.0112	0.0001	0.004	0.0002
213783	**T7**	0.043	0.85	0.008	0.008	0.026	0.06	0.03	0.03	0.012	0.012	0.029	0.005	0	0.001	0.093	0.0004	0.0002	0	0.0104	0	0.004	0.0002
213784	**P1**	0.055	0.34	0.018	0.003	0.028	0.06	0.03	0.03	0.011	0.012	0.047	0.001	0.001	0.001	0.002	0.0007	0.0002	0.008	0.0085	0	0.003	0.0001

Table 4.5: Level Two Parameters

Parameter
Time
Casting Speed
Mold Width
Tundish Temperature (Superheat)
Mold Water Inlet Temperature (all faces)
Mold Water Outlet Temperature (all faces)
Copper Mold Plate Thickness
Slab Tracking
Stopper Rod Position
Metal Level
Metal Level Setpoint
Oscillation Frequency
Mold Narrow Face Taper

Windows NT workstation. The data sampling frequency was 33.33 Hz (30-millisecond period). The raw data from the source were converted from a 4-20 mA range into a distance below the top of the mold using linear interpolation, 4 mA at a metal level 189 mm from the top of the mold and 20 mA a metal level 40 mm from the top of the mold.

In addition to the PDA data, "level two" data were also collected every 0.94 meters of cast length. Table 4.5 presents the data collected via the level two system. This information includes time of production, casting speed, mold width, tundish temperature (superheat), mold water inlet temperature, mold water exit temperature, mold thickness, cast length (for slab tracking), stopper rod position, metal level, metal level setpoint, oscillator frequency, and narrow face taper. These data were used to calculate mold heat transfer, monitor slab length, double-check the PDA data, monitor superheat, and to discover disturbances in the casting process.

4.2.1 Nailboard Measurements

During the course of the project, 47 individual nailboard tests were performed. Three sets of nailboards were initially constructed in order to account for three different width ranges: 985-1100 mm, 1100-1280 mm, and 1280-1460 mm. Individual boards measured 45 mm across and 12.5 mm thick for the east and west halves of the mold. Four number 20 common nails were driven through each at about 20, 85, 225, and 315 mm from the narrow face of the mold. Following placement of the four nails, a length of 2.5 mm diameter aluminum wire was placed next to each nail. This was done as prescribed by McDavid and Thomas [18]. The time required to set up each board was about 5-7 minutes. To improve safety, handles were fastened to each board so the measurer could keep face and hands relatively clear of the mold opening to reduce the chance of injury from molten metal splashes, which occur without warning. A small level was tacked to the top of the board to ensure the nails and wires were vertical to eliminate uneven board placement as a source of error during the measurement. The nails were immersed in the mold from 5-7 seconds. Immersion times shorter than this resulted in not being able to obtain measurements where immersion times that were longer resulted in complete melting and loss of the nails into the mold. Finally, 15 to 20 minutes additional time were required for the nails to cool down to make and record measurements, depending upon the condition of the nails following immersion. Initially, the only measurements made were the distances from the top of

the steel knob on the nail to the bottom of the board and the length of aluminum wire left (to determine flux depth). This time for measuring and recording increased slightly as more measurements were made on the nails, especially for steel knob diameter and the angle at the top of the steel knob.

4.3 Slag Sample Collection

For a few heats during the February 2001 trial, slag samples were obtained from the Ladle Metallurgical Facility (LMF) for the ladle slag, from the tundish, and from the mold. The compositions of the slags were measured using x-ray fluorescence (XRF).

It was found that getting slag samples for every heat from all processing locations was impracticable for one person while making nailboard measurements, which are time consuming. Since the same slag-forming materials were still in use during subsequent trials, it was assumed that the XRF analyses were still valid. Slag samples were therefore only collected for the trials of February 14-15, 2001.

4.4 Steel Sample Collection

In addition to data collection and physical measurements, samples were collected throughout the processing of the material. Samples of as-cast, hot-rolled, skin-passed, pickled, cold-rolled, and galvanized steel product were collected, inspected, and analyzed with the goal of relating the occurrence of defects to events in the mold. Steel composition data were also collected through a level two database, but this could be done at any time following casting and was very easy to accomplish (table 4.4).

Scheduling proved to be an important obstacle in obtaining these samples. Customer requirements and equipment availability often dictated how casting sequences were set up. To collect rolled samples and perform inspection and analysis it was common to wait for days or weeks for the opportunity to do so. This was primarily due to mill scheduling, particularly on the reversing mill and slitter line, where the inspections were performed.

CHAPTER 5: RESULTS OF INDUSTRIAL PLANT TRIALS

This chapter presents the results of the trials performed in this work. In particular, this section will describe the results of the measured plant data of metal level and the other casting parameters and the measured results of the nailboard experiments and briefly discuss the inspection and evaluation of slab and strip samples collected during the course of the trials. Strip quality and defect composition consisted of visual and EDX analyses coupled with fast Fourier transform (FFT) analysis using Microcal Origin of the metal level data to identify the frequencies at which events in the casting mold occurred [52]. Detailed analysis of the data, discussion of the effect of mechanical and fluid flow transients upon slag emulsification and sliver defect formation, and the calculation of the steel stream velocity will be covered in the following chapters.

5.1 Metal Level Measurements

Metal level in the mold is influenced by numerous other variables of the casting process. If a casting variable has an adverse effect upon metal level, it was expected that it should exhibit some periodic behavior with and associated identifiable frequency of the metal level fluctuations. For the first trial (case 1), conducted during June and July 2000, data were collected solely by way of level two for every 0.94 meters cast as discussed in chapter 4. Table 5.1 presents a typical body of data collected during the experiments. The data analysis showed that important events were much shorter than this, so the June 2000 data were deemed unsuitable for numerical analysis, but was still employed in the evaluation of the nailboard measurements and defect samples.

5.1.1 High Frequency Data

For the second trial (case 2) in February 2001, data were collected at 30 millisecond intervals to ensure all events with an occurrence frequency of up to 16.67 Hz would be recorded [9, 49-50]. 16.67 Hz is the maximum because the FFT analysis can distinguish frequencies having at most half of the sampling frequency.

Because of the high sampling frequency, there exists an extremely large body of data for every heat. With ten parameters recorded at 33.33 Hz, 1.2 million numbers were collected

Table 5.1: Sample of Level Two Data. Note: Unless otherwise noted, all temperatures are Fahrenheit and water flows in units of gallons per minute.

Heat	Time	Caster	Mold Water Temperature In	Mold Water Temp. Fixed Out	Mold Water Temp. Loose Out	Mold Water Temp.East Out	Mold Water Temp.West Out	Water Flow Fixed (North)	Water Flow Loose (South)	Water Flow East	Water Flow West
213760	6/12/01 6:25	CAS2	100.4	118.4	118.5	117.6	120.1	1208	1180	29	29
213760	6/12/01 6:25	CAS2	100.4	118.4	118.5	117.6	120.1	1192	1180	29	29
213760	6/12/01 6:25	CAS2	100.4	118.4	118.5	117.6	120.1	1205	1183	29	29
213760	6/12/01 6:25	CAS2	100.4	118.4	118.5	117.6	120.1	1199	1182	29	29
213760	6/12/01 6:26	CAS2	100.4	118.4	118.5	117.6	120.1	1203	1178	29	29
213760	6/12/01 6:26	CAS2	100.4	118.4	118.5	117.6	120.1	1203	1182	29	29
213760	6/12/01 6:26	CAS2	100.4	118.4	118.5	117.6	120.1	1208	1181	29	29
213760	6/12/01 6:26	CAS2	100.4	118.4	118.5	117.6	120.1	1208	1181	29	29
213760	6/12/01 6:26	CAS2	100.4	118.4	118.5	117.6	120.1	1196	1181	29	29
213760	6/12/01 6:26	CAS2	100.4	118.4	118.5	117.6	120.1	1220	1187	29	29
213760	6/12/01 6:26	CAS2	100.4	118.4	118.5	117.6	120.1	1208	1182	29	29

Table 5.1 continued: Sample of Level Two Data.

Heat	Time	Cast Speed (ipm)	Width (inches)	Thickness(inches)	Tundish Temperature	Metal Level Setpoint (in)	Metal Level (in)	Stopper Rod (in)	Oscillation Frequency (cpm)	Sequence Length (in)	East Taper (mm)	West Taper (mm)
213760	6/12/01 6:25	200	47.44	1.96	2830	3.49	3.49	2.38	330	77688	2.81	2.81
213760	6/12/01 6:25	200	47.44	1.96	2830	3.49	0.00	2.38	333	77724	2.81	2.81
213760	6/12/01 6:25	200	47.44	1.96	2830	3.49	3.50	2.38	342	77760	2.81	2.81
213760	6/12/01 6:25	200	47.44	1.96	2832	3.49	0.00	2.36	335	77796	2.81	2.81
213760	6/12/01 6:26	200	47.44	1.96	2833	3.49	3.50	2.38	334	77832	2.81	2.81
213760	6/12/01 6:26	200	47.44	1.96	2834	3.49	3.49	2.38	347	77868	2.81	2.81
213760	6/12/01 6:26	200	47.44	1.96	2835	3.49	3.50	2.39	341	77904	2.81	2.81
213760	6/12/01 6:26	200	47.44	1.96	2835	3.49	3.50	2.39	341	77915	2.81	2.81
213760	6/12/01 6:26	200	47.44	1.96	2836	3.49	3.49	2.39	333	77940	2.81	2.81
213760	6/12/01 6:26	200	47.44	1.96	2837	3.49	3.51	2.37	330	77976	2.81	2.81
213760	6/12/01 6:26	200	47.44	1.96	2839	3.49	0.00	2.37	334	78012	2.81	2.81

for every hour of caster operation and for the 26 heats for which PDA data exist there is a total of 3.12×10^7 numbers recorded. For the sake of space, only representative portions of the collected data will be presented here. Figure 5.1 shows a typical plot of metal level vs. time for one hour of casting and table 5.2 shows a sample of PDA output.

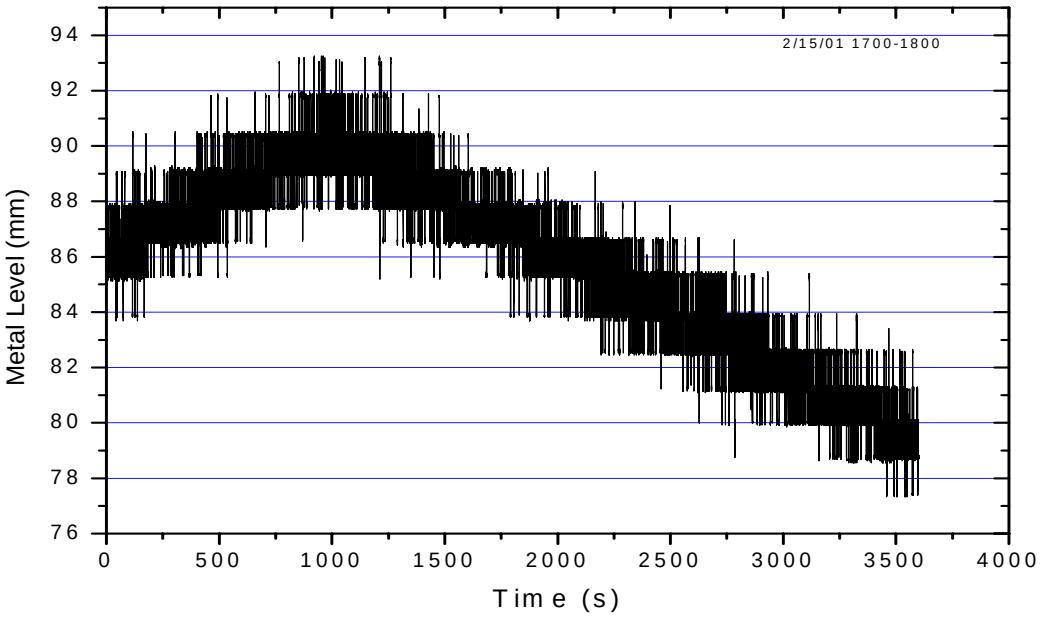

Figure 5.1: Typical Plot of Metal Level vs. Time for 1 Hour

The step-like appearance of the plot is due to the deliberate variation of the metal level setpoint by 1.0 mm every minute between levels of 40 and 90 mm, which is done to maximize the service life of the submerged entry nozzle (SEN) by spreading the erosion band at the metal-slag-refractory interface over a wider area of the lime-stabilized zirconia layer of the SEN wall.

As figure 5.1 illustrates so many data, which also include short-time scale events, it is necessary to look at metal level behavior over shorter times. One minute (60s) of data, such as shown in figure 5.2, reveals that the metal level is constantly fluctuating both above and below the setpoint. Causes of these measured deviations from metal level setpoint include events above, in, and below the mold. In this project, they are divided into two categories: 1) mechanical transients from downstream and 2) fluid flow effects from upstream.

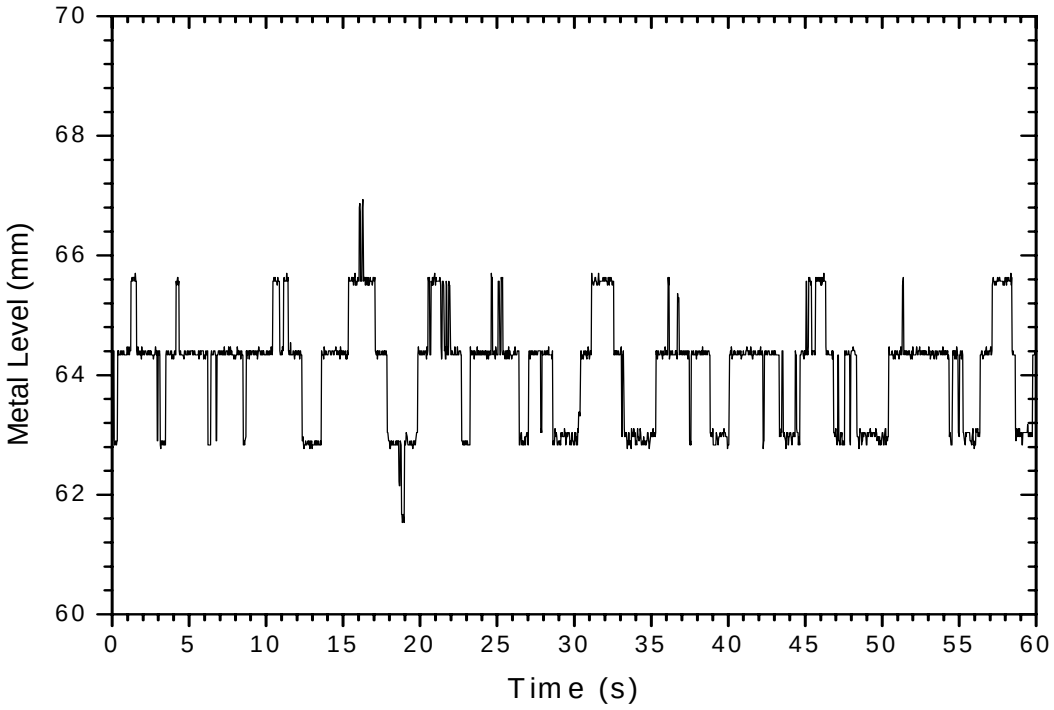

Figure 5.2: Metal Level vs.Time for one minute of casting time.

Mechanical transients include such behavior as bulging, slab shear cuts, oscillator effects, metal level setpoint changes, and alignment issues. They affect level by causing disturbances low in the liquid pool.

Flow-related fluctuations depend upon mold and SEN geometry, SEN submergence, sudden stopper rod changes, mold width, clogging, casting speed, and turbulent fluctuations in the mold [5,6]. Such fluctuations are caused by upstream variations in operating variables such as speed, width, and grade changes and also by transients in turbulence, unstable configurations, and perhaps by the jet of steel exiting from the SEN port being directed too much upward.

5.1.2 Nailboard Measurement Data

A sample of nailboard measurements is presented in tables 5.3a and 5.3b. For every measurement, the distance of each nail from the narrow faces and the mold center was determined. The higher number of the submergence measurements is the distance (in mm) from the top of the mold flux to the lowest point on the bulb of steel and the lower number is the

Table 5.2: Sampling of Casting Data as Obtained through the PDA Data Acquisition System.

Time(s)	Metal Level (mm)	Level Setpoint (mm)	Cast Speed (ipm)	West Stopper Rod (mA)	East Stopper Rod (mA)	Pinch Roll 1 Speed (ipm)	Pinch Roll 1 Current (Amps)	Pinch Roll 2 Speed (ipm)	Pinch Roll 2 Current (Amps)	Raw Level Signal (mA)
0	62.9029	63.9966	160.065	5.81079	7.71023	160.602	2.65324	159.394	11.5948	8.27176
0.03	62.9029	64.2017	159.931	5.79614	7.71023	160.2	-0.02649	159.26	12.3331	8.262
0.06	62.9712	64.065	159.931	5.81079	7.72488	160.737	8.55E-04	160.871	5.55172	8.27176
0.09	64.4068	64.2017	159.797	5.79614	7.70535	161.139	0.11023	161.542	3.80169	8.28153
0.12	64.4068	64.2017	159.797	5.81079	7.71511	161.005	2.65324	159.797	11.7315	8.26688
0.15	62.8345	64.065	160.065	5.80591	7.70535	160.602	3.20012	157.648	14.4386	8.28641
0.18	62.8345	64.2017	159.797	5.79614	7.70047	160.602	0.0282	158.991	13.6729	8.27665
0.21	62.9029	64.1334	159.931	5.80591	7.71511	161.139	0.05554	160.468	5.74313	8.28153
0.24	62.8345	64.065	160.065	5.81079	7.71511	160.468	0.0282	159.394	5.82516	8.262
0.27	62.8345	64.2701	160.871	5.80591	7.70535	161.677	2.21573	161.005	11.4034	8.2913
0.3	62.9029	64.2017	161.005	5.81079	7.71511	160.737	3.0634	161.811	9.73538	8.27665

Table 5.3a: Measured Values of Distance from Bottom of Nailboard to the Meniscus and Flux Depths. Note: Numbers arranged as (Upper Level/Lower Level/Flux Depth). Units are millimeters.

Heat	East Edge	East Quarter	East Half	East SEN	West SEN	West Half	West Quarter	West Edge
213760	58/63/4	55/71/6	66/74/7	68/77/7	65/71/5	55/70/9	47/62/6	40/50/6
117004	55/65/5	60/66/4	64/71/4	59/70/4	62/71/4	54/67/6	44/56/6	40/48/7
117005	30/42/7	40/48/6	45/48/6	45/49/6	55/61/9	41/58/5	33/48/8	25/29/3
117006	31/45/6	39/48/6	42/50/9	47/51/4	58/60/7	47/56/6	42/53/4	42/51/4
213763	30/40/4	37/53/5	48/55/5	51/55/12	50/56/8	50/60/5	44/53/3	37/50/8
117021	46/56/4	49/57/5	55/63/7	58/68/5	50/60/5	47/57/4	42/58/5	42/53/5
117022	35/42/4	34/47/7	46/54/5	52/57/5	45/52/6	40/49/6	32/45/8	25/37/5
117023	47/53/4	50/55/5	50/61/5	50/57/5	53/66/8	45/57/7	40/50/4	36/42/5
117024	40/56/6	49/60/6	52/65/9	60/65/7	57/70/7	53/58/5	47/54/5	42/48/5
117025	75/79/4	73/78/7	70/80/6	70/77/7	68/78/11	62/67/4	62/67/4	60/65/5
117026	51/60/4	55/60/5	56/64/6	61/70/7	55/61/7	53/62/4	52/60/5	47/52/7
213782	42/550/5	45/54/5	45/52/5	47/55/5	49/55/6	47/56/6	47/55/7	43/55/6
213783	35/35/5	40/45/10	37/53/8	45/53/8	49/57/6	43/54/3	40/44/5	35/41/8
213784	36/45/5	42/46/5	42/53/7	54/63/8	51/62/7	46/52/3	45/51/7	43/48/5

Table 5.3b: Measured Steel Knob Diameters. Units are millimeters.

Heat	East Edge	East Quarter	East Half	East SEN	West SEN	West Half	West Quarter	West Edge
213760	10.7	9.66	10.9	9.71	11.54	9.88	8.84	10.9
117004	11.18	8.76	9.52	8.76	13.47	10.46	9.83	9.37
117005	12.91	11.22	12.97	11.78	15.39	12.27	11.91	11.85
117006	13.22	14.06	12.96	13.24	11.41	14.22	17.57	13.76
213763	12.37	11.99	13.77	13.67	12.14	14.26	12.18	13.45
117021	12.18	10.8	14.66	12.87	15.31	16.72	14.2	14.81
117022	13.02	12.86	12.17	14.63	12.23	16.17	13.29	12.15
117023	13.12	12.86	15.22	11.44	14.98	13.14	15.9	14.27
117024	13.42	16.8	12.22	12.26	16.38	10.57	11.05	10.9
117025	12.18	9.37	11.29	9.87	11.08	14.88	13.64	15.07
117026	13.36	12.67	11.93	10.51	9.19	15.24	20.06	15.7
213782	15.42	14.51	12.13	15.55	13.04	13.23	13.68	14.14
213783	12.79	10.65	11.79	10.45	10.11	14.48	14.06	12.07
213784	14.27	12.85	11.54	12.31	11.35	16.14	12.65	12.35

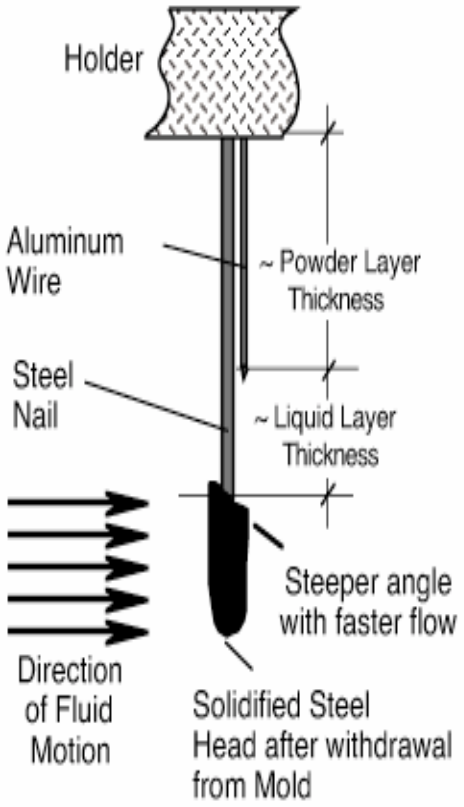

Figure 5.3: Schematic of Nailboard Setup Used for Mold Measurements [18].

distance from the top of the mold flux to the highest point on the bulb of steel. These numbers describe the meniscus height and the effect of flow past the nail. It should be noted that an average of the high and low number was used for each nail when calculating the standing wave height. The measurement of the distance from the bottom of the aluminum wire to the top of the steel knob provides flux depths. In addition, the maximum diameter of the steel bulb was measured. These three measurements are used to calculate the steel velocity across the meniscus (see Figure 5.3).

5.1.3 Other High Frequency Data

Other data collected every 30 milliseconds using the PDA include pinch roll speeds and currents, tundish stopper rod position, casting speed, and the raw electrical signal for metal level. The signals/levels were calibrated on a 4-20 mA scale, meaning five to zero for the stopper rod and 189 to 40 mm for the metal level. This is summarized in table 5.4. These data are correlated with metal level and defect signals for the identification of transients. Examples of data are presented in figures 5.4 through 5.10.

5.2 Slag Samples

Slag samples from the ladle, tundish and mold were collected during case 1 measurements and observations. As slag practices and materials were not changed throughout the project, it was assumed that these values were valid for all heats. The slag composition allows for the determination of whether a defect originated in the ladle, tundish, or mold. Tables 5.5, 5.6, and 5.7 present average slag compositions for ladle, tundish, and mold slag, respectively.

5.3 Steel Samples

Samples from the steel produced during the experiments were obtained when practicable from the hot-rolling mill, the pickling line, or the cold-rolling mill. Table 5.8 lists the samples obtained during the trials. Details will be discussed in the next chapter.

5.4 Mold Meniscus Brass Measurements and Oscillation mark spacing.

Further quantification of metal level standing wave position was obtained by inspecting mold plate hot faces following casting. In several circumstances, a brass layer was visible as a bright yellow stain on the surface of the reddish-colored Cu-Ag alloy of the mold plate. Small amounts of zinc in the liquid steel preferentially diffuse into the copper alloy to form the brass. The shape of this brass discoloration is roughly comparable to the standing wave values obtained through nailboard measurements, but since the metal level is varied to maximize SEN service this could not be quantified very well. Only the general shape of the meniscus can be observed due to the gradual change from brass discoloration to the Cu-Ag alloy of the mold plate. The obtaining of oscillation mark profiles involved measuring the peak-to-trough distance. Since the

formation of individual oscillation marks is influenced by meniscus shape, such profiles provide another pool of data with which to compare meniscus profiles obtained by other methods (see Table 5.9 and Figure 5.11) [53-54].

Table 5.4: Values used for linear conversion of metal level and stopper rod raw signals.

Signal	4 mA Value	20 mA Value
Stopper Rod (inches)	5	0
Metal Level (mm)	189	40

Table 5.5 Average Ladle Slag Composition following Tap (27 Heats).

Slag Component	Avg. Wt. %	Standard Deviation
CaO	31.7	3.3
MgO	7.1	1.4
SiO_2	8.4	2.2
Al_2O_3	2.8	1.1
FeO	37.7	8.8
MnO	3.9	0.7
C/S Ratio	3.0	0.9

Table 5.6: Average Tundish Slag Composition (10 Heats).

Slag Component	Avg. Wt. %
Al_2O_3	31.59
MgO	14.63
Na_2O	0.92
Fe_2O_3	1.52
MnO	0.09
TiO_2	1.47
Cr_2O_3	0.24
CaO	37.20
SiO_2	9.52
V-Ratio	3.98
S	0.04

Table 5.7: Average Mold Slag Composition (24 Heats).

Slag Component	Avg. Wt. %	Standard Deviation
Na_2O	9.72	0.46
MgO	2.06	0.44
Al_2O_3	6.52	0.58
SiO_2	35.27	0.36
K_2O	0.21	0.04
CaO	34.87	0.24
TiO_2	0.05	0
MnO_2	1.47	0.15
Fe_2O_3	1.63	2.18
ZrO_2	0.19	0.09
P_2O_5	0.13	0.03
SO_3	0.18	0.11
V-Ratio	0.99	0.013
Alumina Pick-Up	0.72	0.58

Table 5.8: Defect Samples Collected during Inspection. (OS-Operator Side, DS-Drive side)

Coil #	Gauge (mm)	Defect Location	Appearance/Cause	Comments
299485	0.48	Top, 0.25 m in from OS Top, 0.3 m in from OS	1.4 m long sliver 0.25 m long sliver	Mold powder Mold powder
297189	0.48	2, top, 0.3 m in from OS	2 – 1.4 m long slivers	Mold powder
298440	0.48	0.5 m in from OS, 10350' from head end top	0.37 m sliver	Mold powder
295367	0.48	41 defects, 0.2 to 0.3 m in from DS top	0.23 to 0.62 m long slivers	All mold powder, delaminated
295370	0.48	None	N/A	clean
294655	0.48	None	N/A	clean
297192	1.45	3 defects, OS top, DS top, OS top	0.08, 0.87 and 0.38m slivers	Mold powder, delaminated scab appear.
298537	0.77	2 defects, OS top	0.18 and 0.04 m long pitted	Rolled-in scale, trace mold powder
300115	0.48	Repeating defect every 1.44 m	Roll mark	Rolled-in scale
300116	0.48	None	N/A	N/A
300069	2.03	4 elliptical defects, 0.45 m in from OS, 0.59 m in from DS	0.13 to 0.25 m long line defects, black color	Mold powder and rolled-in scale

Table 5.9: Comparison of Standing Wave Height as Estimated by Oscillation Mark Measurements with Nailboard Meniscus Measurement for heats where slab samples were available. Oscillation mark measurements were peak-to-trough. See also Figure 5.11.

	Oscillation Mark Measurements (mm)			**Meniscus Measurements (mm)**	
Heat/Slab ID	**West**	**East**		**West**	**East**
211248-01	18	22		12	29
211248-04	20	18		14	13
211249-01	14	17		19	22
114376-06	22	n/a		25	22

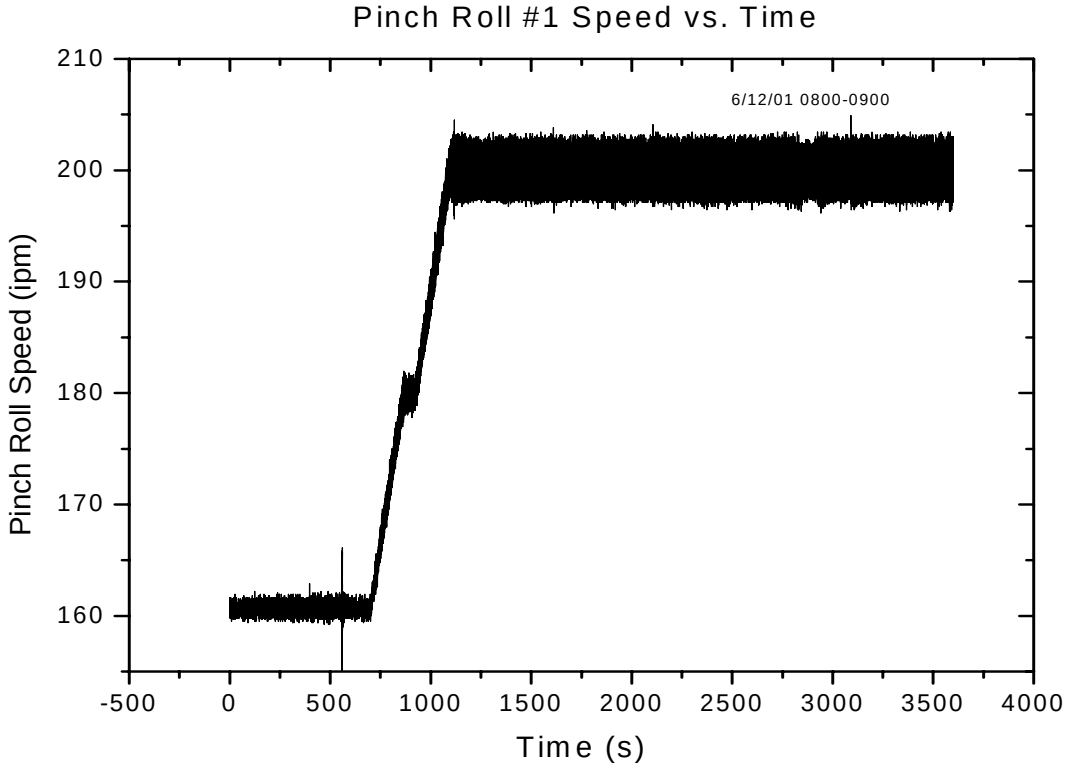

Figure 5.4: Plot of pinch roll #1 speed vs. time.

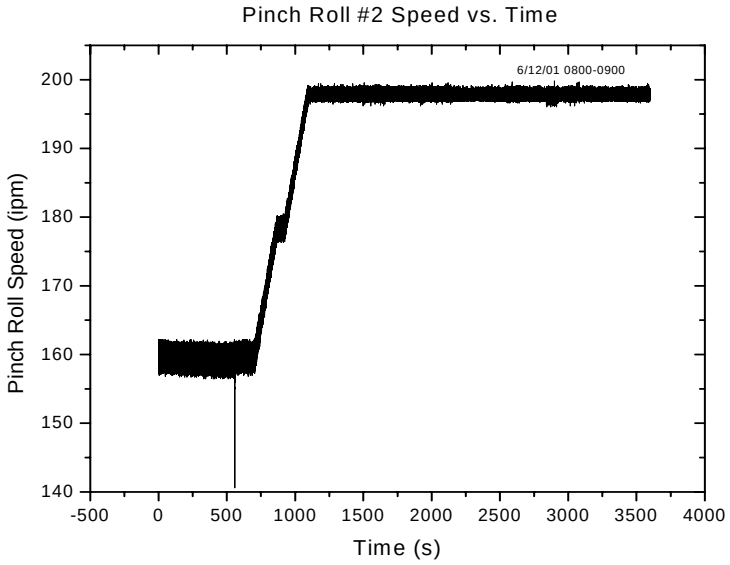

Figure 5.5: Plot of pinch roll #2 speed vs. time.

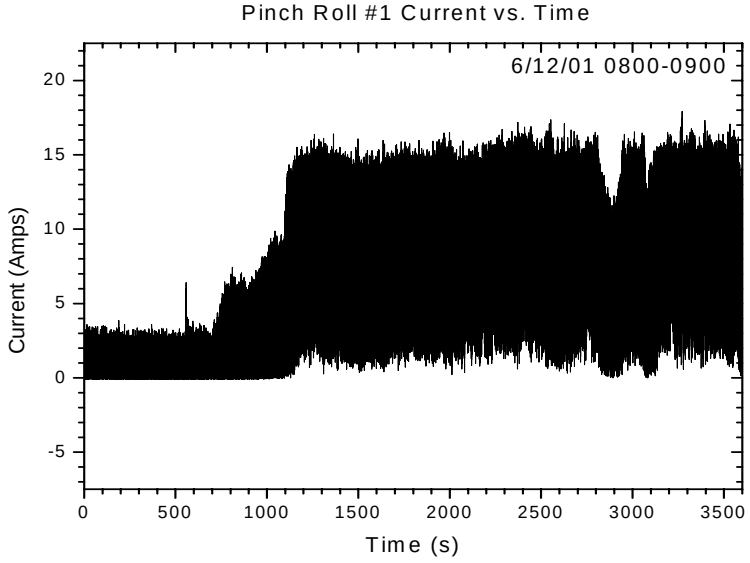

Figure 5.6: Pinch Roll #1 Current vs. Time for 1 Hour of casting.

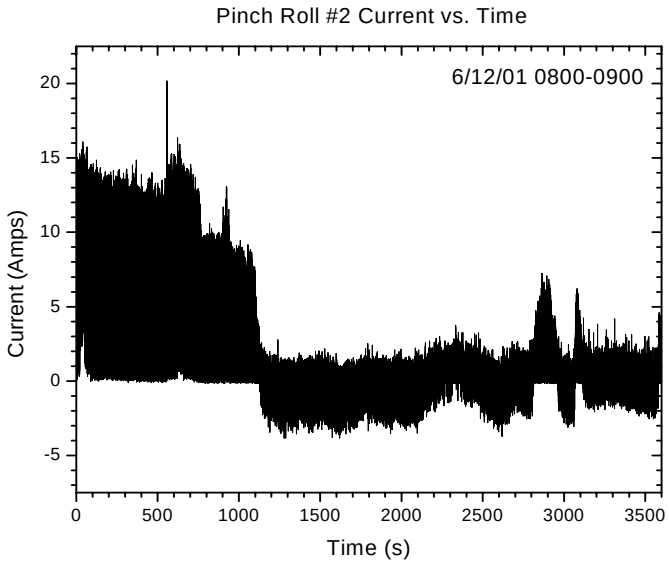

Figure 5.7: Pinch Roll #2 Current vs. Time for 1 Hour of Casting.

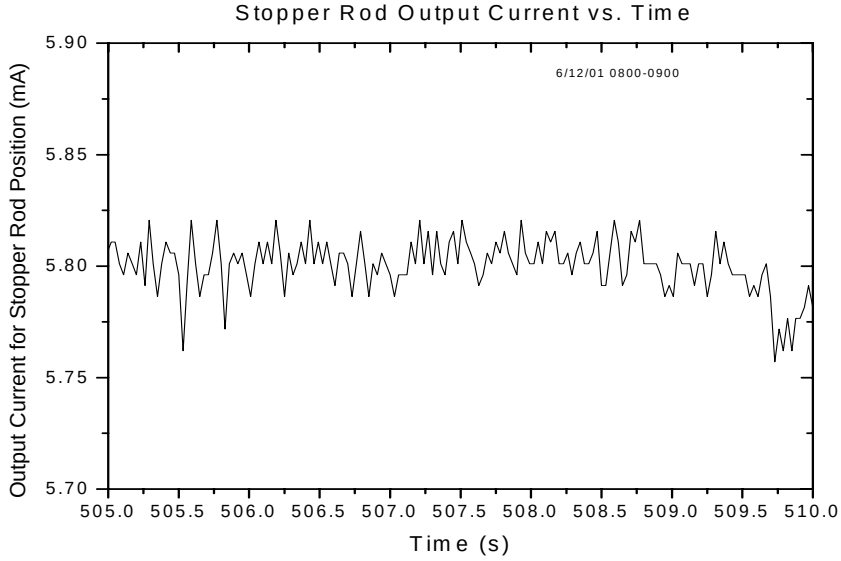

Figure 5.8: Plot of stopper rod output current vs. time.

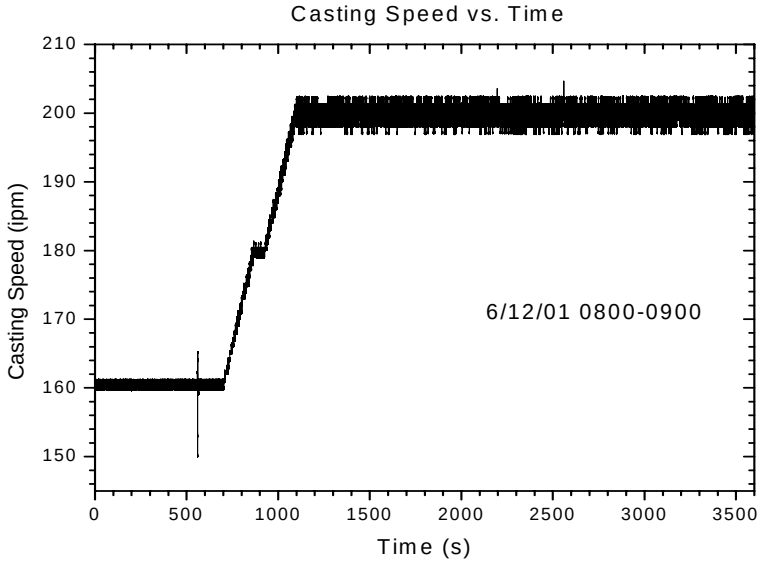

Figure 5.9: Casting Speed vs. Time as Gathered from PDA system.

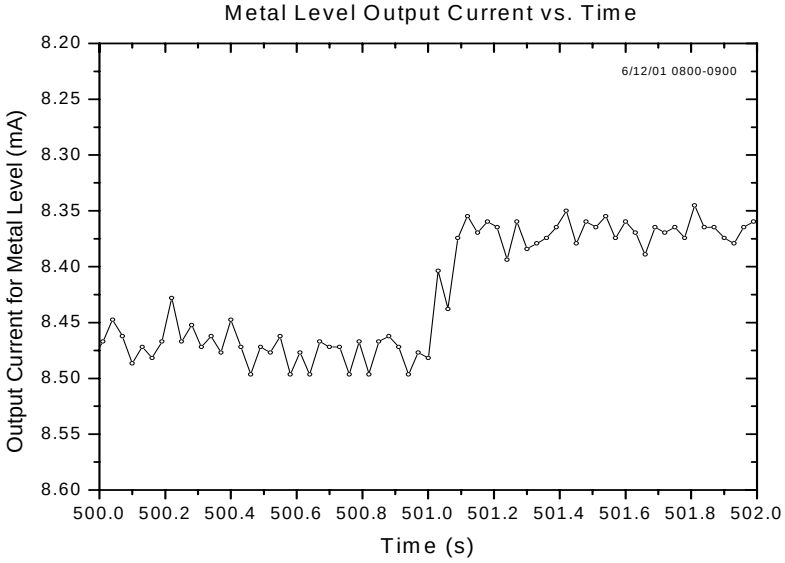

Figure 5.10: Raw Electrical Signal for Metal Level vs. Time (Sampling Rate = 33.33 Hz)

Figure 5.11: Oscillation mark appearance on a slab 114376-06. Marks are measured peak-to-trough and compared to nailboard standing wave measurements. The troughs of the above oscillation marks are not visible due to sample size.

CHAPTER 6: ANALYSIS AND DISCUSSION

The purpose of this discussion is to establish and evaluate the effects of normal CSP caster operation on the metal level, meniscus shape, and meniscus flow behavior including steel flow velocity. Effects include transient occurrences due to both mechanical and fluid flow behavior.

6.1 FFT Generation

In order to detect effects upon metal level fluctuations and the frequencies at which they occur, fast Fourier transforms (FFT) were performed on each set of metal level fluctuation data. To better illustrate and understand, "perfect" test data were constructed with single-line peaks at two frequencies. The test data point frequency was chosen to match that of the actual caster data. From the generated FFT plots of the constructed test data, an equation was developed to calculate the metal level fluctuation in the time domain from the information contained in the frequency domain:

$$X_{fd} = (X_{td} / t_s)* t_t *f \qquad (6.1)$$

where the variables are defined in the nomenclature section.

6.1.1 Use of Constructed data for Validation of Equation 6.1

In order to validate/verify equation 6.1, it was necessary to construct perfect sets of metal level fluctuation data with known periods and amplitudes. This was accomplished by adding the equations for two distinct sine waves to result in a curve similar to the raw metal level data (see Figure 6.1). FFT analyses were performed on these sets of data to observe the software's handling of the data (Figure 6.2). The equation for determining time-domain fluctuations from frequency-domain data proved to be suitable for use with sets of real plant data. The calculated numbers do not exactly match because the “perfect” data was in fact generated using random numbers, therefore peaks do not repeat themselves at the predicted intervals. This is manifested in the “skirting” of the FFT peaks. Skirting indicates that a range of frequency values exists and is the primary source of error in the calculation.

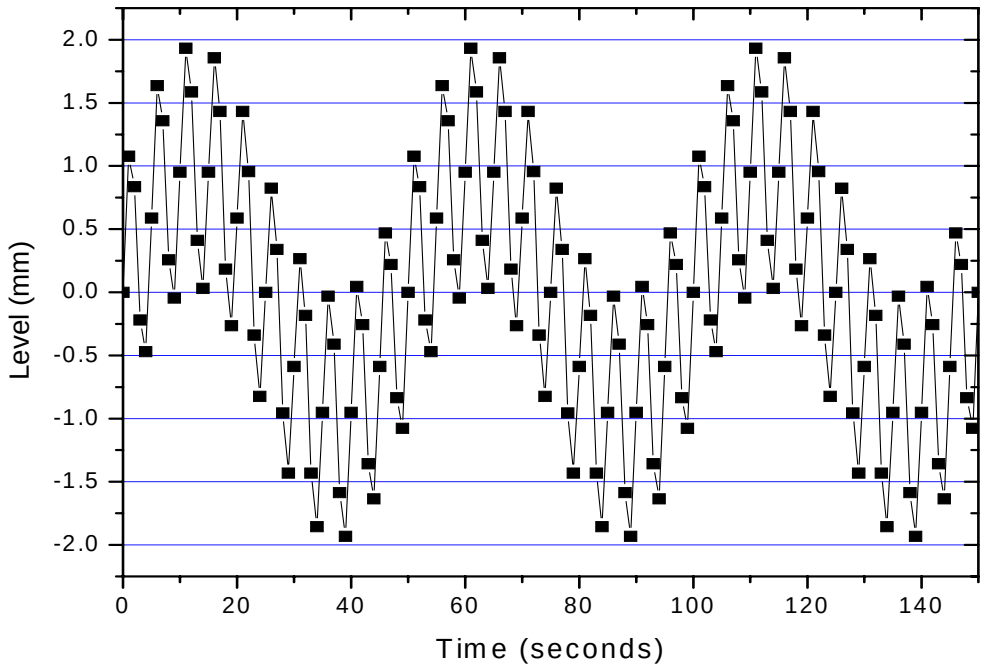

Figure 6.1: Constructed Metal Level vs. Time used for Validation of Equation 6.1.

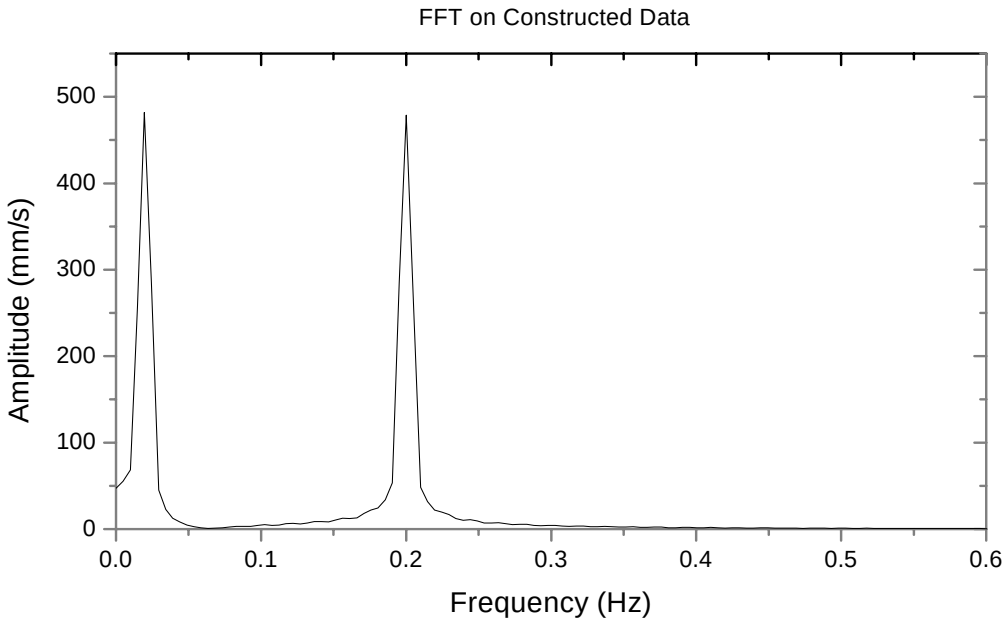

Figure 6.2: FFT Analysis Output Generated Using Constructed Metal Level Data from Figure 6.1.

To fully understand how the relationship between values in the time domain and values in the frequency domain works, it is imperative that the following be understood:

[1] Peaks of the same amplitude in the time domain have increased amplitude in the frequency domain as frequency increases. It should be noted that low-frequency transients do not have large amplitude values in the frequency domain because the amplitude in that

[2] domain is also dependent upon the number of occurrences and not only the amplitude of the fluctuation in the time domain. This is important because the magnitude of the low frequency level fluctuations is easy to underestimate. Conversely, if peaks of the same amplitude in the frequency domain have different frequencies, the higher frequency peak will correspond to a lower amplitude in the time domain.

Thus, the largest peaks in the frequency (FFT) domain do not necessarily correspond to the largest metal level fluctuations.

For example, from Figure 6.2 it is known that X_{fd} equals 483.1665 mm/s for both peaks, the time step, t_s is 0.03 seconds, and the total time, t_t is 150 seconds. The frequencies of the low and high frequency peaks are 0.0188 and 0.1998 Hz, respectively. Using equation 6.1, values of 5.14 mm and 0.48 mm are calculated for the low and high frequencies.

6.1.2 Explanation for conversion from raw signal to level fluctuation plots

To facilitate analysis of the metal level data, the data was manipulated so that the deviation from metal level setpoint could be analyzed. This was accomplished by simply subtracting the setpoint value from the actual metal level value. When plotted, data above zero indicates where metal level was closer to the top of the mold while the opposite is true for data below zero (Figure 6.3). Note the large peak in the center of Figure 6.3. This peak is caused by failure of the PDA system to read a metal level value. This was seen to happen at random intervals throughout the project. Upon FFT analysis on this set of data, the software generated a plot of amplitude vs. frequency (Figure 6.4). Normally, when an FFT is performed on a set of data results are generated at both negative and positive frequencies. The frequency ranges from - 1/2 f_s to + 1/2 f_s, where f_s is the sampling frequency. Instead of plotting the mirror image, only the positive portion of the data has been plotted, albeit with the amplitude doubled to account for all events at that frequency.

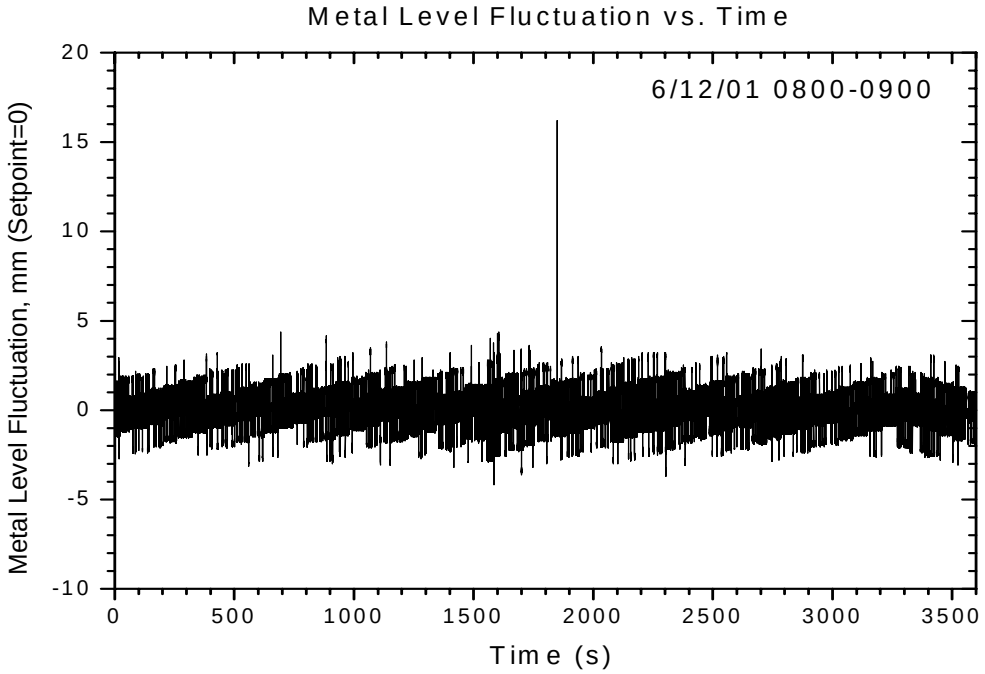

Figure 6.3: One hour plot of Metal Level Fluctuation vs. time.

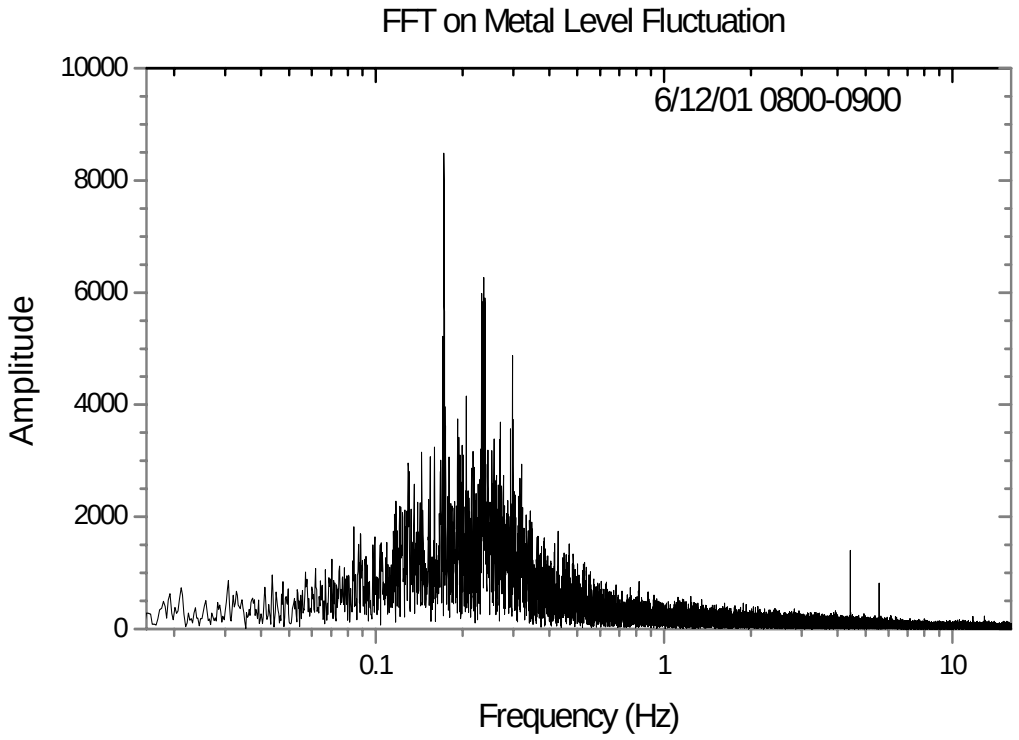

Figure 6.4: An FFT plot of Metal Level Fluctuation (Deviation from Setpoint) as generated.

6.1.3 Mechanical Transient Identification and Characterization

The first step in the identification of mechanical transient effects upon metal level was to calculate the frequencies at which the transients *should* occur. Since roll-bulging and machine-geometry transient effects all are dependent upon casting speed, a table was constructed that calculates the theoretical frequencies at various casting speeds given the known dimensions of the caster (Table 6.1). For mechanical transients caused by roll diameter effects, frequencies were calculated by dividing casting speed by roll circumference. For roll pitch transients, frequencies were calculated by dividing casting speed by the roll spacing. Using Table 6.1 and FFT-generated plots, like Figure 6.4, the frequencies of mechanical transients were identified and catalogued. Figure 6.5 presents labeled frequencies for mechanical transients at casting speeds of 4.06 and 5.08 m/s, which was the range for this data set. It is immediately apparent that almost every mechanical transient matches up roughly with a medium sized peak. However, the theoretical frequencies labeled do not necessarily match up perfectly with peaks on the FFT plot. This is due to the fluctuation of the casting speed during operation. Figure 6.6 shows that the casting speed varies about +/- 0.06 m/min from the setpoint. These speed fluctuations result in the transients occurring over a *range* of frequencies, thereby spreading out some of the peaks.

Table 6.1: Theoretical Frequencies of Mechanical Transients. Roll diameter and pitch values are in millimeters.

Cast Speed (ipm)	Cast Speed (m/min)	Cast Speed (mm/s)	Segment 1 roll diameter	Segment 1 roll pitch	Segment 2 roll diameter	Segment 2 roll pitch	Intersegment spacing
			120	160	160	190	175
			Theoretical Frequency (Hz)				
151.0	3.84	63.92	0.1696	0.3995	0.1272	0.3364	0.3653
152.0	3.86	64.35	0.1707	0.4022	0.1280	0.3387	0.3677
153.0	3.89	64.77	0.1718	0.4048	0.1289	0.3409	0.3701
154.0	3.91	65.19	0.1729	0.4075	0.1297	0.3431	0.3725
155.0	3.94	65.62	0.1741	0.4101	0.1305	0.3454	0.3750
156.0	3.96	66.04	0.1752	0.4128	0.1314	0.3476	0.3774
157.0	3.99	66.46	0.1763	0.4154	0.1322	0.3498	0.3798
158.0	4.01	66.89	0.1774	0.4180	0.1331	0.3520	0.3822
159.0	4.04	67.31	0.1785	0.4207	0.1339	0.3543	0.3846
161.0	4.09	68.16	0.1808	0.4260	0.1356	0.3587	0.3895

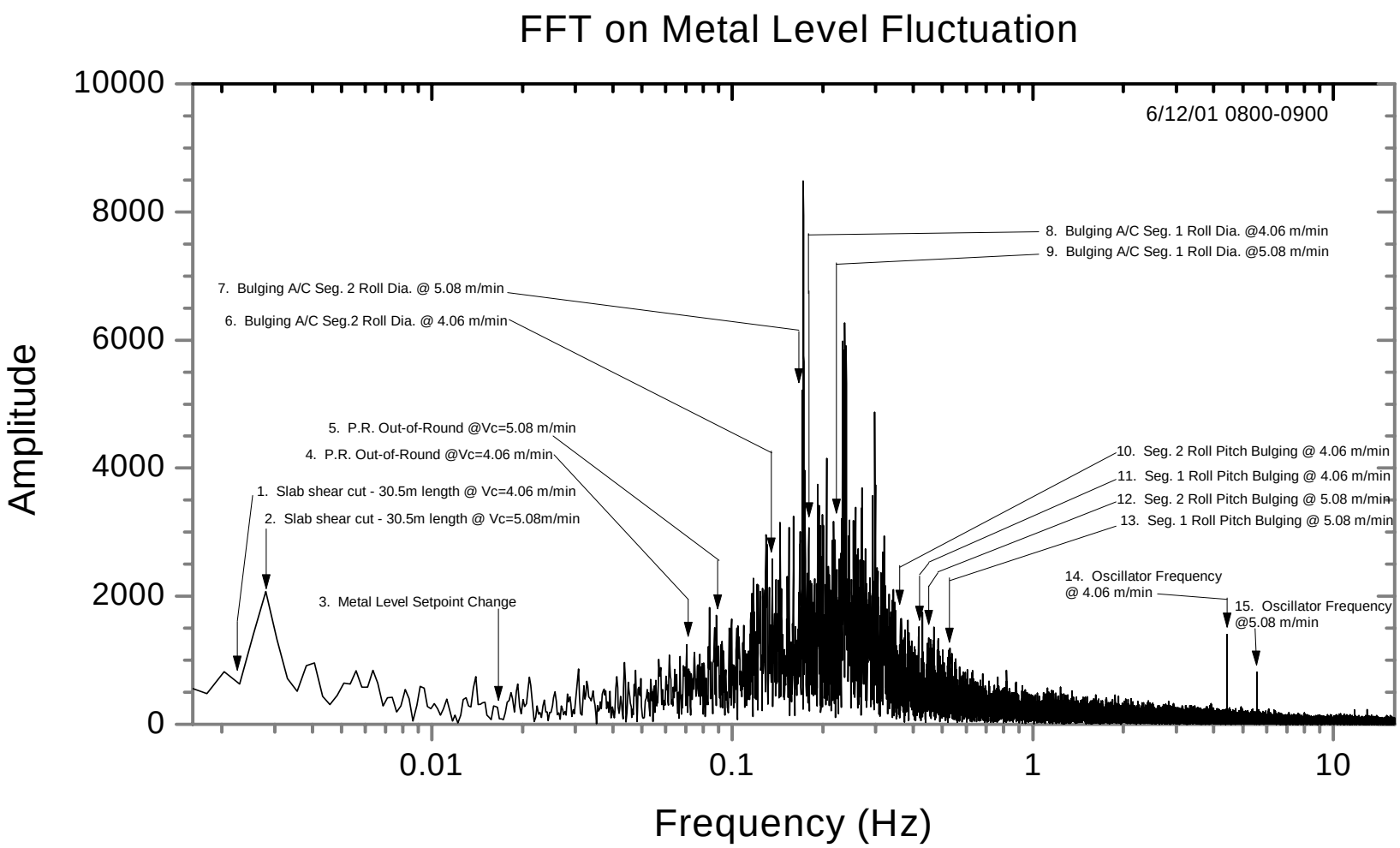

Figure 6.5: Labeled FFT Plot of Metal Level Fluctuation Amplitude vs. Frequency for Mechanical Transients.

Using the peak frequencies and strengths from the frequency domain plots, the corresponding metal level fluctuations were identified in the time domain and the values compared to those calculated. Recalling from 6.1.1 that low frequency peaks are the most significant for a given amplitude, the slab shear cut, with a frequency of 0.0028 Hz for the heat in question, is clearly the transient that caused the greatest metal level deviation with a calculated value of 6.125 mm. This calculated frequency is obtained by simply dividing cast speed by slab length (Table 5.10). Measured values were observed to be approximately 5 mm (see Figure 6.7). It should be noted that Figure 6.7 is a sampling of the data in Figure 6.3.

This was done for all mechanical transients and the results are tabulated in Table 6.2. It should be noted that other peaks that appear associated with mechanical transients are actually due to fluid flow effects.

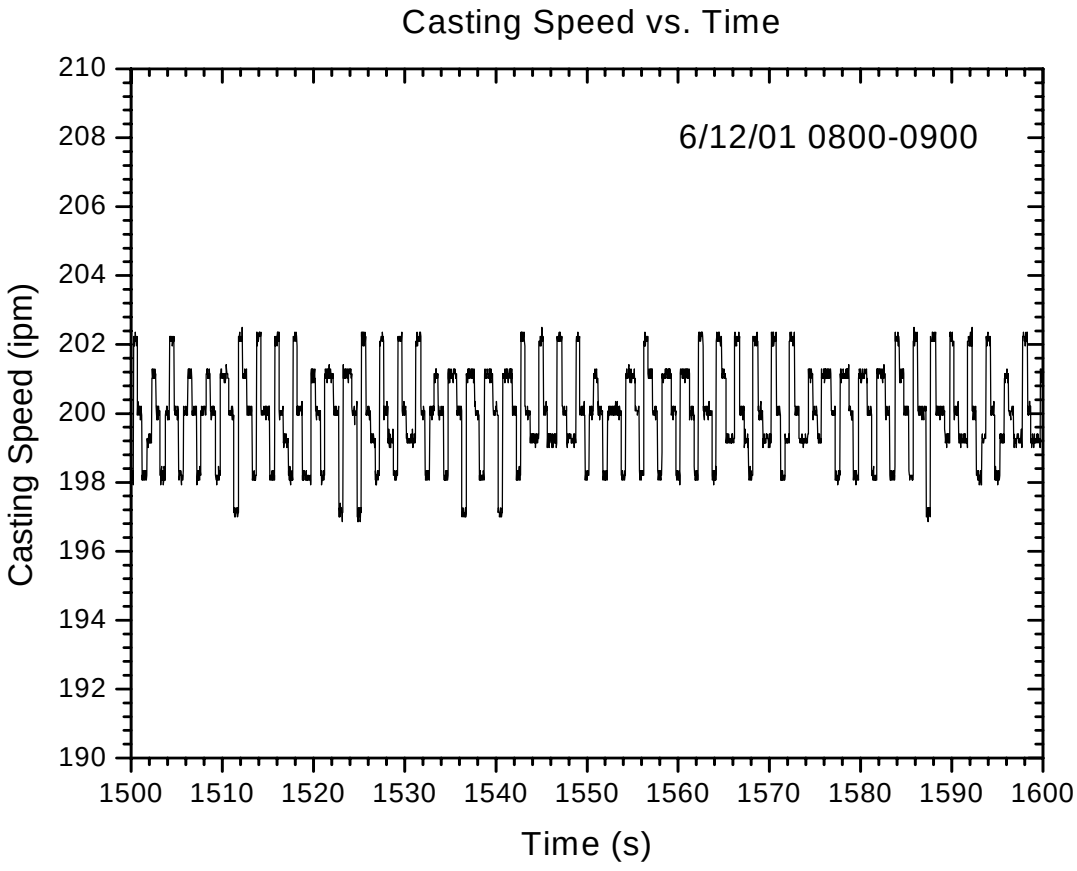

Figure 6.6: Plot of Casting Speed (in inches per minute) vs. Time showing an approximately 0.06 m/min (c. 2.75 ipm) fluctuation in casting speed.

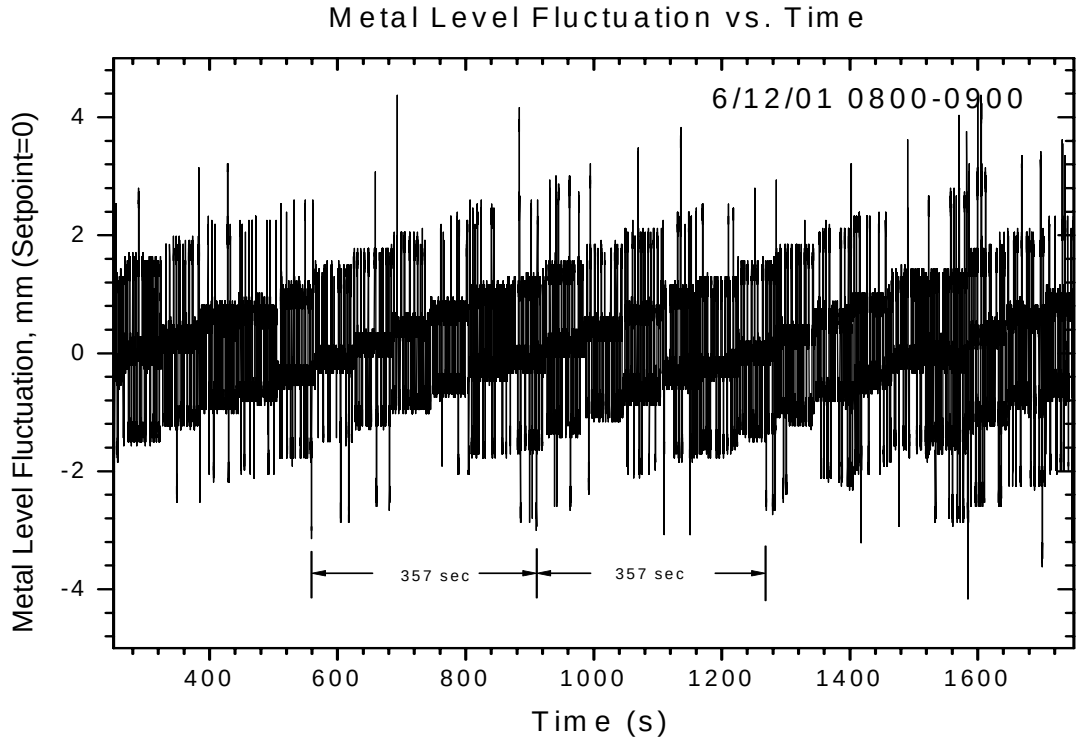

Figure 6.7: Time Domain Plot of Metal Level Fluctuation vs. Time illustrating the period of slab shear cuts 357 seconds apart. This period corresponds to a metal level fluctuation frequency of 0.0028 Hz as labeled in figure 6.6.

6.1.4 Fluid Flow Transient Identification and Characterization

To identify fluid flow transients, it was first necessary to perform FFT analyses upon all data sets. The fluid flow effects of most interest are the oscillation of the standing wave and its dependence upon the residence time of steel in the upper recirculation zone. Using the relationships provided in the literature, flow-related transients were identified and recorded. According to data from Honeyands and Herbertson, the standing wave oscillation is approximately 1.667 times greater than the residence time [6]. Figure 6.8 and Table 6.2 show these transients. The large number of peaks is due to the variation of SEN depth and casting speed during casting. Since average residence time in the upper recirculation zone is dependent upon both variables, their variation can cause significant variation in the oscillation of the standing wave and the peaks have been labeled appropriately. It is recognized that the standing wave does oscillate in the operating CSP mold at frequencies predicted by Honeyands and Herbertson, but not at the amplitude of 40 to 60 mm as

predicted by their water model at a casting rate of 4 m/min (2.5 t/min) [6]. The standing wave oscillation in this project was found to be between 0.2 and 0.3 Hz with a fluctuation magnitude of about 6 mm. This could be due to water being less dense than steel and or there being an appreciable covering of both molten and powder mold flux.

Following identification of the flow transients, equation 6.1 again was employed to determine the amplitude of the meniscus level oscillations in the time domain. These results are compared against the real-time metal level data to determine whether these amplitude values calculated from FFT data agreed with the observed behavior. The calculated and measured amplitudes values are summarized in Table 6.2. The calculated results are very similar, but tend to underestimate the amplitude values in the time domain. This happens because of the variation of variables like casting speed and SEN submergence, which also causes the frequency range in the in FFT plots.

These frequency "ranges" can be either large or small, depending upon the magnitude of the variation in the time domain. For example, for a submergence difference of 29 mm (296 mm to 267 mm) and a casting speed of 5.08 m/min, the frequency range for standing wave oscillation varies from 0.172 to 0.190 Hz (or periods of 5.83 and 5.26 seconds, respectively). The effect of casting speed changes is more pronounced, however. For the same submergence values as above, but with a casting speed of 4.06 m/min the frequency range of standing wave oscillation is between 0.137 and 0.152 Hz (periods of 7.28 and 6.57 seconds, respectively). Considering these frequency ranges, it can be concluded that the FFT is a good tool for identifying and, along with time domain data, characterizing fluid flow induced transient fluctuations in the mold metal level.

Table 6.2a: Mechanical Transients (FFT and Theoretical).

	Frequency Domain (FFT Results)				Theoretical Values		
Peak	**Frequency (Hz)**	**Period (s)**	**Amplitude (mm/s)**	**Amplitude (mm)**	**Frequency (Hz)**	**Period (s)**	**Theor. Amp.(mm)**
1	**0.0020**	**500.00**	**843**	**3.51**	**0.0022**	**454.55**	**3.19**
2	**0.0027**	**370.37**	**2058**	**6.35**	**0.0028**	**357.14**	**6.13**
3	**0.0165**	**60.61**	**278**	**0.14**	**0.0167**	**59.88**	**0.14**
4	**0.0708**	**14.12**	**1258**	**0.15**	**0.0707**	**14.14**	**0.15**
5	**0.0883**	**11.33**	**1737**	**0.16**	**0.0897**	**11.15**	**0.16**
6	**0.1298**	**7.70**	**2959**	**0.19**	**0.1352**	**7.40**	**0.18**
7	**0.1669**	**5.99**	**3023**	**0.15**	**0.1663**	**6.01**	**0.15**
8	**0.1798**	**5.56**	**3081**	**0.14**	**0.1804**	**5.54**	**0.14**
9	**0.2155**	**4.64**	**3180**	**0.12**	**0.2220**	**4.50**	**0.12**
10	**0.3604**	**2.77**	**1672**	**0.04**	**0.3591**	**2.78**	**0.04**
11	**0.4164**	**2.40**	**1536**	**0.03**	**0.4180**	**2.39**	**0.03**
12	**0.4484**	**2.23**	**1365**	**0.03**	**0.4484**	**2.23**	**0.03**
13	**0.5258**	**1.90**	**1208**	**0.02**	**0.5277**	**1.90**	**0.02**
14	**4.4306**	**0.23**	**1415**	**0.00**	**4.4636**	**0.22**	**0.00**
15	**5.5730**	**0.18**	**836**	**0.00**	**5.5526**	**0.18**	**0.00**

Table 6.2b: Mechanical Transients (FFT and Theoretical).

	Frequency Domain (FFT Results)				Theoretical Values		
Peak	**Frequency (Hz)**	**Period (s)**	**Amplitude (mm/s)**	**Amplitude (mm)**	**Frequency (Hz)**	**Period (s)**	**Theor. Amp.(mm)**
16	**0.1358**	**7.36**	**2601**	**0.16**	**0.1373**	**7.28**	**0.16**
17	**0.1549**	**6.46**	**3081**	**0.17**	**0.1523**	**6.57**	**0.17**
18	**0.1714**	**5.83**	**8485**	**0.41**	**0.1716**	**5.83**	**0.41**
19	**0.1926**	**5.19**	**3767**	**0.16**	**0.1902**	**5.26**	**0.17**
20	**0.2319**	**4.31**	**5997**	**0.22**	**0.2288**	**4.37**	**0.22**
21	**0.2571**	**3.89**	**3395**	**0.11**	**0.2537**	**3.94**	**0.11**
22	**0.2971**	**3.37**	**4910**	**0.14**	**0.2860**	**3.50**	**0.14**
23	**0.3205**	**3.12**	**2974**	**0.08**	**0.3170**	**3.15**	**0.08**

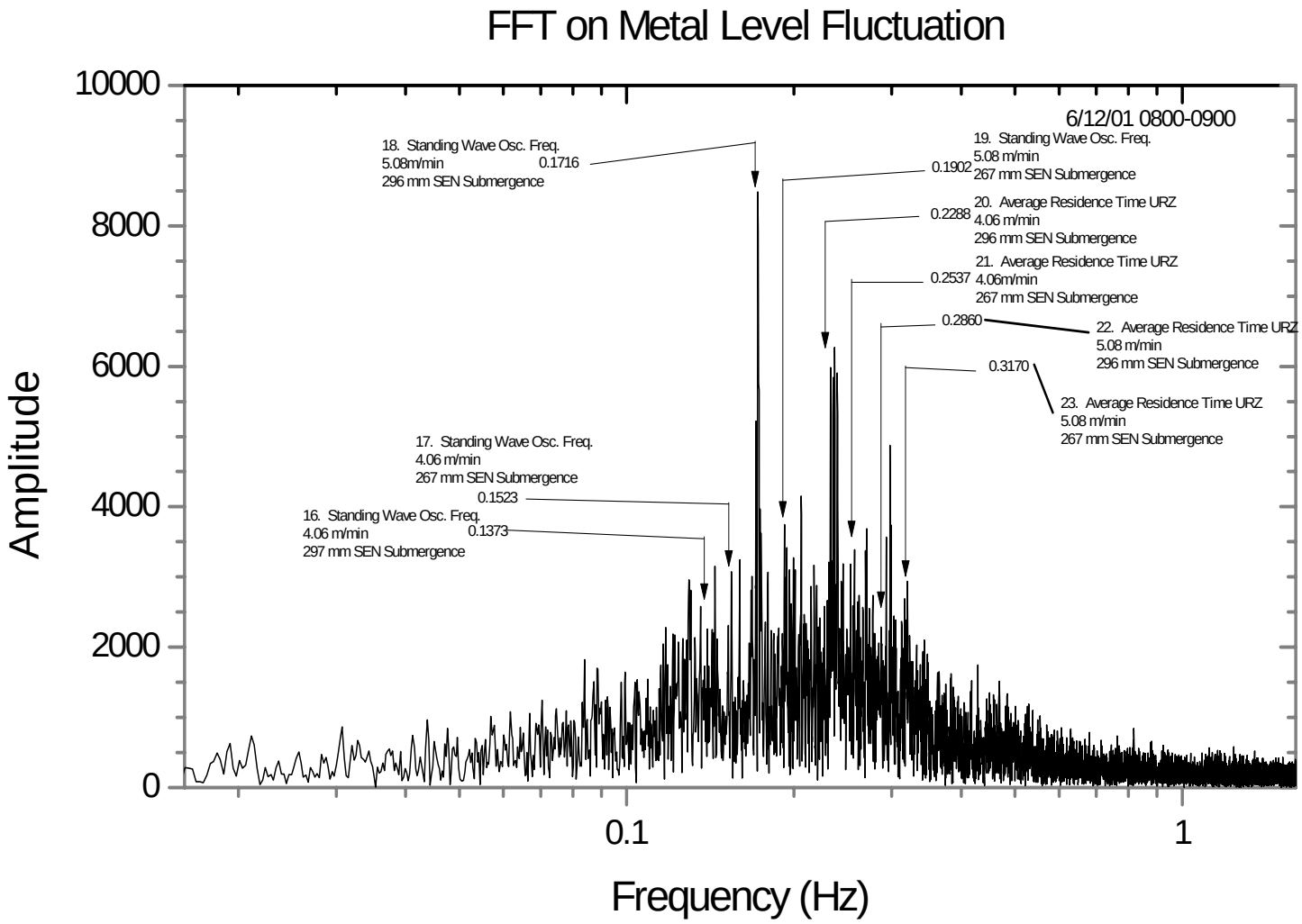

Figure 6.8: Labeled FFT Plot of Metal Level Fluctuation Amplitude vs. Frequency for Fluid Flow Transients. (URZ - Upper Recirculation Zone)

6.2 Nailboards

During the course of this project, the nailboard method emerged as an important tool in the analysis of flow behavior in the thin-slab continuous casting mold. Originally used very effectively as a tool for measuring standing wave shape and flux depths, it was postulated that it could also be used to determine meniscus surface velocity. During the first two plant trials in June-July 2000 and February 2001 nailboard measurements yielded valuable information regarding meniscus shape and flux depths for a wide variety of CSP casting conditions. The extensive meniscus and flux data corroborates findings from both mathematical and physical modeling studies. This corroboration not only includes verification qualitatively, but also includes quantitative observations consistent with the behavior predicted by the models with respect to responses in flow behavior due to changes in key operating variables such as casting speed and SEN design. In addition, some very useful preliminary meniscus velocity results were obtained that contributed much to the further refinement of the measurement technique. Plant trials evolved such that by June 2001, the obtaining of data pertinent to meniscus velocity calculation became the paramount objective of that particular trial. The use of nailboards throughout the course of this study and the refinement of the method to determine meniscus surface velocity quantitatively is believed to be the single most important and groundbreaking result of this project.

6.2.1 Plant Trial Use of Nailboards

Because the nailboard method evolved and was refined throughout the project, the results are discussed according to four major cases. Case 1 consists of the simplest of nailboard measurement results yielding just meniscus/standing wave shape and liquid and powder flux depths. Case 2 nailboard data yields information gathered in case 1 and also observations and measurements relating to the direction of flow. Case 3 data consists of case 1 and 2 data along with limited steel knob diameter data, which was used to generate preliminary meniscus surface velocity data. Case 4 data includes all data necessary for the evaluation of meniscus profile, flux depths, and steel flow characteristics including steel knob diameter data used for the calculation of flow velocities. Case 4 data is divided into two categories - data gathered while casting with a two-port SEN and data gathered while

casting with a four-port SEN. The differences between the two-port and four-port SEN data elucidate the effects of SEN design upon meniscus, flux, and steel flow behavior in the mold.

6.2.2 Case 1 Findings - Meniscus Profile

The most important result of the case 1 data was the establishment of nailboards as a reliable tool for the measurement of meniscus profile and flux depths. Figures 6.9 and 6.10 show that both meniscus shape and flux depths measured are consistent with the findings of other researchers [8,9,18]. As predicted by the literature, the meniscus is highest a short distance in from the narrow face along the centerline of the mold. To avoid confusion, it should be noted that the standing wave is considered to be the difference between the highest and lowest points of the profile. Flux depths vary as expected, being most shallow in areas where the standing wave is highest and deepest in areas where the wave is lowest. This is because the molten flux flows downwards and gathers in the trough of the standing wave. According to Figure 6.9, the typical standing wave height (distance from peak to trough of the steel/flux interface) is about 22 mm. The typical flux depth from Figure 6.10 is about 4-8 mm, but occasionally local depths are much deeper.

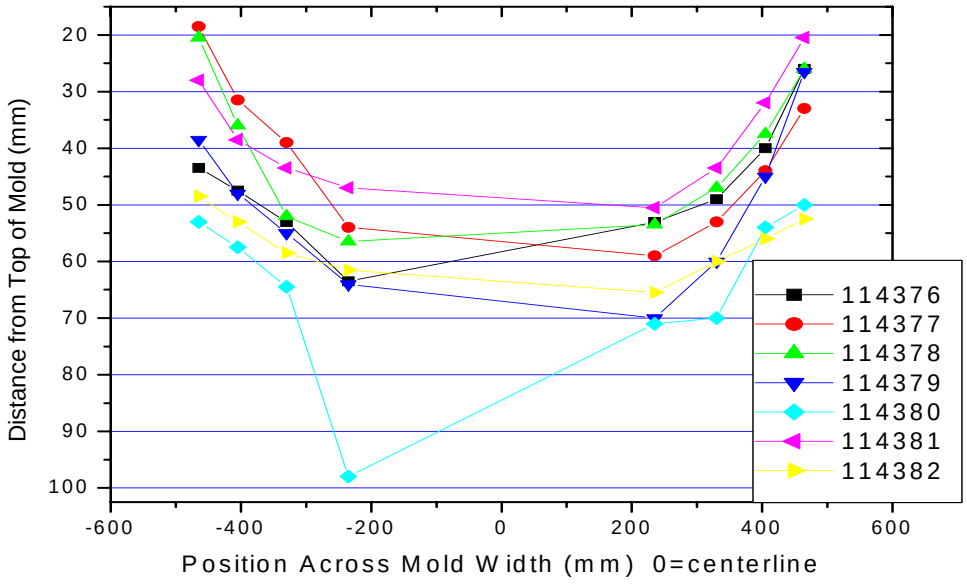

Figure 6.9: Meniscus Shape Profile Across Mold Width. Casting speeds range between 4.4 and 5.1 m/min and widths range between 1150 and 1300 mm.

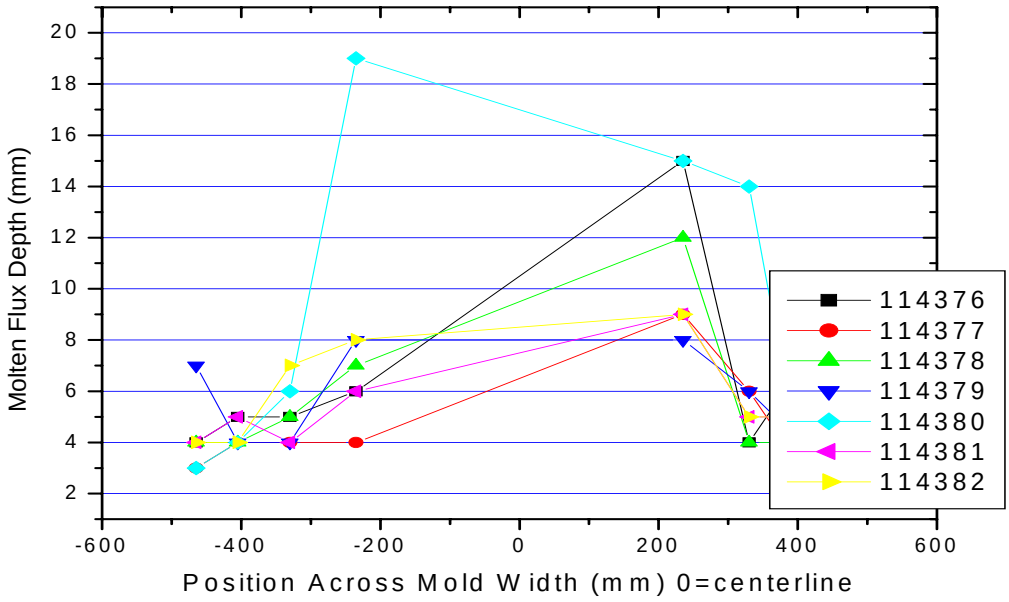

Figure 6.10: Flux Depth Profiles Across Mold Width for Same Heats as in Figure 6.9.

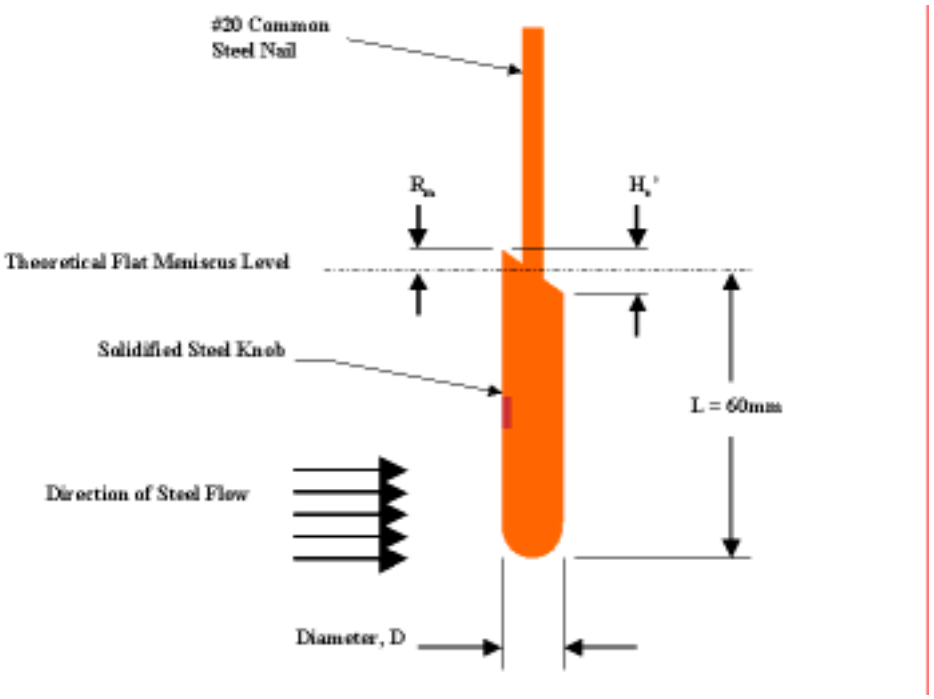

Figure 6.11: Diagram of Nailboard Measurements Used for Calculating Meniscus Surface Velocity.

6.2.3 Case 2 Data - Flow Direction

Following the success of the case 1 data in showing nailboards to be effective measurement tools, nailboards were again employed in making meniscus and flux measurements. From the outset of the follow-up trial, it was noticed that the direction of steel flow could be ascertained by evaluating the angle by which the highest point of the steel knob was rotated from the centerline of the mold (figure 6.11). For flow coming directly towards the SEN from the narrow face, the knob highpoint lies along the centerline. However, it was noticed that the highpoint was sometimes in a location rotated up to 45 degrees either clockwise or counterclockwise from the center line. Such an observation is corroborated by the results predicted by numerical and physical models [18]. It indicates that flow does not have 4-fold symmetry, due to both transients, geometry, and misalignment. Further results on flow direction are discussed in 6.3.

6.2.4 Case 3 Data - Nail Knob Diameter

During the gathering of case 2 data it was noticed that the diameters of the knobs varied with location in the mold from measurement to measurement, as did the angle of the flow. The diameters of the case 3 knobs appear to be independent of superheat as the knobs toward the center of the mold are not significantly different than the knobs near the narrow faces, where superheat is expected to be lower [18]. A literature search for a method to relate these geometric characteristics to velocity was conducted. The results described in 6.4, while not numerous, show that the nailboard method velocities are similar to previous calculations and measurements [18,42].

6.2.5 Case 4 Data - Interface Velocity

Following the successful trial, which yielded case 2 and case 3 results, another plant trial was conducted to use nailboard data to predict meniscus velocity using fluid dynamic fundamentals. To do this, nail and knob diameters were measured for every nail in addition to the same measurements done for cases 1, 2 and 3. This data is needed to calculate meniscus surface velocity.

6.3 Flow Direction as Indicated by Nailboard data

As mentioned previously, during the gathering of case 2 data it was noticed that the location of the highpoint of the steel knob following immersion indicated the direction from which the steel was flowing. Most of the time, no rotation was observed meaning that there was no velocity component in the through-thickness direction. Rotations were measured to be from about 5 degrees to 60 degrees with the flow always coming from the direction of the narrow face towards the SEN. This behavior has been predicted by several numerical models [18]. Several factors may affect this behavior. They include SEN alignment, flow oscillation at the SEN exit, flow within the mold and the cavity of the solidifying strand, and mold geometry effects. This observed rotation may affect the velocity values themselves. Since only a few instances of this rotation were noted and measured, it is not yet possible to conclusively determine whether this is so. Preliminary results show that large flow rotations above 45 degrees correlate slightly with a lower standing wave relative to heats cast at similar speeds with no observed flow rotation (Figure 6.12). This suggests that perfectly aligned jet impingement upon the narrow face produces a higher standing wave, which is logical. Further study is needed to determine if this is really the case.

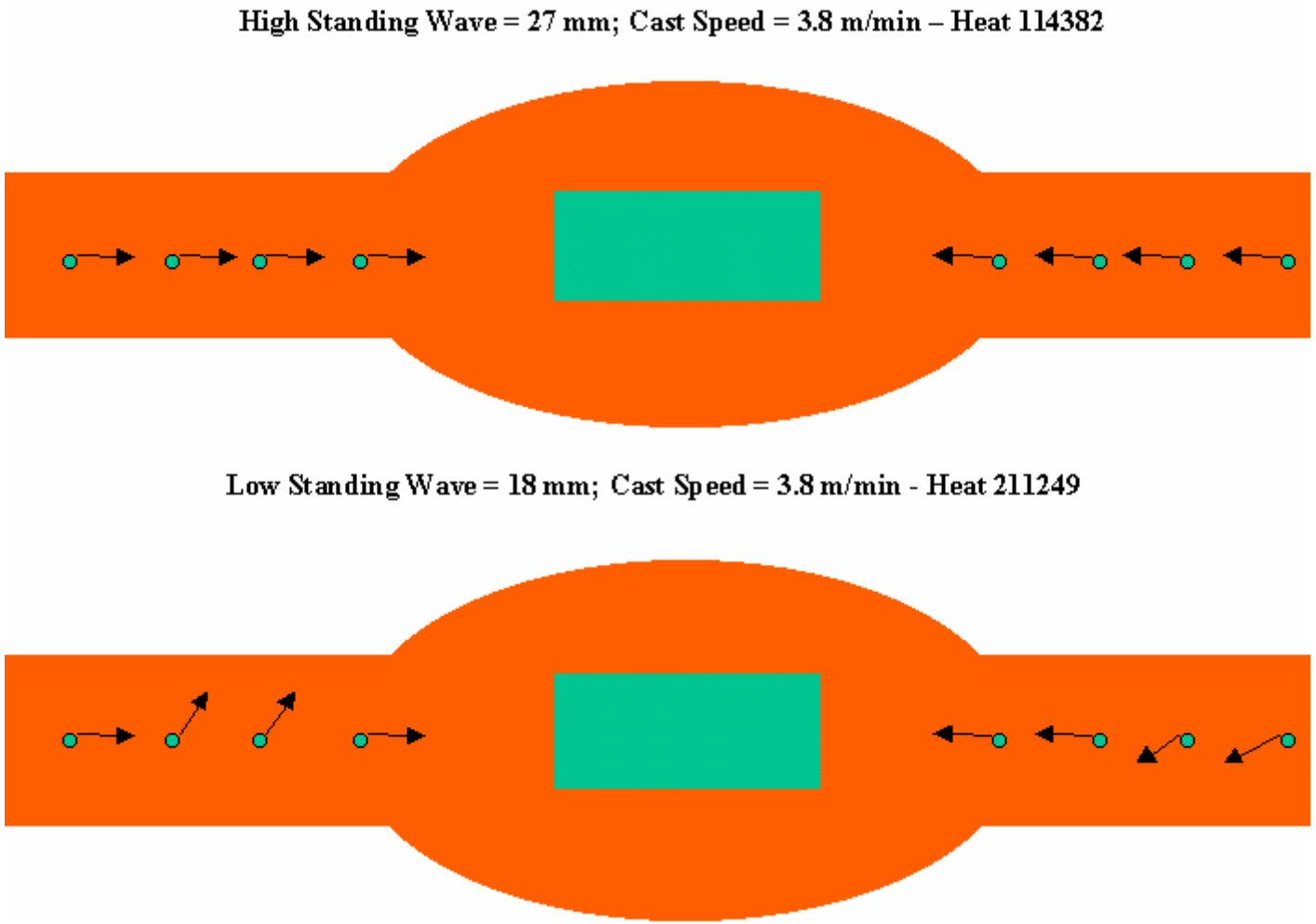

Figure 6.12: Schematic of Flow Direction as Determined from Nailboards for High and Low Standing Wave.

6.4 Explanation of Morison Equation and Description of Calculation Method

A method developed by Morison for round cylinders immersed in water was extended and applied to correlate steel knob shape with meniscus velocity. Morsion's original work calculated the force of water flowing past immersed piles. Since it was not known at the beginning of this trial that the knob diameters were important to surface velocity, only limited meniscus velocity results were obtained from heats cast near the conclusion of the trial (Case 4 data). The values that were measured for the meniscus velocity calculation are as follows (see also figure 6.11):

- High and low points of steel knob
- Unrefracted wave height, H_o'
- Diameter, D, of steel knob following immersion
- Depth, L, of nail immersion below flat level (0.060 m)

Constants that must be used are listed below:

- Ratio, k, of wave crest elevation above still liquid level to the wave height (0.78)
- Euler's Constant, γ (0.5772)
- Steel Density, ρ (7800 kg/m^3)
- Inertia Coefficient, C_m (1+k)
- Acceleration due to gravity, g (9.8 m/s^2)
- Fluid flow constant, δ ($3\pi/8$)

6.4.1 Suitability of the Morison Equation for Small Cylinders

Since the Morison equation was originally used to calculate forces upon large pilings it was necessary to determine whether it was applicable for small cylinders like the nails. Following a literature search it was deemed appropriate because of the geometry of the individual nails. Sarpkaya reports that a diameter to length ratio above 0.2 is required because the equation takes into consideration the effects of wave diffraction. That ratio for a nail with no knob is 0.05, but for a nail with a steel knob, it ranged from 0.2 to approximately 0.3 so the equation was assumed applicable [55].

6.4.2 Calculation of Meniscus Stream Velocity Using Fluid Dynamics/Morison Equation

After obtaining all of the above values and calculating an initial wave height (H_o), the maximum force of steel against the nail/knob can be calculated. Up to this point, Morison's equation is followed exactly. Velocity was then calculated using the relationship between force and velocity for vertically oriented circular cylinders immersed in a flowing fluid.

The first step in the calculation of meniscus surface velocity values is to establish a run-up height for the steel as it flows past a submerged nail. For this case, the run-up height is assumed to be half of the unrefracted wave height, H_o', which is defined as the distance between the high point and low point on each steel knob. Recall that the angle at the top of the steel knob and the diameter of the knob are indicators of flow direction and velocity. Equation 6.2 predicts the wave run-up height from the total wave height (H_o). Equation 6.3 is used to calculate hypothetical wave run-up values (R_m).

$$H_o = H'_o * k \quad (6.2)$$

$$R_m = H_o * 0.5\{1 + k^2[\ln(k/2) + (2\gamma + 3]\}^{0.5} \quad (6.3)$$

which simplifies to

$$R_m = 0.507\ H_o' \quad (6.4)$$

The variables are defined in the nomenclature. Wiegel and Beebe have observed that the ratio, k, of the initial wave height (H_o) to the unrefracted wave height (H'_o) for an immersed cylinder is 0.78 [56]. Accordingly, the run-up height, R_m, corresponds to about half of the measured unrefracted wave height, H_o', agreeing with Sorenson [56].

Next, the maximum force of flowing steel acting upon the steel knob on the nail is calculated. The equation is derived from the Morison equation for an unrefracted wave and is:

$$F = \pi^2 \rho H_o L D^2 / 8t^2 * C_m * k \quad (6.5)$$

The value, t, is an empirical maximum frequency wave period and is assumed to be 0.030 seconds, which corresponds to the maximum frequency detectable in this study. With force calculated, it was necessary to calculate velocities associated with it. To obtain a horizontal velocity the following equation is used [57]:

$$U = (F / L * 2 / (\rho C D))^{0.5} \quad (6.6)$$

C is the force coefficient corresponding to the total in-line force and has a value of six for the conditions in this study [57]. While the root mean square velocity may underestimate the actual maximum velocity, it does take into consideration flow oscillation and flow ellipticity, which is common with flow about a vertically-oriented circular cylinder [57].

6.5 Evaluation of the Calculated Meniscus Stream Velocity Values

The calculated meniscus stream velocities values are compared against values obtained and/or calculated through mathematical and physical water modeling and through the other velocity measurement methods discussed previously. As shown in table 6.4, the values obtained using the method just described are 30% to 100% greater than velocities predicted by two mathematical models [18, 42]. However, the casting conditions are very different, as is mold geometry.

6.5.1 Comparison with Mathematical Model Predictions

The two mathematical models from which velocity data were obtained for comparison were from a rectangular mold and a CSP mold, done by McDavid and Thomas [18] and Nam et al [42], respectively. Table 6.3 and Figures 6.14a and 6.14b show calculated velocity across the width of the mold. As can be seen from Figure 6.13, the predicted velocity profiles have similar shape, but appreciably lower values than do the velocity profiles generated during the course of this project. The discrepancy might also be due to the shape and magnitude of the standing wave, or level fluctuations or fluctuations in the standing wave, which were not modeled. The design of the SEN and casting conditions such as casting speed and mold geometry in the mathematical models differ substantially from operating conditions in this project, which included casting with both 2-port and 4-port SEN designs. Moreover, since there are only four locations per side where nailboard data is obtained, the scarcity of data is very much a factor in limiting the construction of a velocity profile.

In addition to these, numerous other factors may affect the velocity at the meniscus. Some of these include:

- SEN alignment and funnel geometry effects

- Integrity of flow control through the SEN (e.g. biased flow)
- SEN exit stream oscillation
- Stopper Rod Irregularities

Table 6.3: Meniscus Surface Velocity Values as Calculated for 14 Heats of the Current Project. All values are given in units of meters/sec.

	Distance From Centerline of the Mold (mm)							
Heat #	**-465**	**-405**	**-330**	**-235**	**235**	**330**	**405**	**465**
213760	0.146	0.151	0.186	0.186	0.166	0.242	0.229	0.208
117004	0.210	0.144	0.162	0.195	0.219	0.232	0.216	0.172
117005	0.248	0.189	0.124	0.137	0.168	0.283	0.270	0.156
117006	0.271	0.224	0.203	0.145	0.095	0.225	0.277	0.221
213763	0.221	0.276	0.195	0.147	0.170	0.238	0.213	0.263
117021	0.220	0.185	0.215	0.226	0.246	0.257	0.300	0.254
117022	0.190	0.257	0.196	0.170	0.184	0.240	0.261	0.240
117023	0.177	0.160	0.257	0.178	0.278	0.250	0.251	0.184
117024	0.292	0.270	0.251	0.156	0.290	0.145	0.175	0.161
117025	0.139	0.136	0.211	0.165	0.209	0.172	0.164	0.173
117026	0.218	0.158	0.194	0.194	0.148	0.233	0.252	0.176
213782	0.282	0.227	0.183	0.222	0.183	0.221	0.205	0.249
213783	0.000	0.145	0.273	0.182	0.179	0.251	0.149	0.169
213784	0.225	0.143	0.203	0.209	0.201	0.196	0.173	0.156

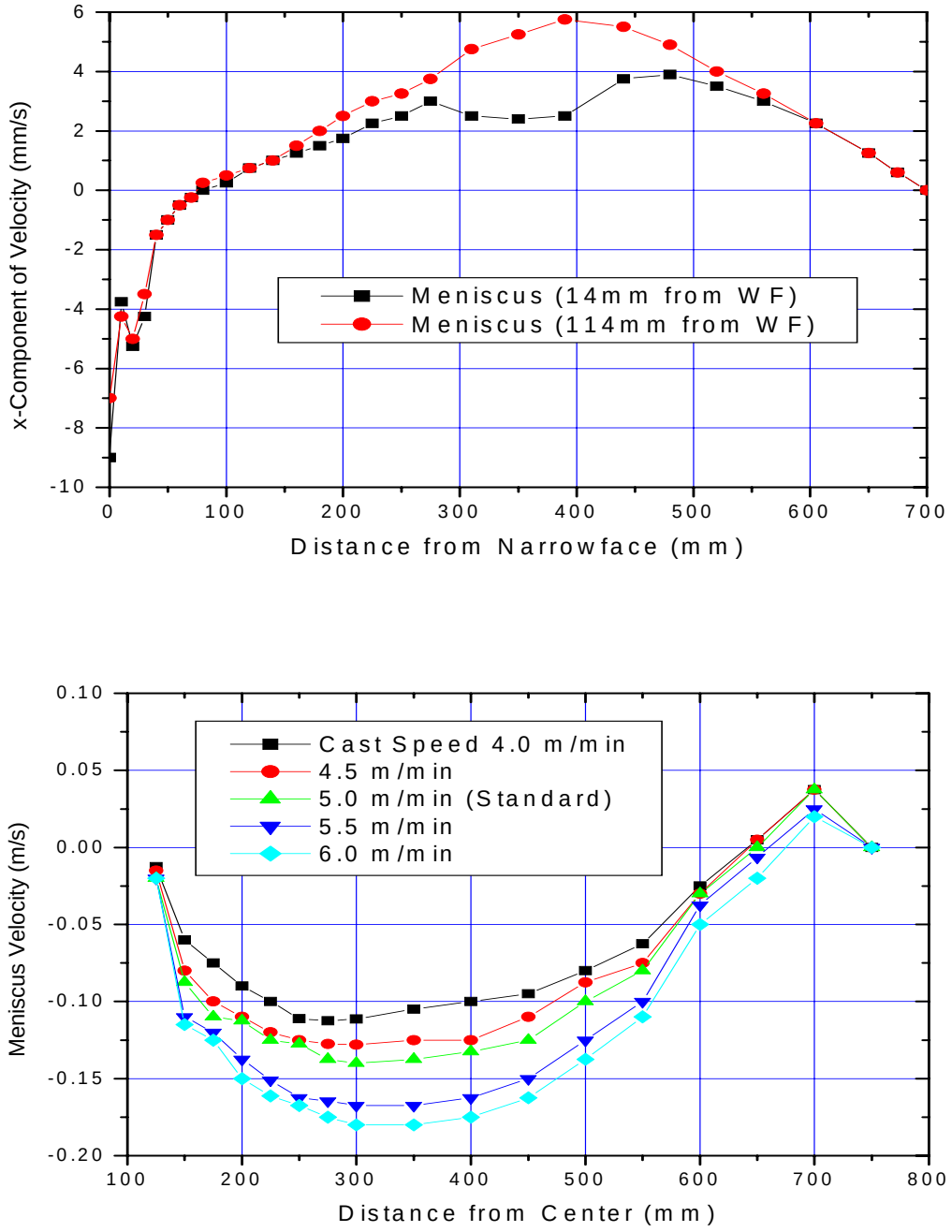

Figure 6.13: Top - Meniscus Surface Velocity vs. Position in Mold [18]. Bottom - Meniscus Surface Velocity Values at Several Casting Speeds vs. Position in Mold [42].

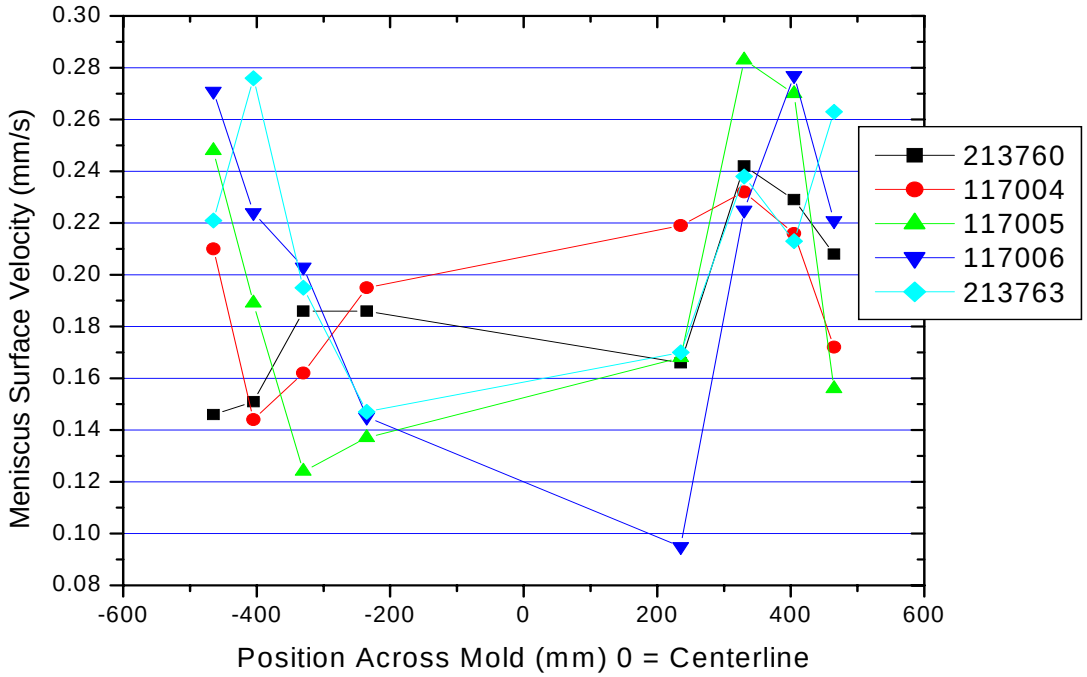

Figure 6.14a: Calculated Meniscus Surface Velocity vs. Position in Mold for Heats in this Study Cast with a 2-Port SEN. Note: Zero represents the mold centerline and the values furthest from the center are not at the narrow face, but 85 mm in from the narrow face.

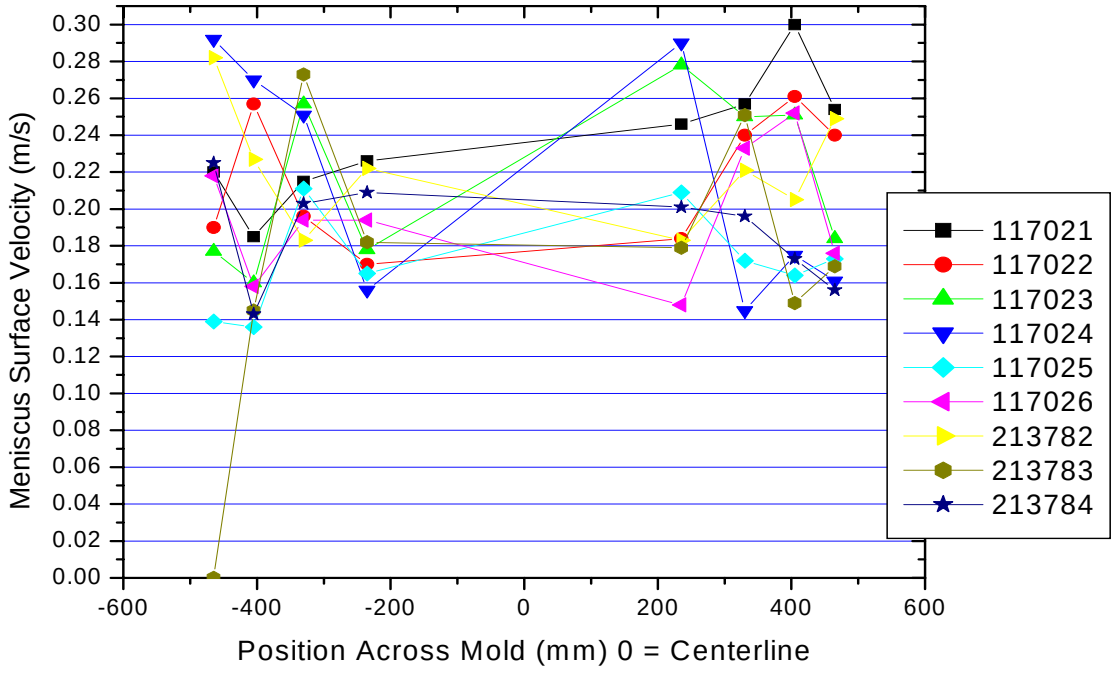

Figure 6.14b: Calculated Meniscus Surface Velocity vs. Position in Mold for Heats in this Study Cast with a 4-Port SEN.

6.5.2 Comparison with Water Model Predictions

The calculated velocity values were also compared to water model velocity measurements. In the water models, meniscus velocity was measured by either PIV or by the movement of dye released into the system. Table 6.4 shows typical values for meniscus surface velocity in several numerical and physical models. As was the case with mathematical models, transient effects such as SEN misalignment or erosion are not considered in the water models. Also, the water models cannot predict accurately the interfacial behavior of molten steel and slag in CSP casting. This is evident from the observations that the measured standing waves and wave oscillations are much smaller in steel than in the water models. This problem concerning suitable slag substitutes to be used in water modeling is appreciable. Most "slags" consist either of an oil or some polymeric material, but nothing thus far has come close to exhibiting the same relationship to water that real slag does to molten steel. The problem is very complex and is out of the scope of the current phase of the project, but will most certainly be considered in any subsequent work.

Table 6.4: Comparison of Maximum Meniscus Velocity Values between Several Models and Present Work.

Author	Study Type	Max. Meniscus Velocity (m/s)	Section Size And Cast Speed	SEN Port Angle
McDavid, Thomas [18]	**Conventional CC Numerical Model**	0.17	229 x 1397mm 1 m/min	25° down
Nam et al [42]	**CSP Numerical Model**	0.17	50 x 1500mm 4.0-6.0 m/min	70° down
Kubota et al [9]	**Conventional CC 1/3 Scale Water Model**	0.37	76 x 500mm 1.84 m/min	25° down
Present Work	**Nailboard Measurements**	0.30	50 x 1295 5.1 m/min	30° down

6.5.3 Surface Velocity Measurement Trends

The most important comparisons for meniscus surface velocity values were done by analyzing the dependence of surface velocity upon casting speed and volume flow rate, location in the mold, standing wave height, and the oscillation of the standing wave. No

previous information could be obtained for CSP casting so the comparisons are with conventional slabs.

For many cases in this analysis, it was found that the calculated meniscus surface velocities showed no correlation with changes in casting variables such as volume flow rate and casting speed. Maximum, minimum, and average velocity values appear to be unaffected by changes in these variables. This may be due to these maxima, minima, and averages being based on very local measurements (each individual nail in a set location) and then compared to a global value like volume flow rate and casting speed. It was found, however, that volume flow rate and casting speed affect the *difference* between the maximum and minimum meniscus surface velocities for an individual nailboard measurement (two of four values per nailboard). This difference is simply the maximum (usually near the narrow face) minus the minimum (typically near the SEN) velocity for each nailboard. See Figure 6.12 for nail arrangements. It is believed that this difference to some extent describes the level of turbulence near the meniscus - for instance, as the casting speed increases so does the difference between maximum and minimum meniscus velocities and therefore turbulence is greater. Figures 6.15 and 6.16 show the relationship of meniscus surface velocity difference with steel volume flow rate and casting speed. The trend in Figure 6.15 shows that volume flow rate has little effect upon the meniscus velocity difference, but this is understandable as flow rate takes into consideration mold width. Figure 6.16 shows that an increase in casting speed causes the meniscus surface velocity difference to increase somewhat. This trend is similar to what would be expected, although with much scatter in the results. This scatter in the data may be due to the nailboard method only being in its infancy with regard to meniscus velocity measurement. For example, an increase of approximately 25% in casting speed can result in anywhere from a 30% to 50% increase in the meniscus surface velocity gradient. This large scatter might be due to the many other changing factors that affect flow at the meniscus. Two significant effects are known to be mold width and SEN submergence [5,6]. Figure 6.17 illustrates that there appears to be a decrease of 30 to 50 percent in meniscus surface velocity difference with a 120 mm increase in width.

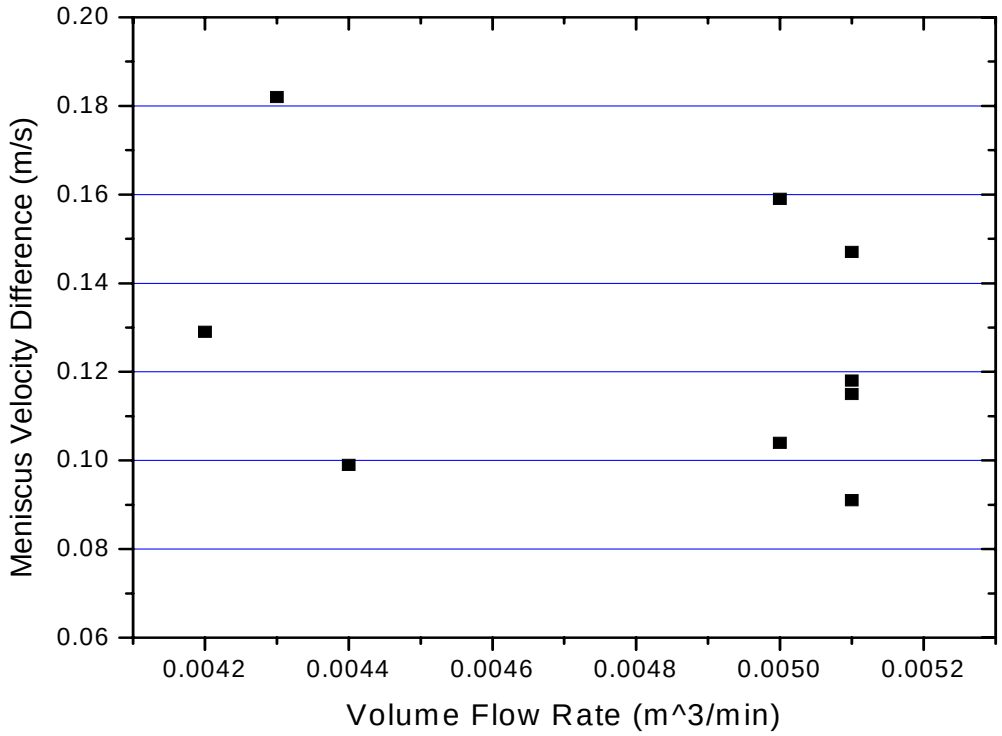

Figure 6.15: Dependence of Meniscus Surface Velocity upon Volume Flow Rate.

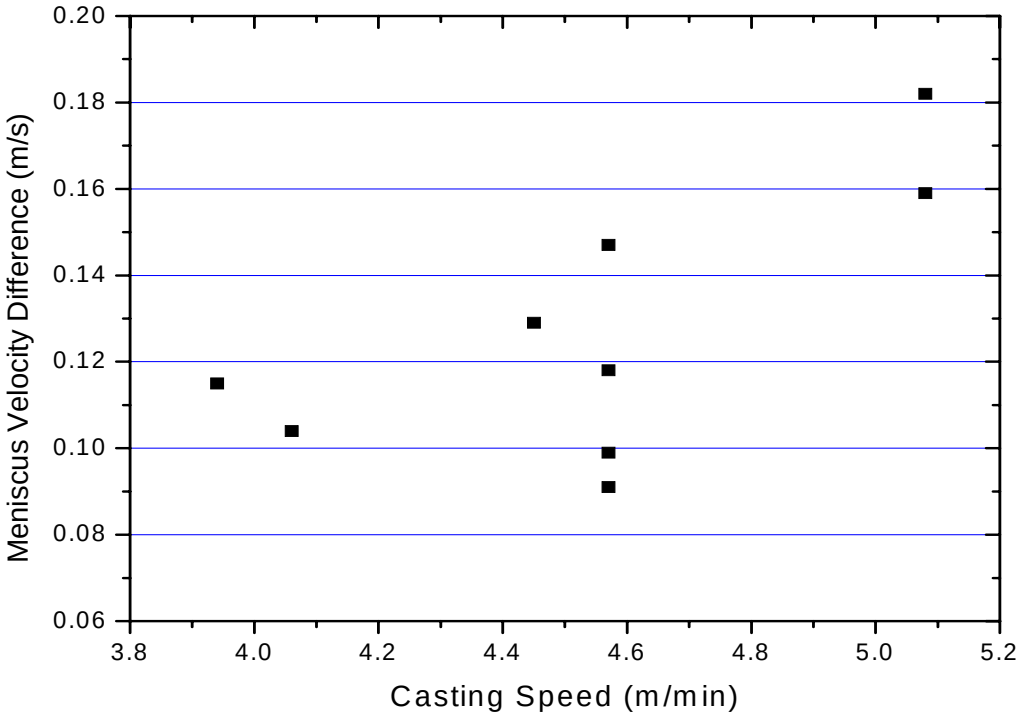

Figure 6.16: Dependence of Meniscus Surface Velocity upon Casting Speed.

This makes good sense because as the mold width increases, there is more space for the steel flowing from the SEN to lose more of its momentum as it flows, resulting in lower velocities at the surface. Interestingly, increased SEN submergence depth appears to increase the meniscus surface velocity (and the difference) (Figure 6.18), which might be due to the small (29 mm) range of SEN submergence values. While this at first appears misleading, Honeyands et al have shown that maximum wave height increases in water models when SEN submergence exceeds approximately 225 mm [5]. On the other hand, Figure 6.19 shows that SEN submergence has no effect upon standing wave height. A more important relationship is presented in Figure 6.20. This figure shows a moderate correlation between standing wave height and meniscus surface velocity difference. This certainly makes sense and is another indication that the meniscus surface velocity values calculated from nailboard data reflect meniscus behavior.

An interesting observation regarding the diameter of the steel knobs that form on the nails during immersion in the mold is that the knob diameter decreases with increasing casting speed (Figure 6.21) yet increases with increasing meniscus surface velocity (Figure 6.22). The limited amount of data available at this point make it difficult to come to any conclusions, but it is believed that with a large body of meniscus velocity data the nail/steel knob diameter will decrease with increasing meniscus surface velocity and that there also may be an effect of superheat.

6.6 Meniscus Surface Velocity Relationship with Standing Wave Fluctuation and Oscillation

Meniscus surface velocity and the fluctuation of the standing wave (or the long-period wave) were determined by Kubota et al to be related linearly [9]. A similar trend was observed in the course of this project, although with lower surface velocities. Figure 6.23 shows a very rough correlation with scatter, but with velocities varying only from 0.25 m/s to 0.30 m/s. It is believed that the differences are due to Kubota's results being based on 1/3-scale water model results and different mold geometry. To further investigate this phenomenon, the period of the standing wave fluctuation was plotted versus the value of SEN submergence divided by casting speed. Honeyands and Herbertson have shown a linear relationship between the two in continuous slab casting [6]. Figure 6.24 shows similar results obtained

during this project. The value of SEN submergence divided by casting speed can be thought of as the average residence time in the upper recirculation region of the mold. The solid diamonds in Figure 6.24 represent standing wave oscillation periods as predicted by the Honeyands/Herbertson water model and the open squares represent the actual standing wave oscillation period as obtained through metal level fluctuation data and FFT analysis. The error in the measured data is believed to originate with the variations in casting speed and SEN submergence during operation.

6.7 Defects

For the June-July, 2000 trials, typical coil rejections were approximately 20%, mostly for mold flux-related defects. Following a grade change from a boron-containing grade to one without boron, a rejection rate of 0.5% was achieved thereafter and in the subsequent trials in February and June, 2001. Finally, with the trial of the 4-port SEN, a rejection rate of zero was achieved, albeit only with 54 coils (Table 5.5). The mold flux - related defects were typical in appearance as described in the literature and contained trace amounts of sodium and potassium, which are present only in mold fluxes (Figure 6.25)[13-14, 16].

Mold flux-related defects were found to occur with greatest frequency when boron-containing grades were being produced. Prior to this project, internal rejection rates for mold flux slivers were as high as 20-30%. Upon analysis of mold slags from both boron-containing steels and steels without boron, it was found that the slags from boron-steels picked up about 50% more alumina and anywhere from 20-100% more zirconia than slags from regular carbon steels. The importance of boron and boron oxide has been discussed previously in the literature review. One of the coils from a boron grade was found to have 41 mold flux sliver defects while coils of carbon steel of the same gauge with mold flux slivers had only between one and five individual defects [58].

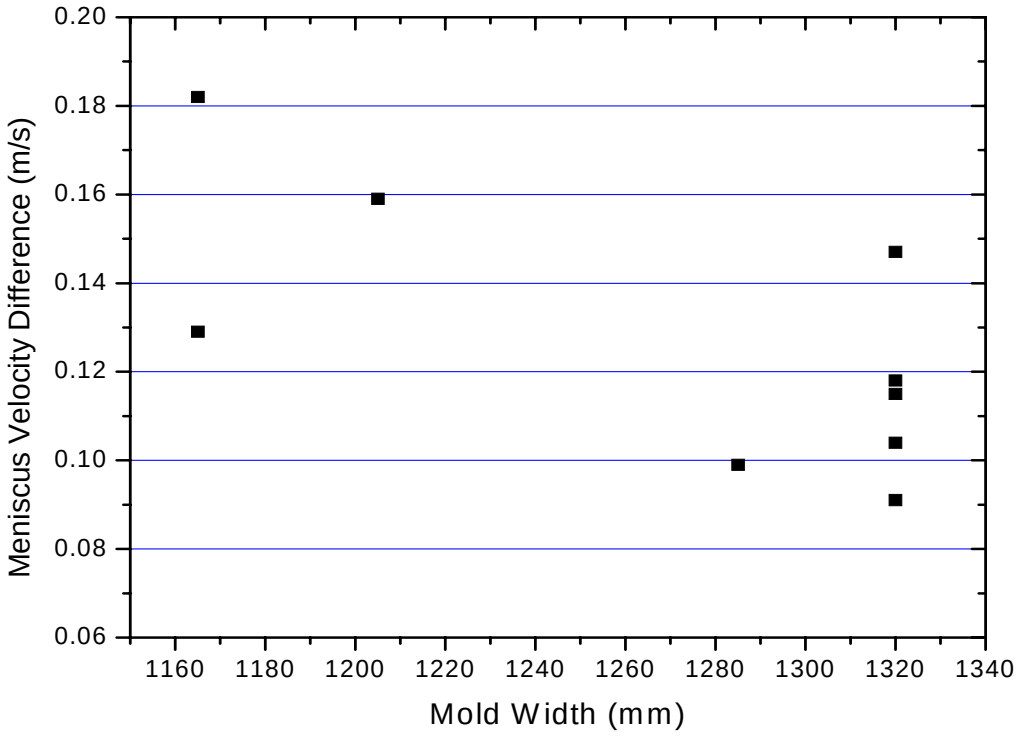

Figure 6.17: Dependence of Meniscus Surface Velocity upon Mold Width.

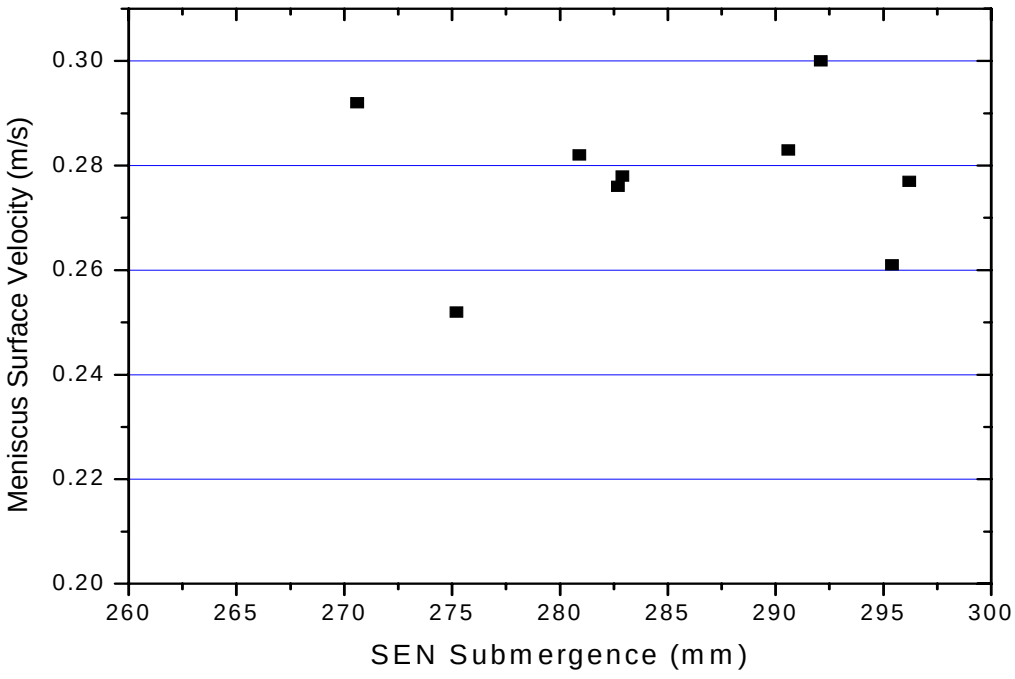

Figure 6.18: Dependence of Meniscus Surface Velocity upon SEN Submergence.

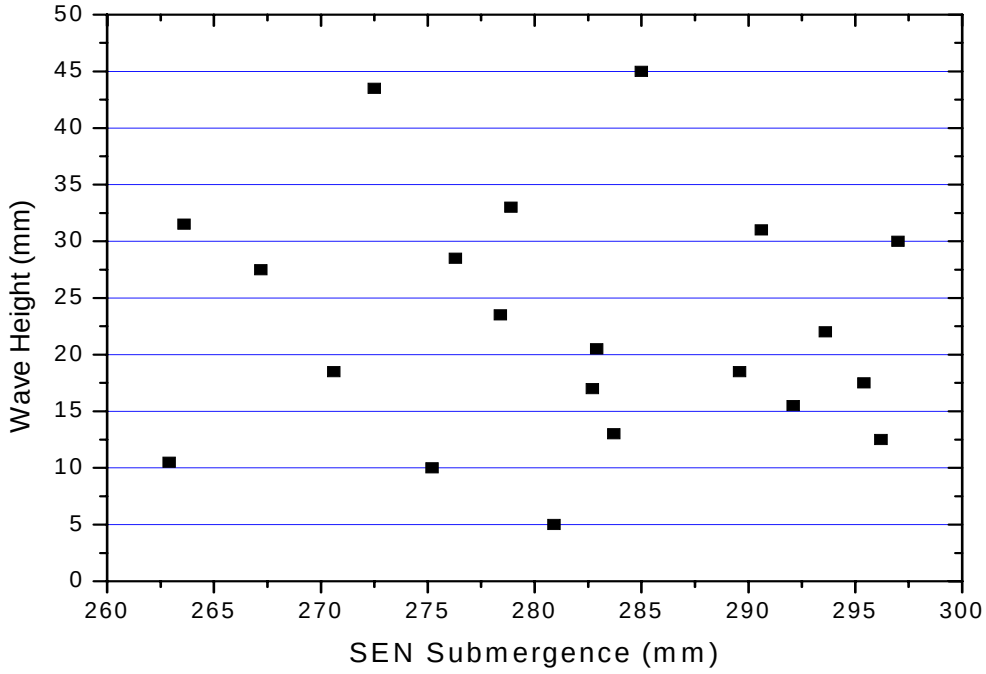

Figure 6.19: Relationship between SEN Submergence and Standing Wave Height.

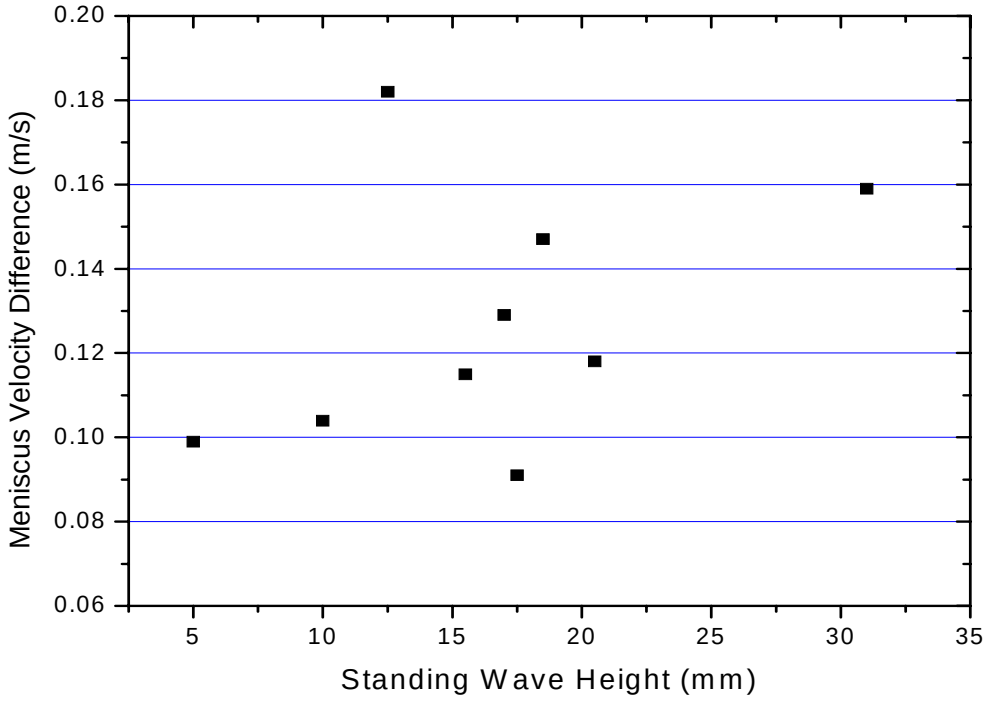

Figure 6.20: Relationship of Meniscus Surface Velocity to Standing Wave Height.

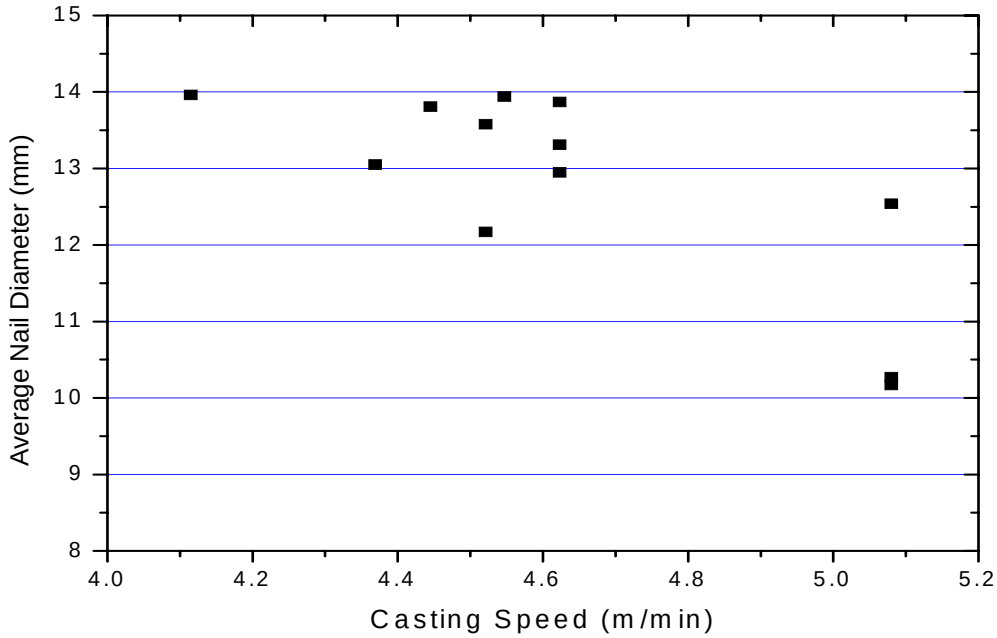

Figure 6.21: Nail Diameter vs. Casting Speed.

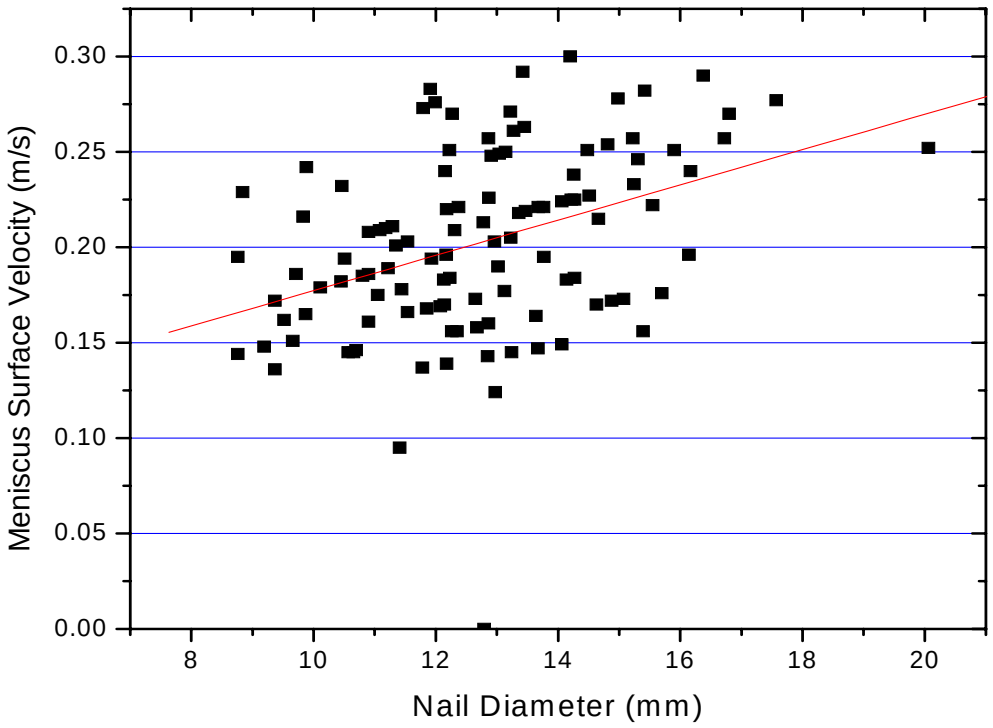

Figure 6.22: Meniscus Surface Velocity vs. Nail Diameter.

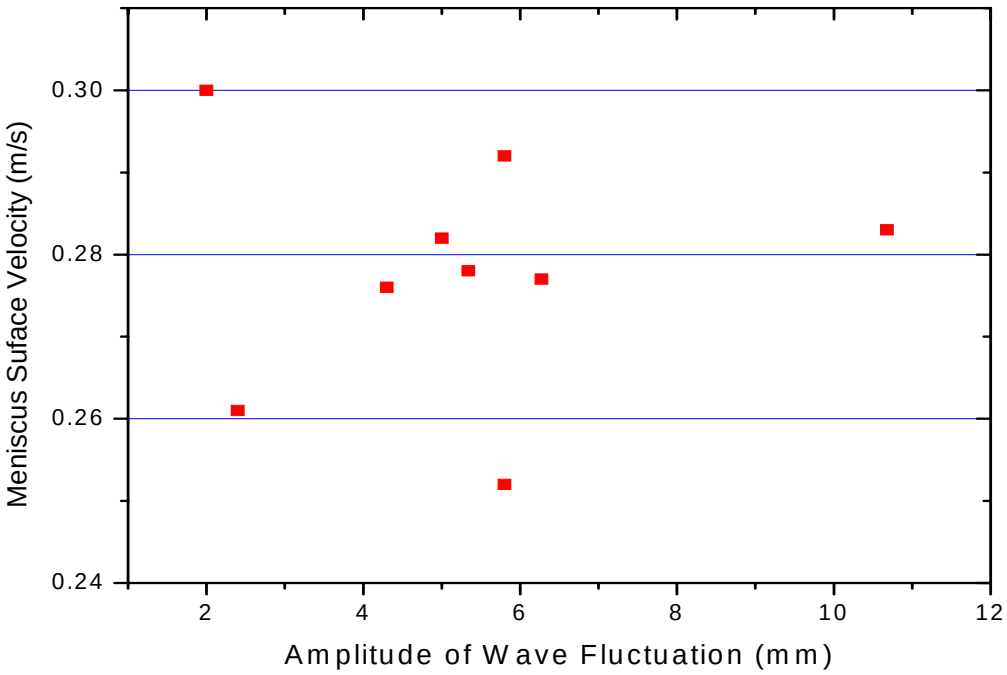

Figure 6.23: Relationship between Surface Stream Velocity and Standing Wave Oscillation Amplitude for this study.

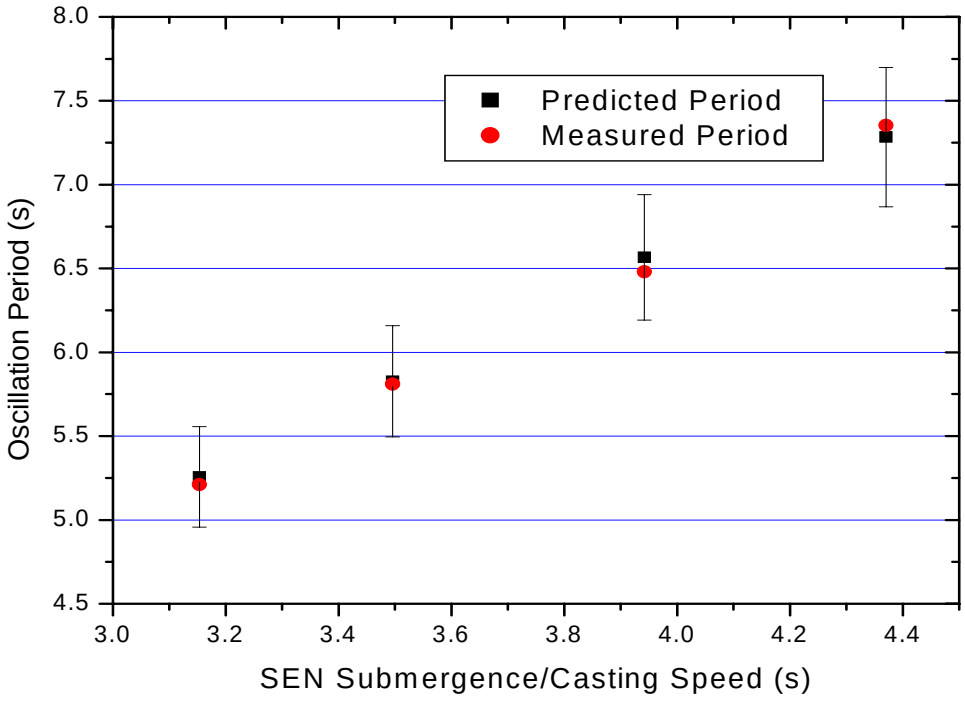

Figure 6.24: Standing Wave Oscillation Period vs. Average Residence Time in Upper Recirculation Zone for the Current Study [Predicted Period Adapted from Reference 6, Figure 3].

Mold flux sliver defects were observed to occur at seemingly random locations across the width of the strip. Also appearing to be somewhat random were the estimated depths of the defects. The depth of a defect could not always be estimated, however, as some amount of delaminated steel that comes away from the rest of the coil is necessary to make such estimations. Some defects appeared with no delaminated steel and the mold flux/slag residue was visible along the entire length of the defect. Most slivers did exhibit some degree of delamination and the thickness of this delaminated steel is believed to be proportional to the depth at which the defect was deposited into the solidifying shell during casting. For example, a defect with a delaminated steel thickness of 0.10 mm on a 0.50 mm coil is estimated to have been deposited in the shell at a distance of 10 mm from the surface (assuming a 100x reduction from a 50 mm thick slab).

Once the grade change was made and no boron was present in the steel, mold flux sliver internal rejections average about 0.5%, but this was deemed too high. Further inspection of mold flux slivers yielded some interesting results. For example, one defect had a delaminated steel thickness of 0.06 mm. Since the slab was 50 mm thick and the finished coil 0.50 mm thick (a 100x reduction), the defect was estimated to have been entrained at a depth of 6 mm in from the slab surface (Figure 6.25).

Using the equation:

$$x = kt^{1/2} \quad (6.7) \ [4]$$

where k is a caster constant (26 mm / $min^{1/2}$) and t is the time in minutes, the depth in the mold where the defect was deposited was calculated. The variable, x, is the depth of the defect in millimeters. For a 6 mm defect depth, a time of 3.19 seconds is obtained and knowing the casting speed to have been 5.08 m/min, it can be deduced the defect was entrained in the steel shell at a distance of about 270 mm from the meniscus. In addition, it was also observed that this defect occurred near the edge of the sheet. These factors indicate that the mold flux slag was entrained by being drawn away from the meniscus steel/flux interface then carried by the steel flow in the upper recirculation zone into the SEN exit stream. This strong SEN exit flow then probably caused the entrained flux to be deposited where it was, only to be exposed during rolling.

It is thought that the lack of observed mold flux defects on the steel produced using the four-port SEN was due to the flow patterns in the mold. While details of the SEN are

proprietary and not available for discussion, it is believed that the upper ports provide just enough meniscus and upper recirculation flow to prevent meniscus freezing and the lower ports provide for most of the steel delivery. Such a design in all likelihood leads to the upper recirculation zone being smaller in the four-port case than with two-port SEN casting. This results in lower overall meniscus surface velocity values while casting with a four-port SEN. Figures 6.26 and 6.27 illustrate this with respect to volume flow rate. It must be noted, however, that very little data was available for the four-port SEN at the time the trial was undertaken.

At the time of the submission of this thesis, use of the four-port SEN has commenced for all casting done at Nucor-Crawfordsville as it has shown a marked improvement with regard to the occurrence of mold flux slivers and other defects known to originate at the meniscus. Unfortunately, inspection data are not available at this time.

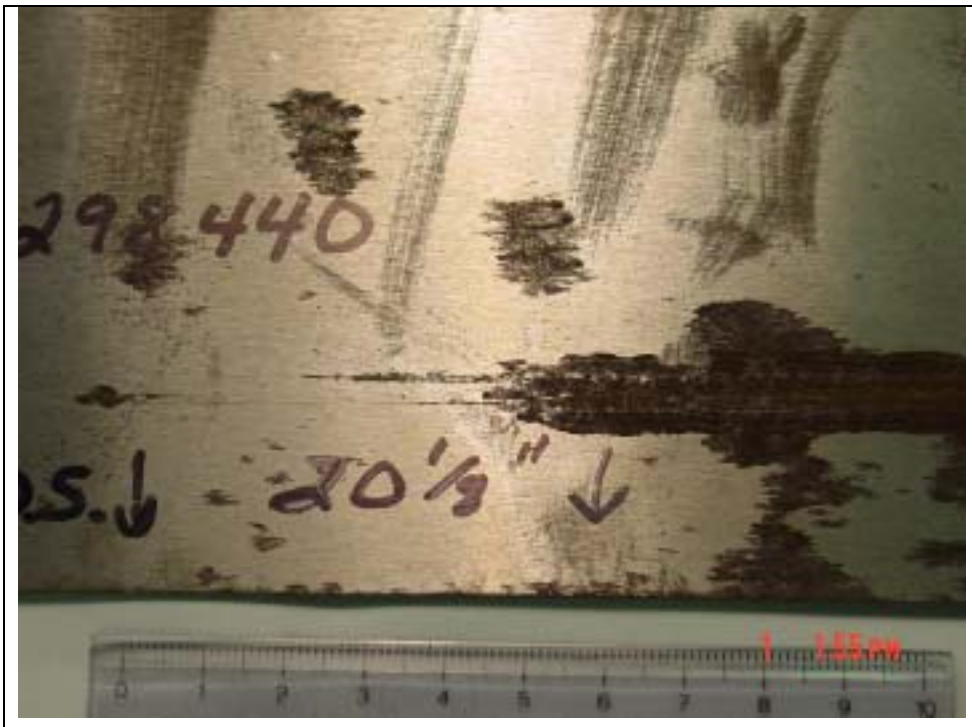

Sliver Defects

Figure 6.25: Typical Mold Flux Sliver Defect on CR Strip. Defect is Elongated Horizontally.

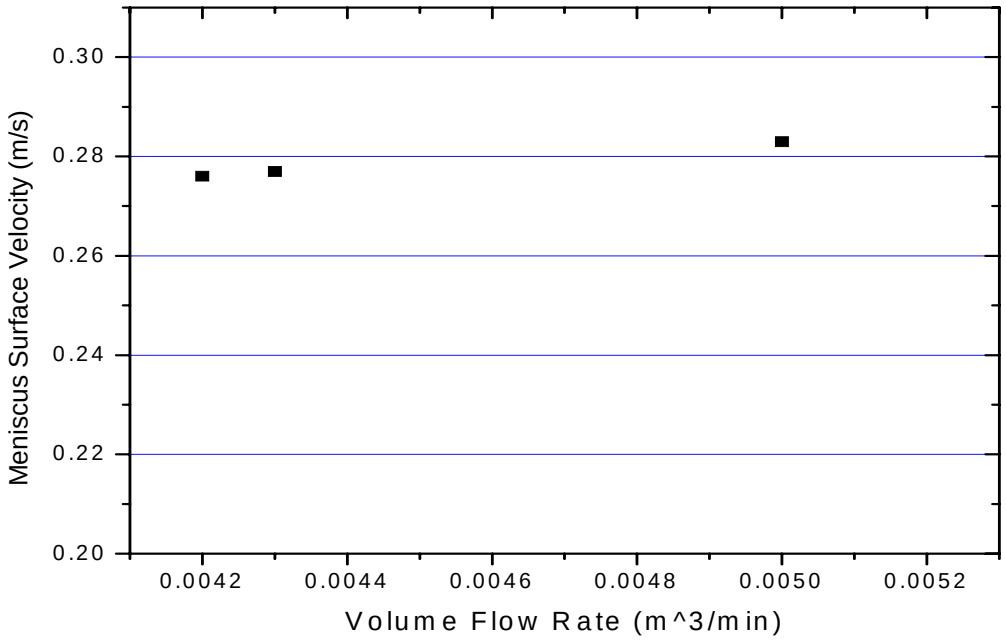

Figure 6.26: Meniscus Surface Velocity vs. Volume Flow Rate for a Standard Bifurcated SEN.

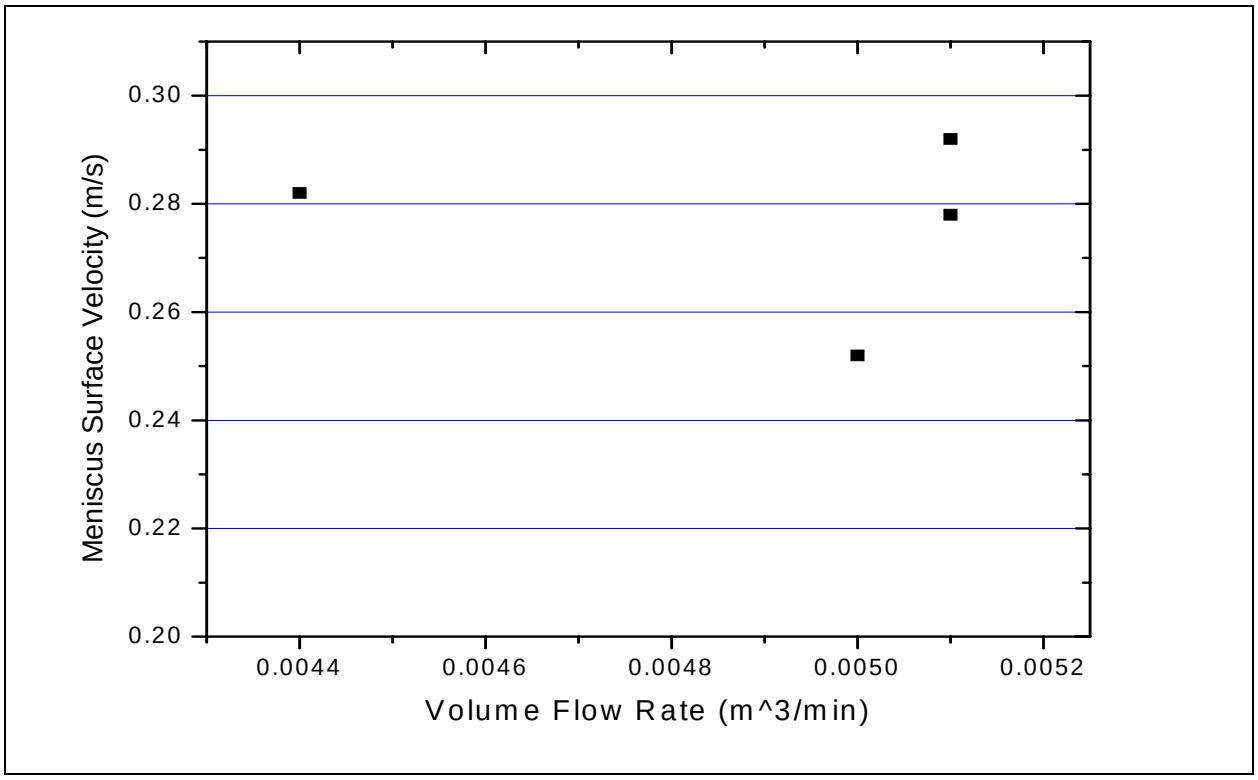

Figure 6.27: Meniscus Surface Velocity vs. Volume Flow Rate for a Trial Four-Port SEN.

Chapter 7: Conclusions and Recommendations

Three extensive industrial plant trials were performed. It is believed that these trials are the first of their kind to be performed on an operating CSP caster. These trials consisted of extensive mold meniscus and flux measurements using nailboards. In addition to the mold and meniscus nailboard measurements, pertinent casting data was collected by way of low and high frequency data acquisition systems. The low frequency data (level two) consisted mainly of strand and mold dimensions and information essential for calculating heat transfer. The high frequency (PDA) data was used to perform Fast Fourier Transform (FFT) analyses. Upon examination of the low frequency data, it was evident that nothing out of the ordinary had occurred (stickers, erratic heat transfer, etc.). FFT analysis of the high frequency data shows clearly that there are many factors, from mechanical transients to various fluid flow phenomena, that have an effect upon mold metal level and the surface quality of the final product.

From the FFT results, it was found that casting speed appears to have the largest effect increasing the magnitude and frequency of meniscus level oscillations. Width was also found to have an effect. Casting speed and width, however, are related by the mass or volume flow rate of steel. When the flow rate is increased, the frequency and magnitude of meniscus level fluctuations increase as predicted by the models. However, while the frequencies match those established by the models of Honeyands and Herbertson, the magnitudes of the oscillations in the real casting system tend to be approximately an order of magnitude less than those found in the literature [5,6]. The largest effect of any transient, mechanical or flow related, is that of the slab shear cut. Metal level fluctuations of more than 6 mm were measured to occur almost every time a slab cut was made. The shear cuts only occur every 10-20 minutes, depending upon slab length, but the very large fluctuations associated with them have long been suspected of resulting in defects and breakouts. This possible relationship to defects and breakouts is difficult to confirm in the plant owing to the the difficulty of inspecting hot slabs as they move through the process.

Nailboard measurements yielded much data about meniscus and standing wave shape in CSP casting. Standing wave heights were found to average about 20-25 mm high and flux depths were observed to vary between 3 and 10 mm. It was also observed that the standing

wave is always higher near the narrow face and flux depths are greater nearer the SEN under ordinary casting conditions. When used in conjunction with oscillation mark measurement and FFT results that provide magnitudes of standing wave height and level fluctuations due to mechanical and flow-induced transients, a new consistent understanding of mold/meniscus behavior in thin-slab casting has emerged. These nailboard measurements are believed to be the first on a CSP process. However, they differ from previous research for reasons that are unclear and require further investigation. One interesting result of this use of the nailboard data in conjunction with FFT data is the similarity of flow and standing wave behavior when compared to the work of Honeyands and Herbertson – the oscillation of the standing wave with changes in the steel residence time in the upper recirculating region in this project match almost perfectly their results [6]. This is important because their work was carried out on water models, conventional slab casters, and rectangular mold thin-slab casters.

The most groundbreaking findings of this project stem from refinement of the nailboard method. These measurements have built on previous findings of meniscus/standing wave and flux depth behavior (from conventional casting studies) and have yielded data pertaining to the fluid flow behavior in the molten steel/flux interfacial region, including meniscus surface velocities. Flow direction as determined from nailboard inspection has been observed to possibly have an impact upon standing wave height. At flow rotations greater than 45 degrees, a slight decrease in standing wave has been detected when compared to other heats cast under similar conditions. The calculated meniscus velocity values appear to be consistent with the values found in the literature even though no experimental values for CSP casting with similar conditions to those in this project have been published to date. Typical average meniscus surface velocities determined in the study average about 0.25 m/s at a casting speed of approximately 5 m/min and a mold width of 1200 mm. This compares favorably with published velocity values even though the casting conditions in this study are not to be found in the literature. Dependence of meniscus surface velocity upon casting speed and volume flow rate is at present inconclusive with no apparent correlation. However, a trend showing that the difference between maximum and minimum meniscus velocities increases with casting speed was noted and may possibly be an indication of increased turbulence in the meniscus region. A similar trend was also observed with respect

to standing wave height, as would be expected since standing wave height is known to vary directly with casting speed and volume flow rate.

The observation that meniscus surface velocity decreases with increasing mold width suggests that flow velocity and the resultant turbulence and defects might be related to the geometry of the upper recirculation zone. This is somewhat supported by the results of the four-port SEN trial where no defects were observed. The calculated meniscus surface velocities were similar for both the two- and four-port SEN, but the construction of the SENs is very different, which certainly has a large impact upon the geometry of the upper recirculation zone.

This preliminary work will allow operators to perform this very simple and inexpensive test several times during a shift. Prior to any measurement of the steel knob on the ends of the nails, an operator will be able to get an approximate idea of the standing wave dimensions and any crossflow that might be occurring. If these visual observations are made frequently during a sequence, much may be learned about the evolution of steel flow due to SEN wear/erosion. From three simple measurements that can be made with calipers, a local meniscus velocity can be calculated, which can then be used in evaluating the likelihood of slag emulsification and defect generation.

REFERENCES

[1] J.K. Brimacombe and I.V. Samarasekera. "The Challenges of Thin Slab Casting." *Near-Net-Shape Casting in the Minimills Conference*, Vancouver, British Columbia, August 19-23, 1995, p.33-53.

[2] W. Hennig, F. Quix, and D. Schulz. "CSP Concepts/Strategies - Developments over the last 10 Years." *12th Seminario de Aceria of the Instituto Argentino de Siderurgia (IAS)*, Buenos Aires, November 2-5, 1999, p.439-448.

[3] E. Hoffken, P. Kappes, and H. Lax. "The Production of Continuously Cast Strip on the Pilot Plant at Buschhutten." *Stahl und Eisen*, v. 106, no. 23, p. 27-33, 1986.

[4] USS Research Continuous Casting Technology Course. December 5-9, 1994, Monroeville, PA.

[5] T. Honeyands, J. Lucas, J. Chambers, and J. Herbertson. "Preliminary Modelling of Steel Delivery to Thin Slab Caster Moulds." *1992 Steelmaking Conference Proceedings*, 1992, p. 451-459.

[6] T.A. Honeyands and J. Herbertson. "Oscillations in Thin Slab Caster Mould Flows." *127th ISIJ Meeting*, March, 1994, Tokyo, Japan.

[7] J.Y. Lamant, M. Larrecq, A. Mouchette, Y. Codur, J. Gancarz, A. Leclercq. "Advanced Control of Mold Operation and Improved Slab Surface Quality on Sollac Continuous Casters." *Proceedings of the Sixth International Iron and Steel Congress*, 1990, Nagoya, Japan, p. 317-324.

[8] H. Tanaka, H. Kuwatori, and R. Nisihara. "Analysis of Continuous Casting Powder Entrapping Phenomena by Water-Model Experiments." *Journal of the ISIJ*, Vol. 78, no. 5, 1992, p. 73-78.

[9] J. Kubota, K. Okimoto, M. Suzuki, A. Shirayama, and T. Masaoka. "Mechanism of Level Fluctuation and Mold Powder Catching in Slab Continuous Casting at High Speeds." *Proceedings of the Sixth International Iron and Steel Congress*, 1990, Nagoya, Japan, p. 356-363.

[10] S. Feldbauer, I. Jimbo, A. Sharan, K. Shimizu, W. King, J. Stepanek, J. Harman, and A.W. Cramb. "Physical Properties of Mold Slags That Are Relevant to Clean Steel Manufacture." *1995 Steelmaking Conference Proceedings*, 1995, p. 655-667.

[11] R. Bommaraju, T. Jackson, J. Lucas, and G. Skoczylas. "Design, Development and Application of Mold Powder to Reduce Slivers." *Continuous Casting Volume Seven*, ISS, 1995, p. 165-171.

[12] A.W. Cramb, Y. Chung, J. Harman, A. Sharan, and I. Jimbo. "The Slag/Metal Interface and Associated Phenomena." *Iron and Steelmaker (USA)*, Vol. 74, no. 3, 1997, p. 77-83.

[13] N.A. McPherson and S.L. McIntosh. "Mould Powder Related Defects in Some Continuously Cast Steel Products." *Continuous Casting Volume Seven*, ISS, 1995, p. 145-153.

[14] M. Byrne, A.W. Cramb, and T.W. Fenicle. "The Sources of Exogenous Inclusions in Continuous Cast, Aluminum-Killed Steels." *Continuous Casting Volume Seven*, ISS, 1995, p. 133-143.

[15] J.M. Harman and A.W. Cramb. "A Study of the Effect of Fluid Physical Properties upon Droplet Emulsification." *1996 Steelmaking Conference Proceedings*, 1996, p. 773-784.

[16] S. Feldbauer and A.W. Cramb. "Insights into Slag Entrainment in the Mold of a Continuous Caster." *13th PTD Conference Proceedings*, 1996, p. 327-340.

[17] M. Gebhard, Q.L. He, and J. Herbertson. "Vortexing Phenomena in Continuous Slab Casting Moulds." *1993 Steelmaking Conference Proceedings*, 1993, p. 441-446.

[18] R.M. McDavid and B.G. Thomas. "Flow and Thermal Behavior of the Top Surface Flux/Powder Layers in Continuous Casting Molds." *Metallurgical and Materials Transactions B*, Vol. 27B, August, 1996, p. 672-685.

[19] B.G. Thomas, Q Yuan, S. Sivaramakrishnan, T. Shi, S.P. Vanka, M.B. Assar. "Comparison of Four Methods to Evaluate Fluid Velocities in a Continuous Slab Casting Mold." *ISIJ International*, Vol. 41, No. 10, 2001, p. 1262-1271.

[20] B.G. Thomas, A. Dennisov and H. Bai. "Behavior of Argon Bubbles During Continuous Casting of Steel." *1997 Steelmaking Conference Proceedings*, 1997, p. 375-391.

[21] A.C. Mikrovas and S.A. Argyropoulos. "A Novel Technique to Estimate Velocity in Liquid Steel and in Other High Temperature Liquid Metals." *Iron and Steelmaker*, October 1993, p. 85-93.

[22] M. Hanao, M. Kawamoto, H. Mizukami, and K. Hanazaki. "Influence of Velocity of Molten Steel Flow near the Meniscus in a Continuous Casting Mold on Surface Quality of Slabs." *1999 Steelmaking Conference Proceedings*, 1999, p. 63-70.

[23] H. Mizukami, M. Hanao, S. Hiraki, and M. Kawamoto, T. Watanabe, A. Hayashi, and M. Iguchi. "Measurement of Meniscus Flow Velocity in High Speed Continuous Casting Mold." *Tetsu-to-Hagane*, Vol. 86, no. 4, 2000, p. 63-68.

[24] S.A. Argyropoulos. "Measurement of Velocity in High Temperature Metals and Slags." *Fundamentals of Metallurgical Processing: The James M. Toguri Symposium (Canada)*, August 2000, p. 31-42.

[25] T. Koeplin. Telephone conversation in October 2000.

[26] B.G. Thomas and Hua Bai. "Tundish Nozzle Clogging - Application of Computational Models." *18th PTD Conference Proceedings*, Vol. 18, 2001.

[27] S.G. Kollberg, H.R. Hackl, and P.J. Hanley. "Improving quality of flat rolled products using electromagnetic brake (EMBR) in continuous casting." *Iron and Steel Engineer*, Vol. 73, no. 7, 1996, p. 24-28.

[28] J. Lehmann, M. Boher, and M.C. Kaerle. "An experimental study of the interactions between liquid steel and a MgO-based tundish refractory." *CIM Bulletin*, Vol. 90, no. 1013, 1997, p. 69-74.

[29] W. Holler. "Prevention of alumina clogging in submerged nozzles for continuous casting of steel by introduction of a carbon-free inner layer." *Veitsch-Radex Rundschau (Germany)*, Vol. 1, 1999, p. 30-39.

[30] Ravi Rastogi and Alan Cramb. Personal Communication, 2002.

[31] W. Lai, M. Milone, and I.V. Samarasekera. "Meniscus Thermal Analysis as a Tool for Evaluating Slab Surface Quality." Unpublished Research, University of British Columbia, 1999.

[32] X. Huang and B.G. Thomas. "Modeling of Transient Flow Phenomena in Continuous Casting of Steel." *Canadian Metallurgical Quarterly*, Vol. 37, no. 3-4, 1998, p. 197-212.

[33] M. Byrne and A.W. Cramb. "Operating Experience with Large Tundishes." *Continuous Casting Volume Seven*, ISS, 1995, p. 155-164.

[34] *Continuous Casting Volume Seven*, ISS, 1995.

[35] C.G. Aneziris, E.M. Pfaff, and H.R. Maier. "The Zirconia/Slag/Air Interface of Zirconia Based Submerged Entry Nozzles During Near Net Shape Steel Casting." *British Ceramic Proceedings (UK)*, Vol. 60, no. 1, 1999, p. 459-460.

[36] D.E. Larson. Nucor Steel, Personal Communication, December 18-20, 2000.

[37] M.S. Jenkins, B.G. Thomas, W.C. Chen, and R.B. Mahapatra. "Investigation of Strand Surface Defects Using Mold Instrumentation and Modelling." *1994 Steelmaking Conference Proceedings*, 1994, p. 337-345.

[38] F.M. Najjar, B.G. Thomas, and D.E. Hershey. "Numerical Study of Steady Turbulent Flow through Bifurcated Nozzles in Continuous Casting." *Metallurgical and Materials Transactions B*, Vol. 26B, August 1995, p. 749-765.

[39] H.B.M. Schulte, R.H.M.G. Nabben, D.W. van der Plas, and D. Triezenberg. "Study of the fluid flow in the mould for high quality slab casting." *Le Revue de Metallurgie-CIT*, June 1997, p. 751-759.

[40] A. Vaterlaus. "Innovative Clogging Prevention and Mold Flow Optimization by the Whirl SEN." *1997 Steelmaking Conference Proceedings*, 1997, p. 165-172.

[41] L.J. Heaslip and J. Schade. "Physical Modeling and Visualization of Liquid Steel Flow Behavior During Continuous Casting." *Iron and Steelmaker*, Vol. 26, no. 1, 1999, p. 33-41.

[42] H. Nam, H. Park, and J.K. Yoon. "Numerical Analysis of Influences of Operation Parameters on Fluid Flow and Heat Transfer in Funnel Type Mold of Thin Slab Casters." *Second International Conference on Processing Materials for Properties*, TMS, 2000, p. 363-368.

[43] J.D. Lee and C.H. Yim. "The Mechanism of Unsteady Bulging and Its Analysis with the Finite Element Method for Continuously Cast Steel." *ISIJ International*, Vol. 40, no. 8, 2000, p. 765-770.

[44] S. Kumar, B.N. Walker, I.V. Samarasekera, and J.K. Brimacombe. "Chaos at the Meniscus - The Genesis of Defects in Continuously Cast Steel Billets." *13th PTD Conference Proceedings*, 1995, p. 119-141.

[45] D.T. Stone and B.G. Thomas. "Measurement and Modeling of Heat Transfer Across Interfacial Mold Flux Layers." *Canadian Metallurgical Quarterly*, Vol. 38, no. 5, 1999, p. 363-375.

[46] H. Yasunaka, K. Nakayama, K. Ebina, T. Saito, M. Kimura, and H. Matuda. "Improvement of Transverse Corner Cracks in Continuously Cast Hypoeutectic Slabs." *Tetsu-to-Hagane*, Vol. 81, no. 9, 1995, p. 894-899.

[47] R.B. Mahapatra, J.K. Brimacombe, I.V. Samarasekera, N. Walker, E.A. Patterson, and J.D. Young. "Mold Behavior and Its Influence on Quality in the Continuous Casting of Steel Slabs: Part 1. Industrial Trials, Mold Temperature Measurements, and Mathematical Modeling." *Metallurgical Transactions B*, Vol. 22B, December 1991, p. 861-874.

[48] R.B. Mahapatra, J.K. Brimacombe, I.V. Samarasekera. ". "Mold Behavior and Its Influence on Quality in the Continuous Casting of Steel Slabs: Part 2. Mold Heat Transfer, Mold Flux Behavior, Formation of Oscillation Marks, Longitudinal Off-Corner Depressions, and Subsurface Cracks." *Metallurgical Transactions B*, Vol. 22B, December 1991, p. 875-888.

[49] T. Techima, J. Kubota, M. Suzuki, K. Ozawa, T. Mosaoka, and S. Miyahara. "Influence of Casting Conditions on Molten Steel Flow in Continuous Casting Mold at High Speed Casting of Slabs." *Tetsu-to-Hagane*, Vol. 79, no. 5, 1993, p. 576-582.

[50] J. Kubota, K. Okimoto, A. Shirayama, and H. Mukarami. "Meniscus flow control in the mold by traveling magnetic field for high speed slab caster." *Mold Operation for Quality and Productivity (USA)*, ISS, 1991, p. 197-205.

[51] I. Lemanowicz, R. Gorissen, H.J. Odenthal, and H. Pfeifer. "Validation of CFD-calculations for the submerged entry nozzle-mould system using the digital particle velocimetry." *Stahl und Eisen*, Vol. 120, no. 9, 2000, p. 85-94.

[52] Microcal Software, Inc. Microcal Origin 6.0. Northampton, MA, 1999.

[53] J.K. Park. "Thermomechanical Phenomena in High Speed Continuous Casting Processes.", PhD Thesis, University of British Columbia, 2002.

[54] K. Schwerdtfeger and H. Sha. "Depth of Oscillation Marks Forming in Continuous Casting of Steel." *Metallurgical and Materials Transactions B (USA)*, Vol. 31B, no. 4, 2000, p. 813-826B.

[55] Sarpkaya. *Mechanics of Wave Forces on Offshore Structures*, 1981, p. 388-396.

[56] Sorenson. *Basic Coastal Engineering*, 1978, p. 32.

[57] RSumer and Fredsøe. *Hydrodynamics Around Cylindrical Structures*, 1997, p. 163-168.

[58] R. Averion and D. Edelman. Nucor Steel, Personal Communication, September 7, 2001.

APPENDIX 1: METAL LEVEL, FFT, AND RAW NAILBOARD RESULTS FOR 2-PORT SEN TRIAL (CASE 4 DATA)

Table A1.1: Pertinent Information for Heats That Were Part of 2-Port SEN Trial.

Heat	Grade	Interval Size (s)	Cast Speed(m/min)	Width (mm)
213760	W3	1100	5.08	1205
117004	W3	3600	5.08	1205
117005	W3	1800	5.08	1205
117006	W3	1800	5.08	1185
213763	W3	1800	4.45	1150

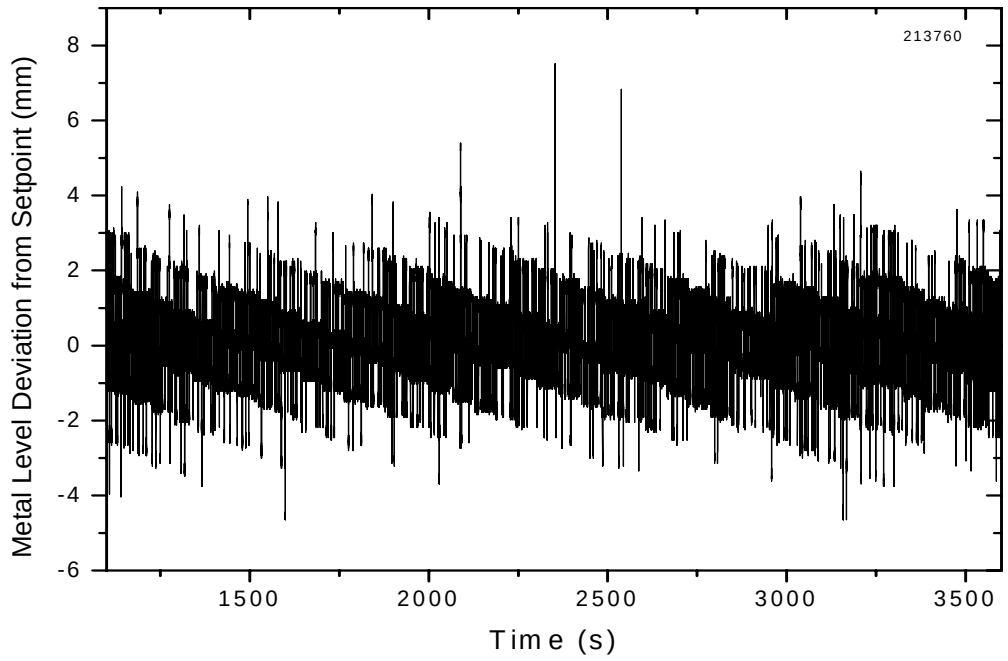

Figure A1.1: Plot of Metal Level Fluctuation from Setpoint for Heat 213760.

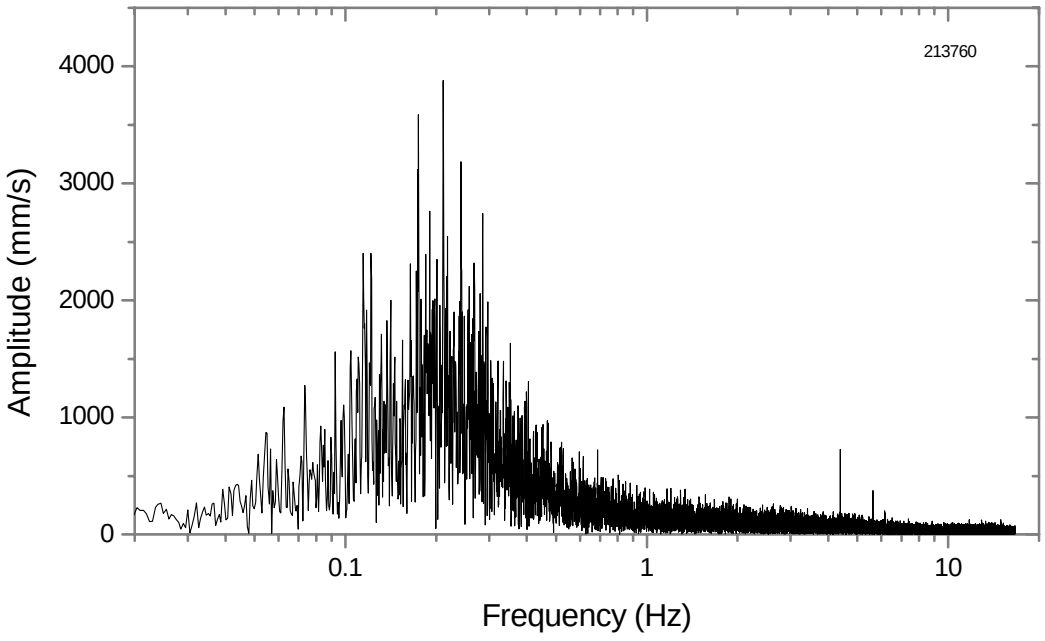

Figure A1.2: FFT Plot of Metal Level Fluctuation for Heat 213760.

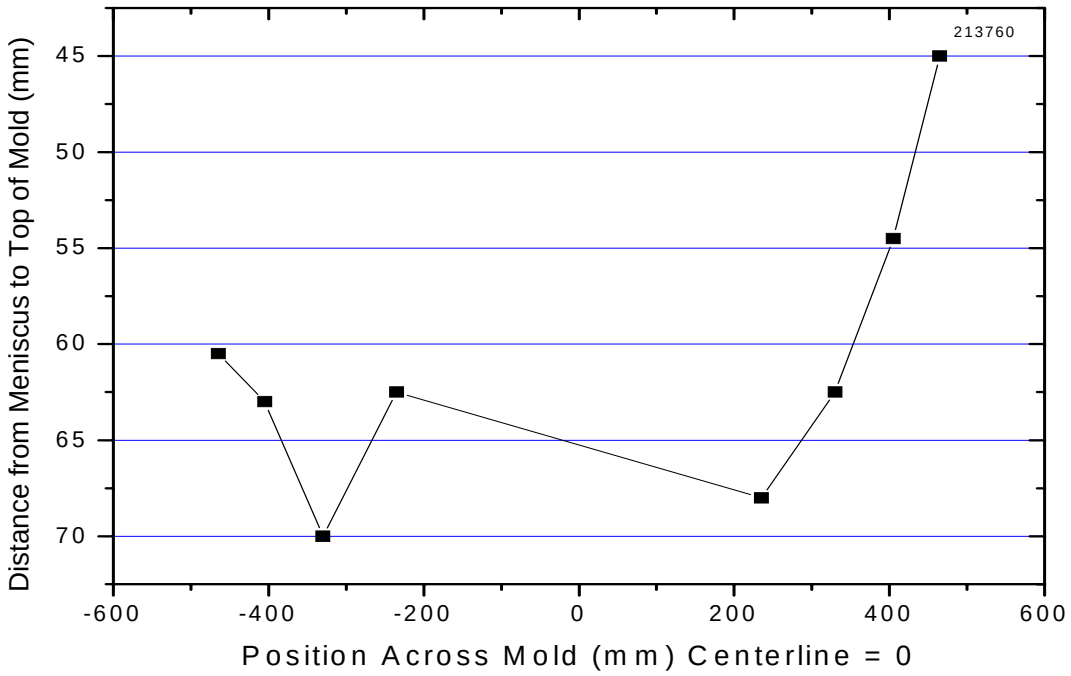

Figure A1.3: Meniscus Shape Profile for Heat 213760.

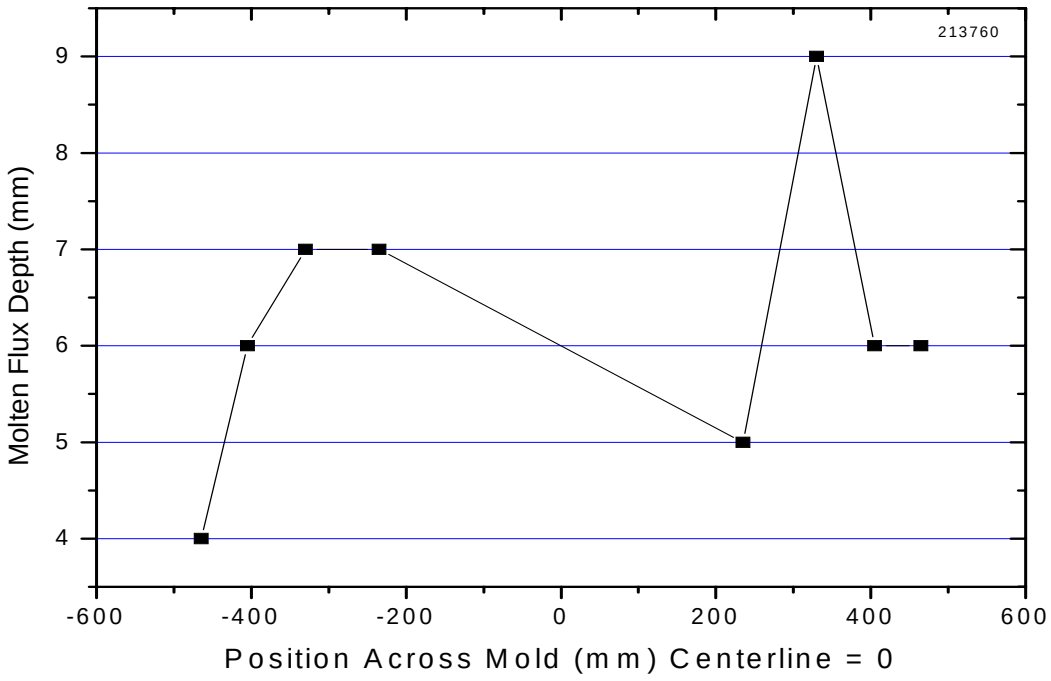

Figure A1.4: Molten Flux Depth Profile for Heat 213760.

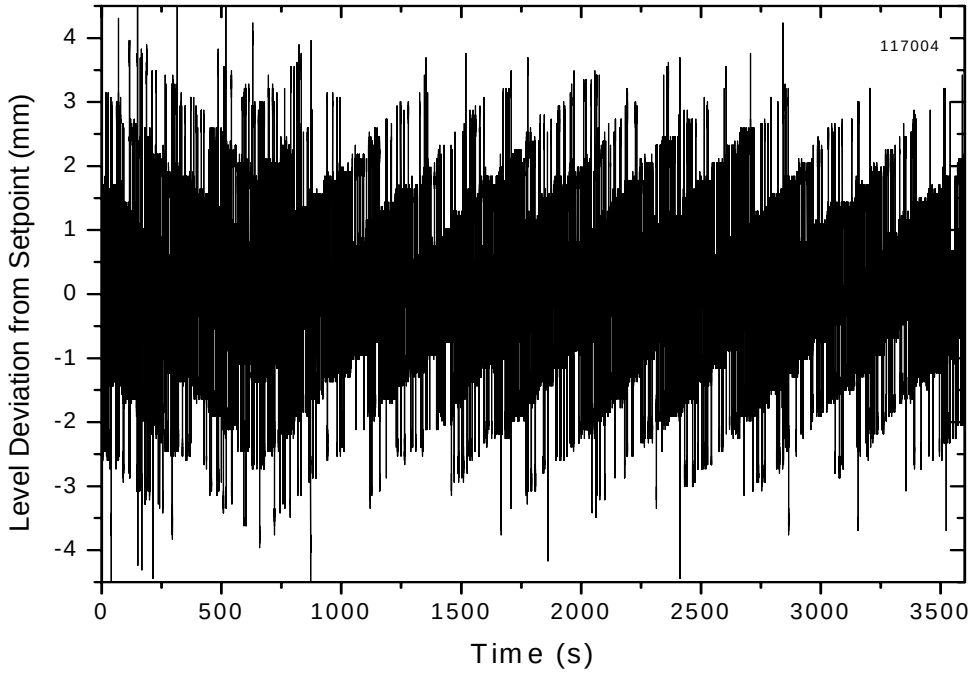

Figure A1.5: Plot of Metal Level Fluctuation from Setpoint for Heat 117004.

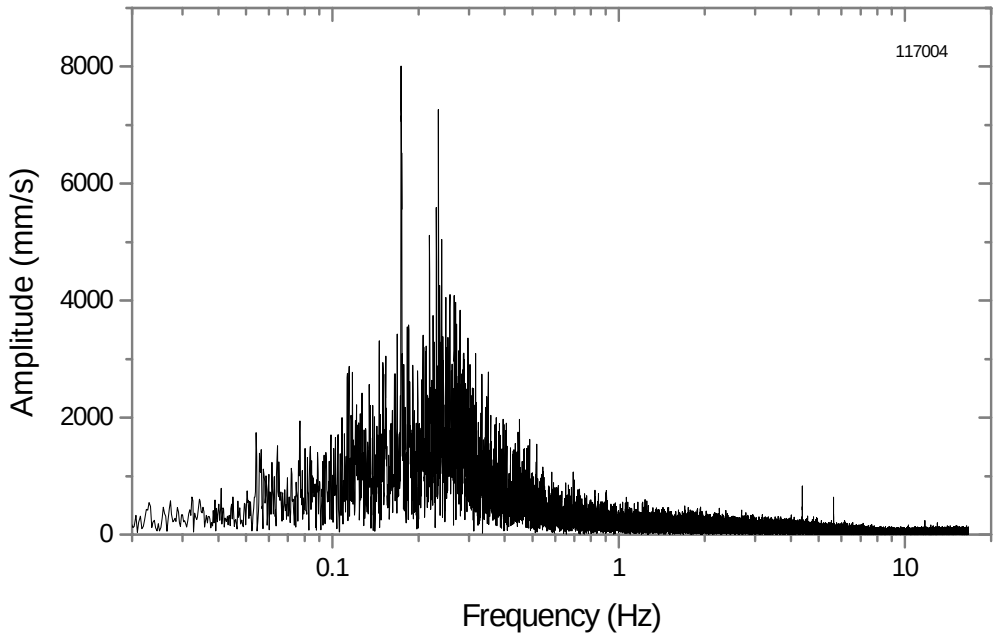

Figure A1.6: FFT Plot of Metal Level Fluctuation for Heat 117004.

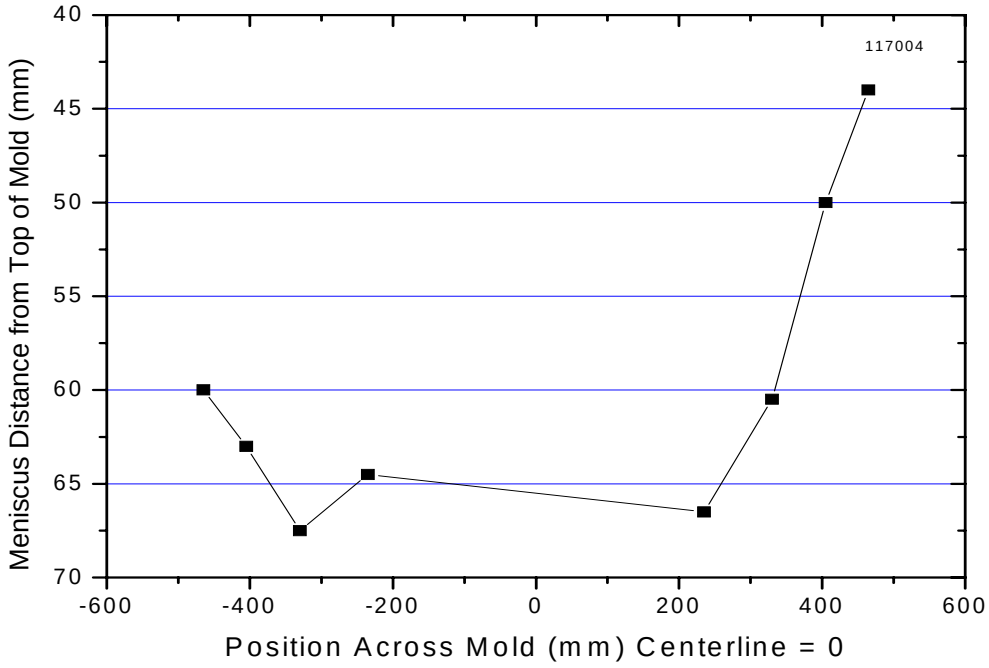

Figure A1.7: Meniscus Shape Profile for Heat 117004.

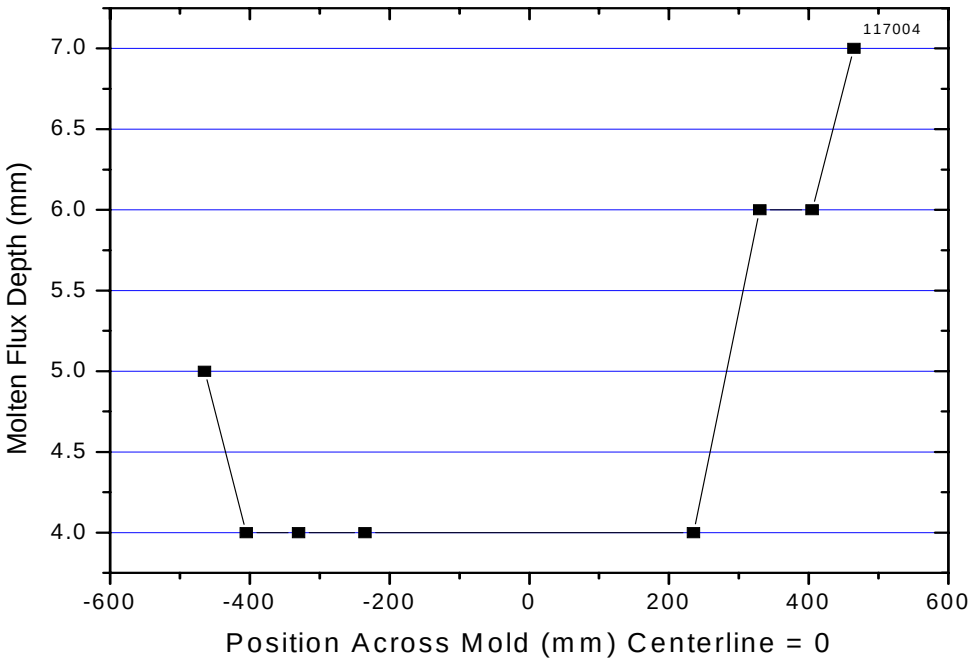

Figure A1.8: Molten Flux Depth Profile for Heat 117004.

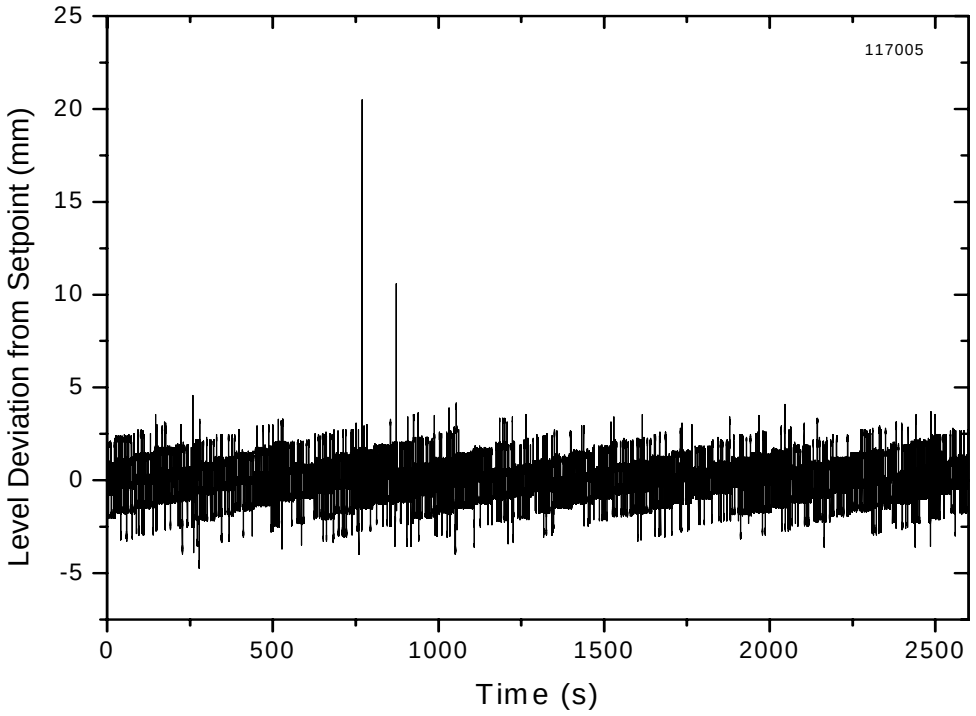

Figure A1.9: Plot of Metal Level Fluctuation from Setpoint for Heat 117005.

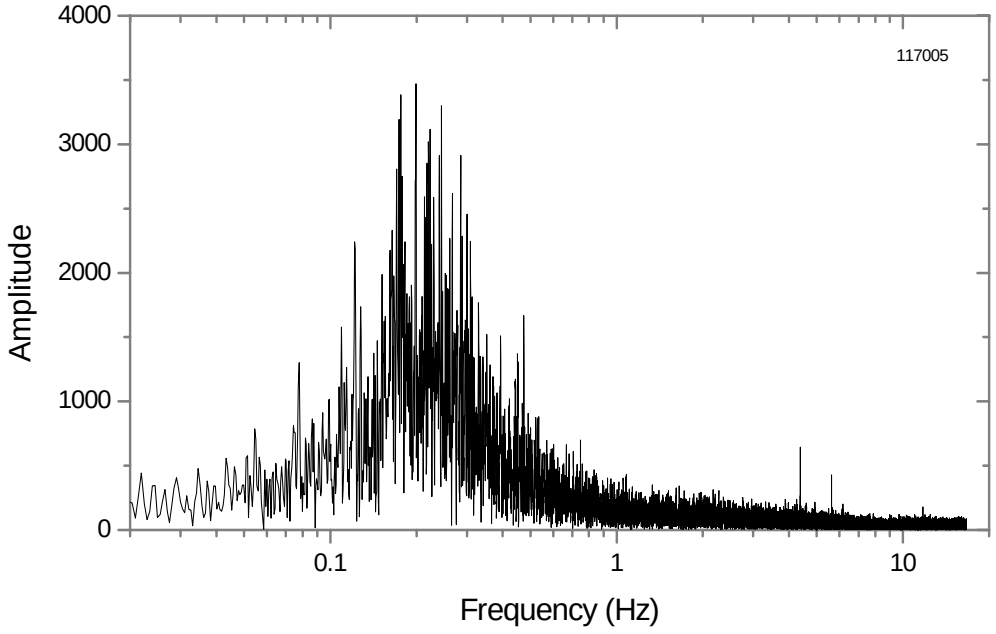

Figure A1.10: FFT Plot of Metal Level Fluctuation for Heat 117005.

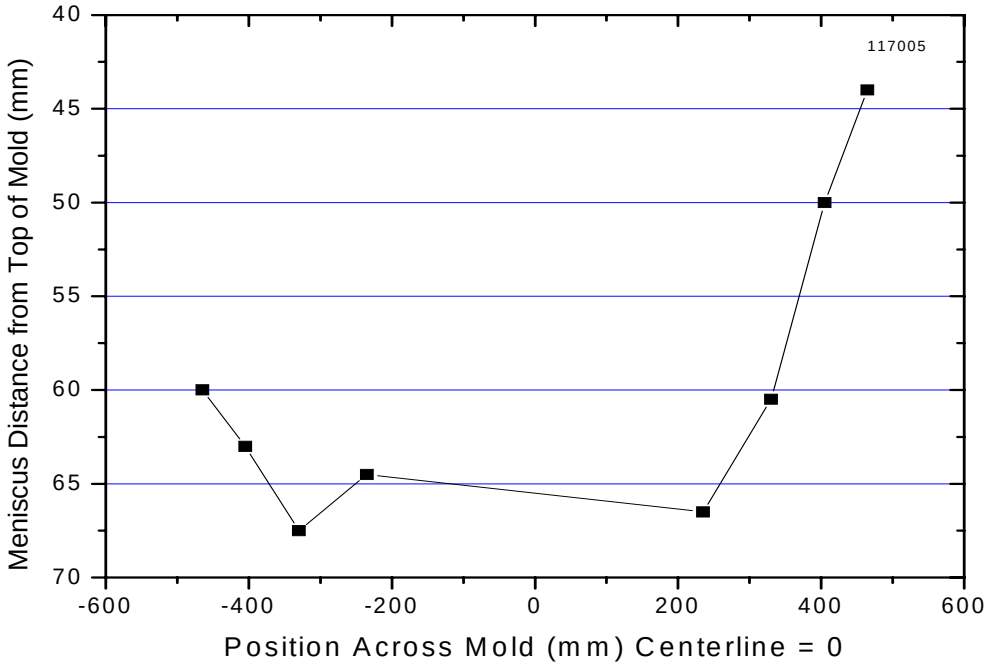

Figure A1.11: Meniscus Shape Profile for Heat 117005.

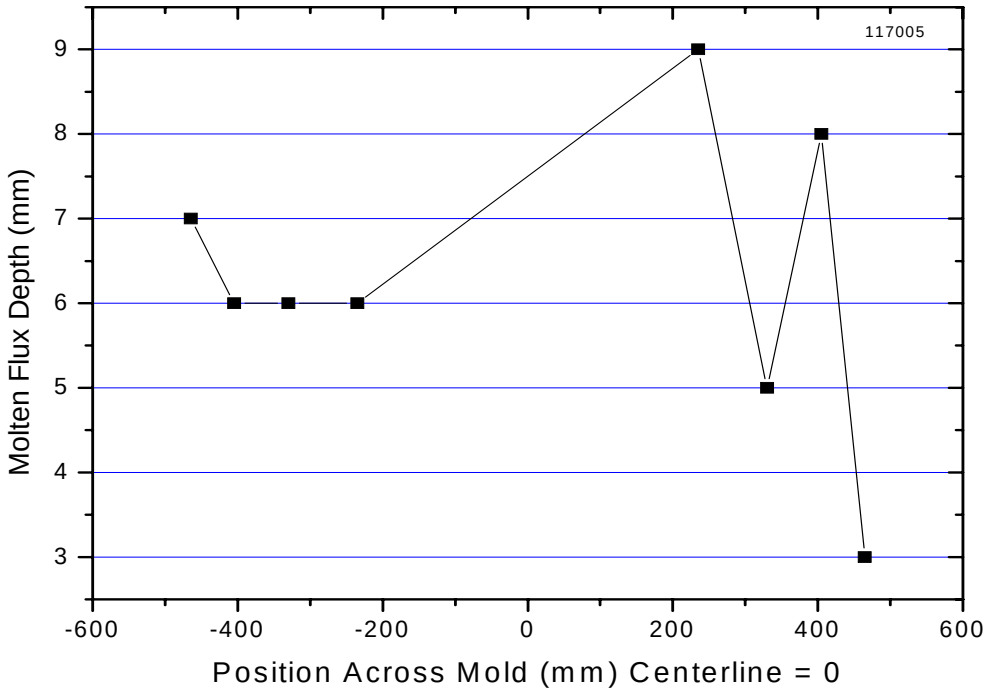

Figure A1.12: Molten Flux Depth Profile for Heat 117005.

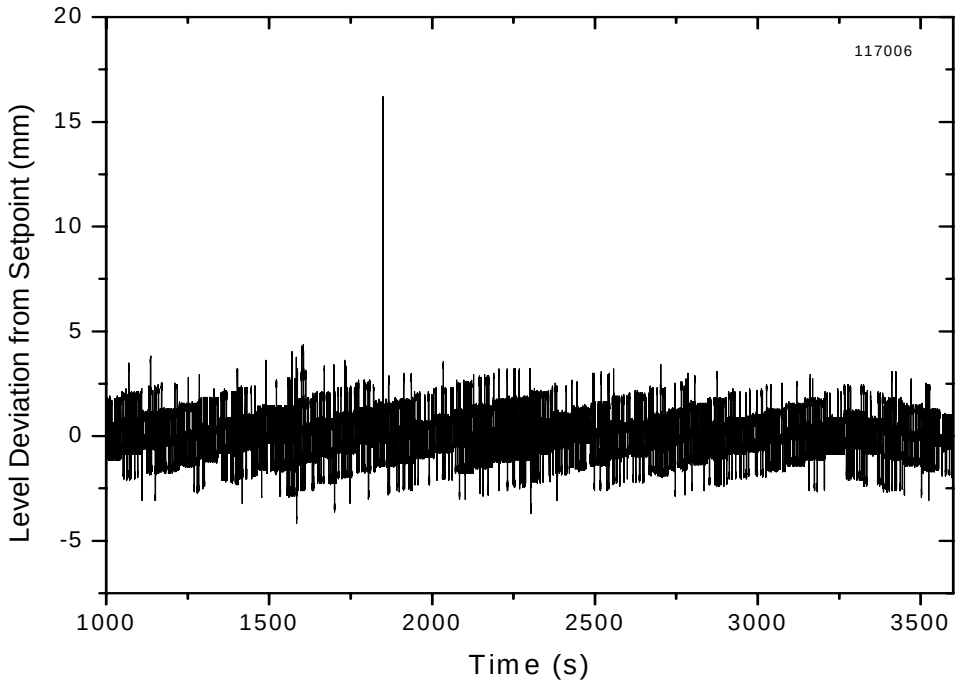

Figure A1.13: Plot of Metal Level Fluctuation from Setpoint for Heat 117006.

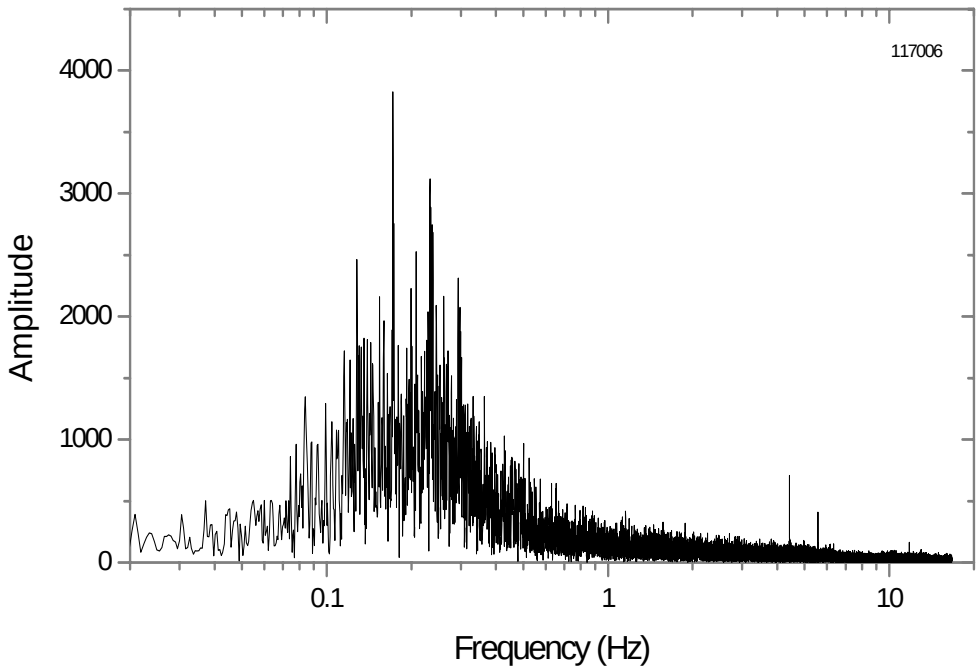

Figure A1.14: FFT Plot of Metal Level Fluctuation for Heat 117006.

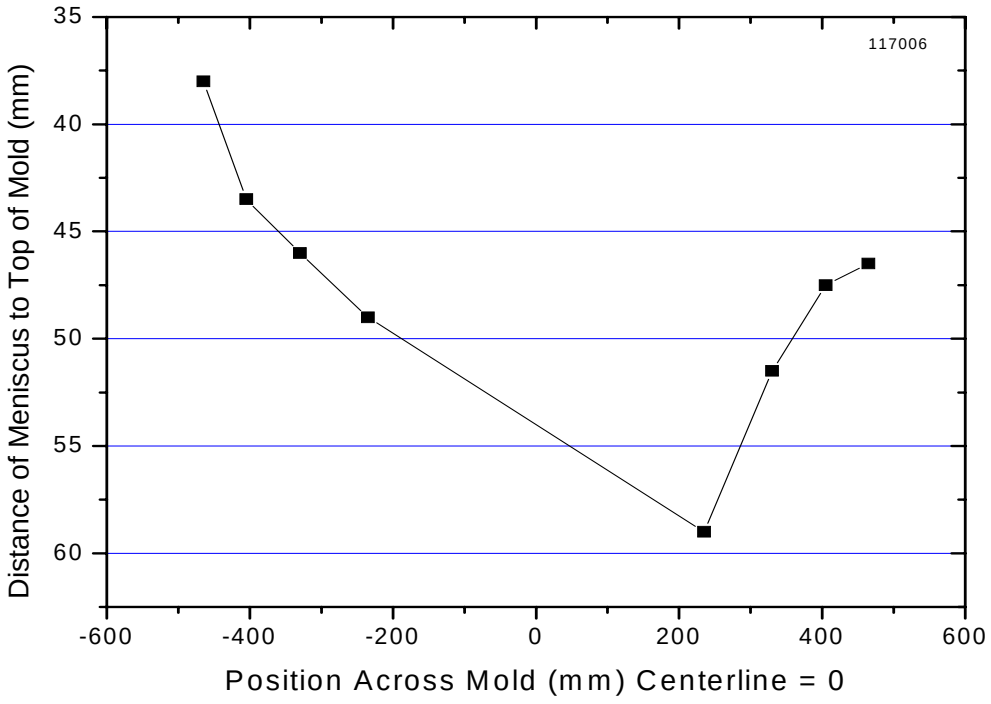

Figure A1.15: Meniscus Shape Profile for Heat 117006.

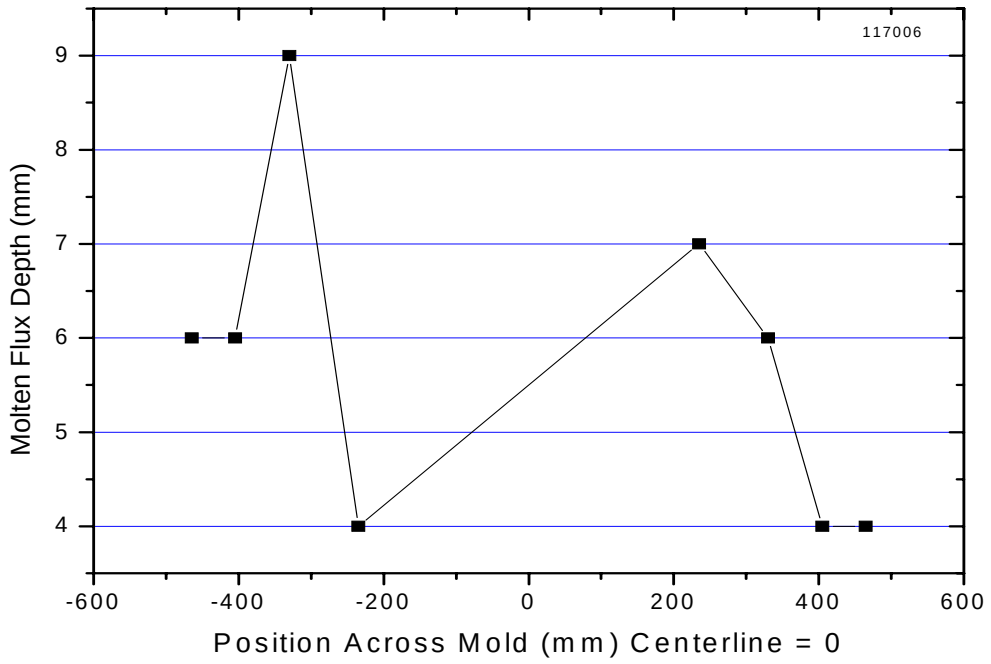

Figure A1.16: Molten Flux Depth Profile for Heat 117006.

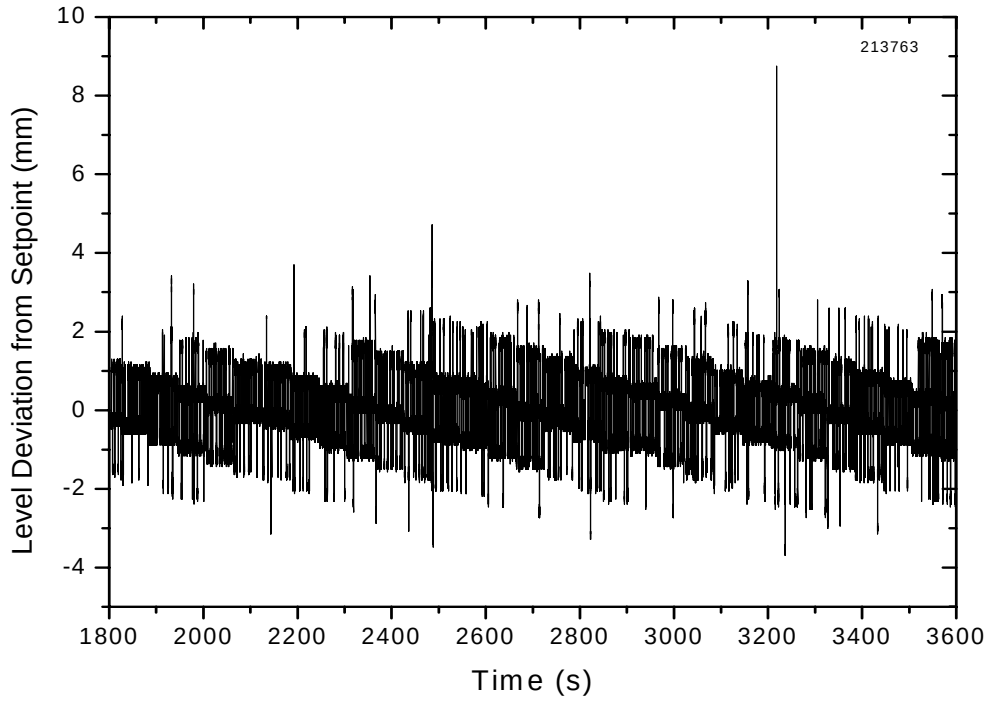

Figure A1.17: Plot of Metal Level Fluctuation from Setpoint for Heat 213763.

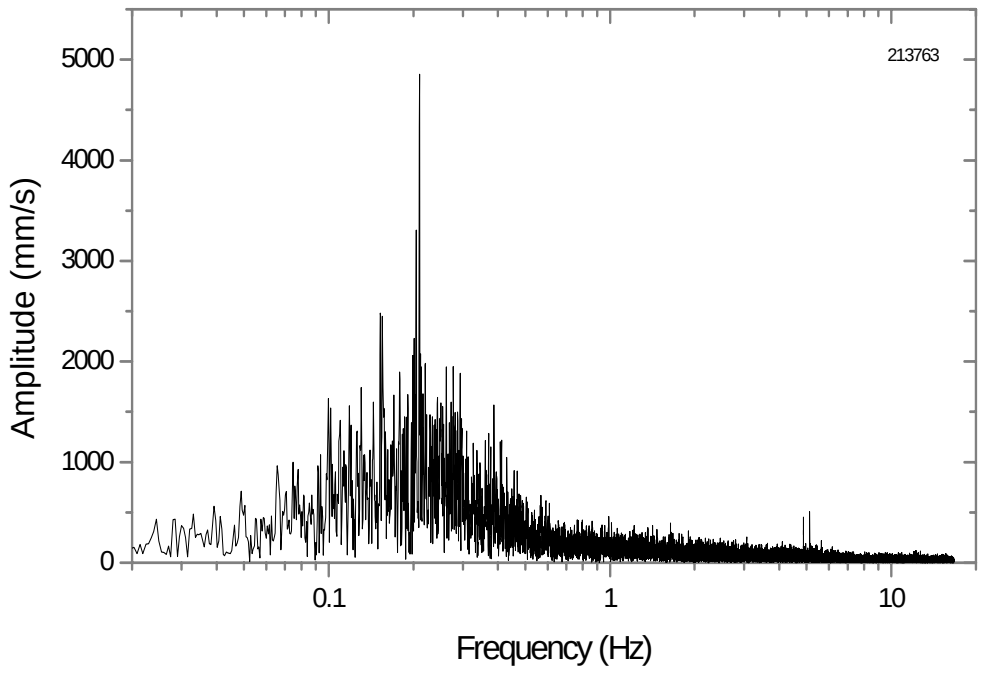

Figure A1.18: FFT Plot of Metal Level Fluctuation for Heat 213763.

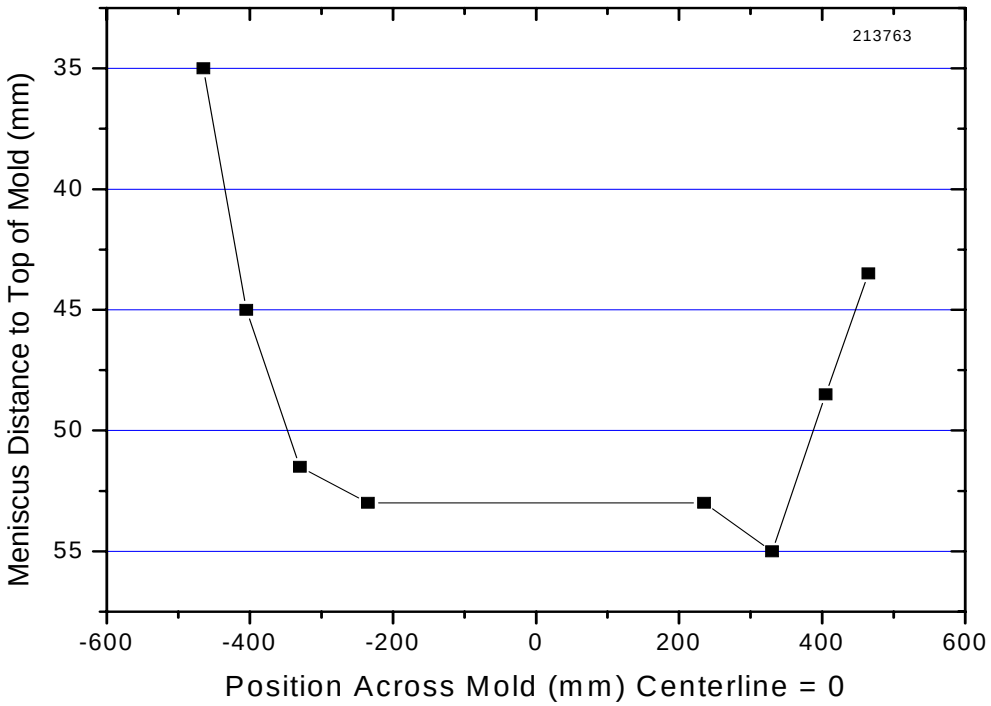

Figure A1.19: Meniscus Shape Profile for Heat 213763.

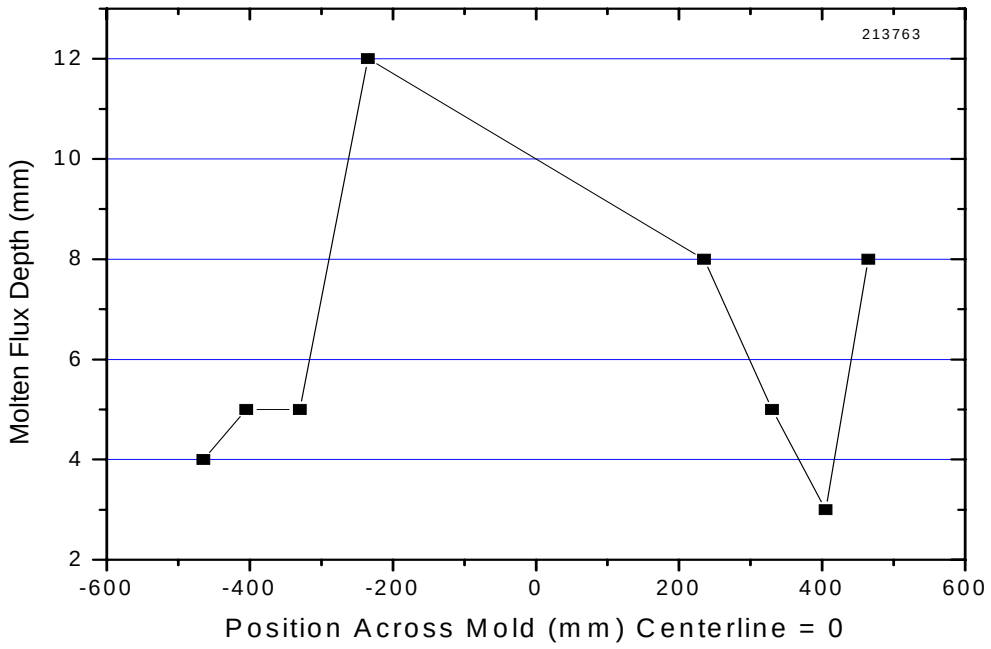

Figure A1.20: Molten Flux Depth Profile for Heat 213763.

APPENDIX 2: METAL LEVEL, FFT, AND RAW NAILBOARD RESULTS FOR 4-PORT SEN TRIAL (CASE 4 DATA)

Table A2.1: Pertinent Information for Heats That Were Part of 4-Port SEN Trial.

Heat	Grade	Interval Size (s)	Cast Speed(m/min)	Width (mm)
117021	T1	1000	3.94	1392
117022	T1	1800	4.57	1392
117023	T1	1800	4.57	1320
117024	T1	1800	4.57	1320
117025	T1	1800	4.57	1320
117026	T1	1700	4.06	1320
213782	T7	1200	4.57	1320
213783	T7	1800	4.57	1285
213784	P1	1800	4.57	1280

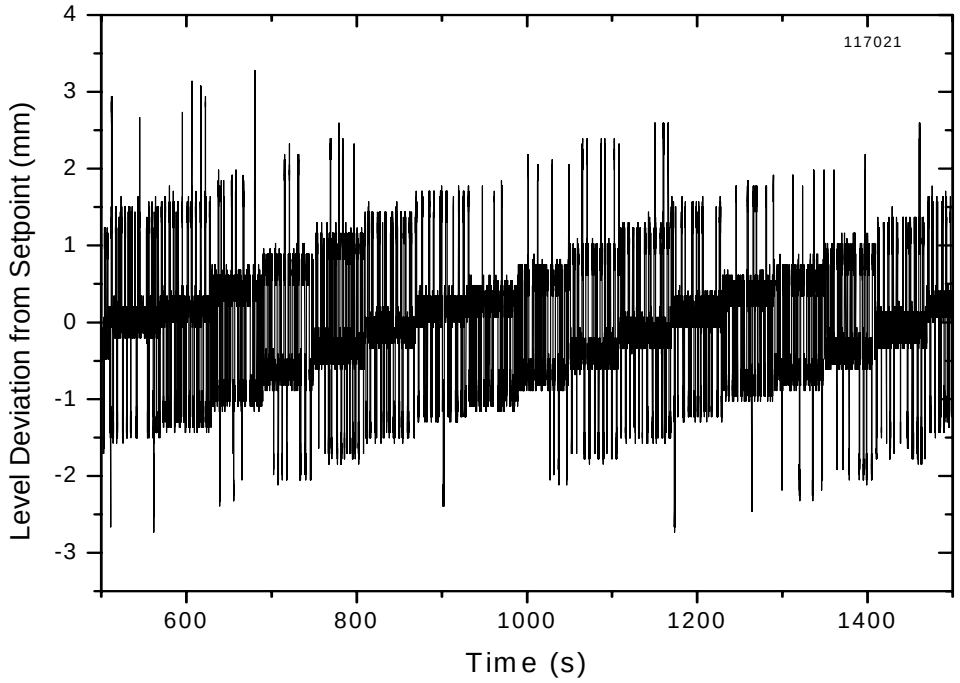

Figure A2.1: Plot of Metal Level Fluctuation from Setpoint for Heat 117021.

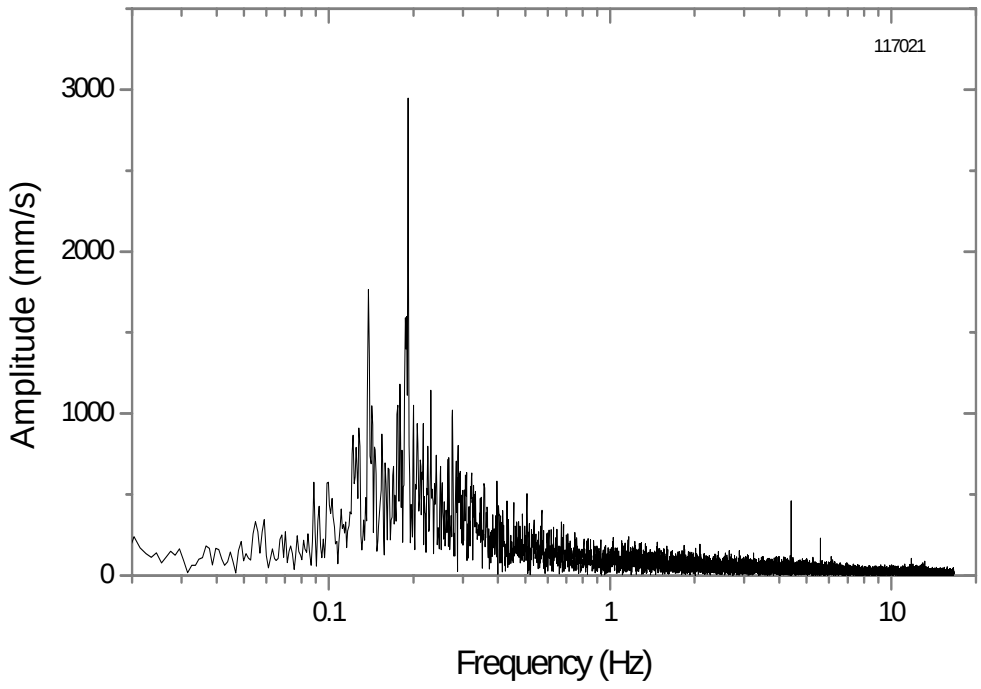

Figure A2.2: FFT Plot of Metal Level Fluctuation for Heat 117021.

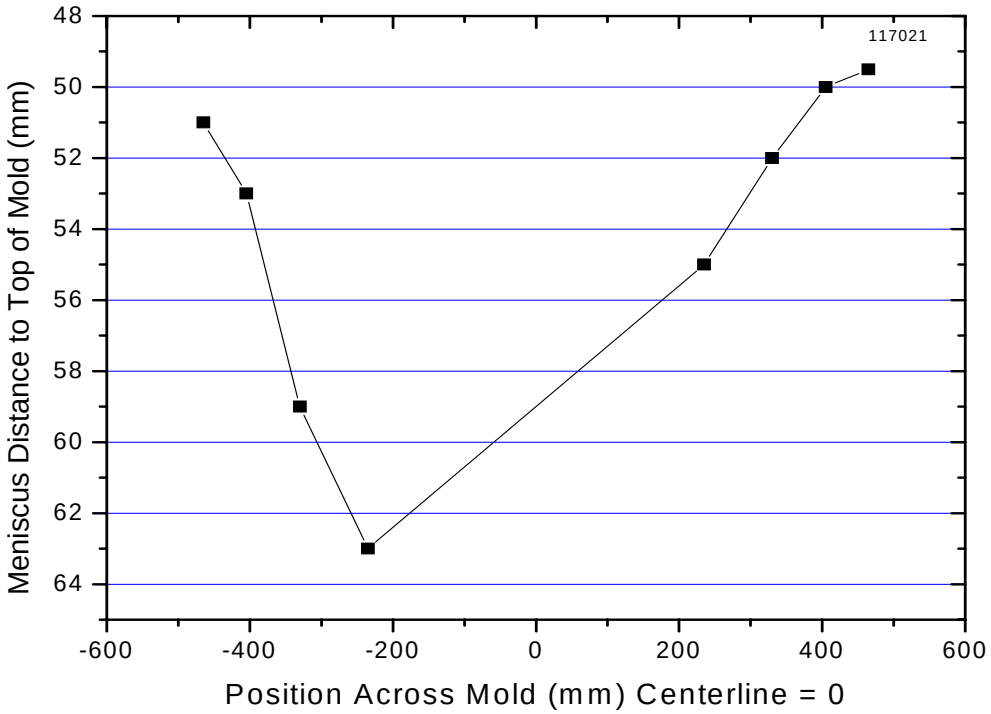

Figure A2.3: Meniscus Shape Profile for Heat 117021.

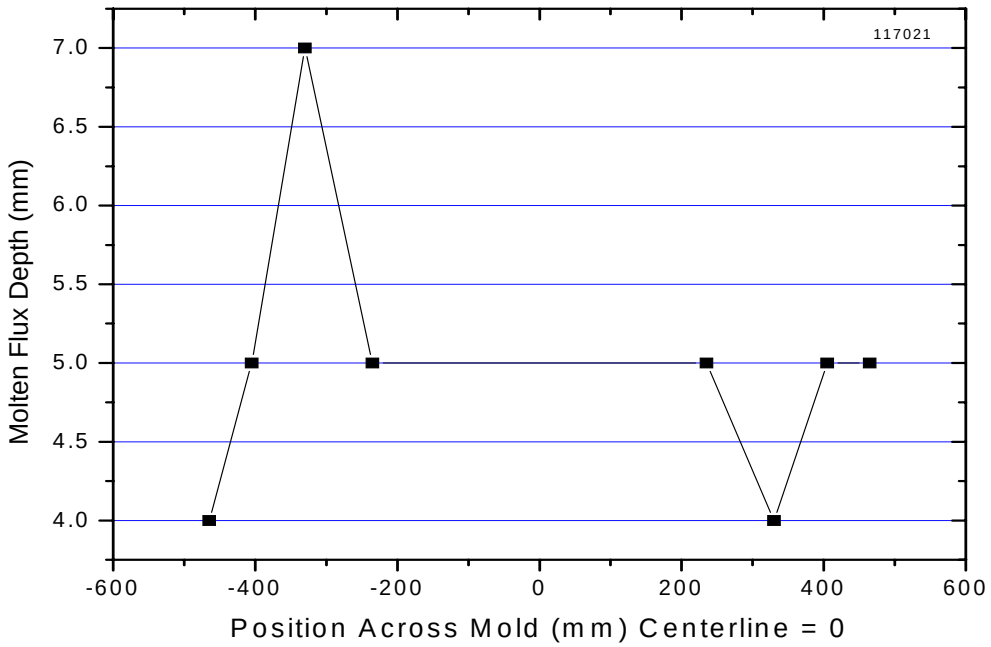

Figure A2.4: Molten Flux Depth Profile for Heat 117021.

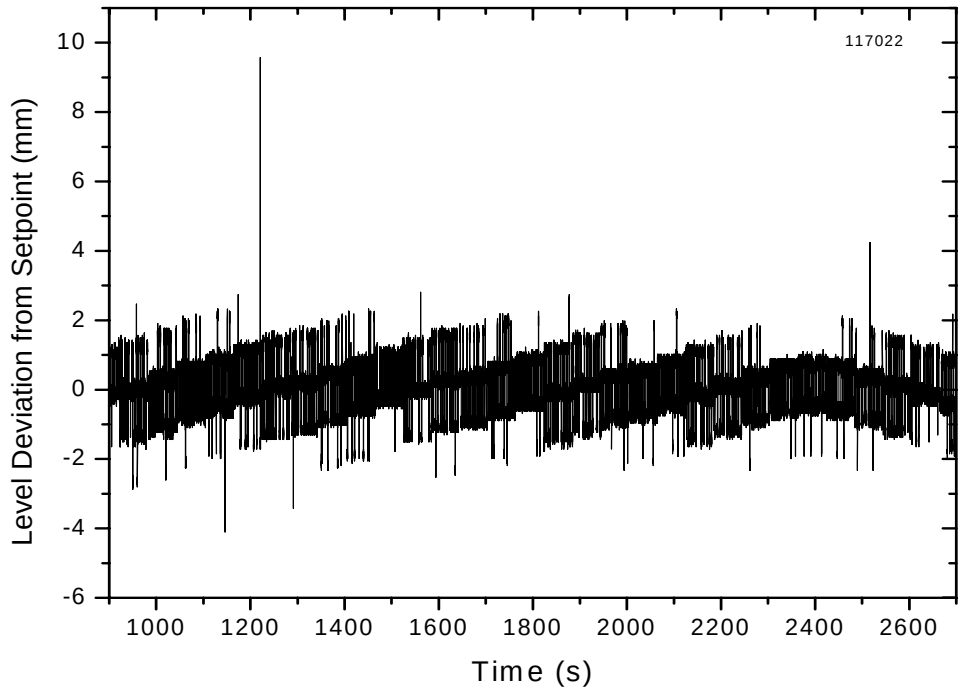

Figure A2.5: Plot of Metal Level Fluctuation from Setpoint for Heat 117022.

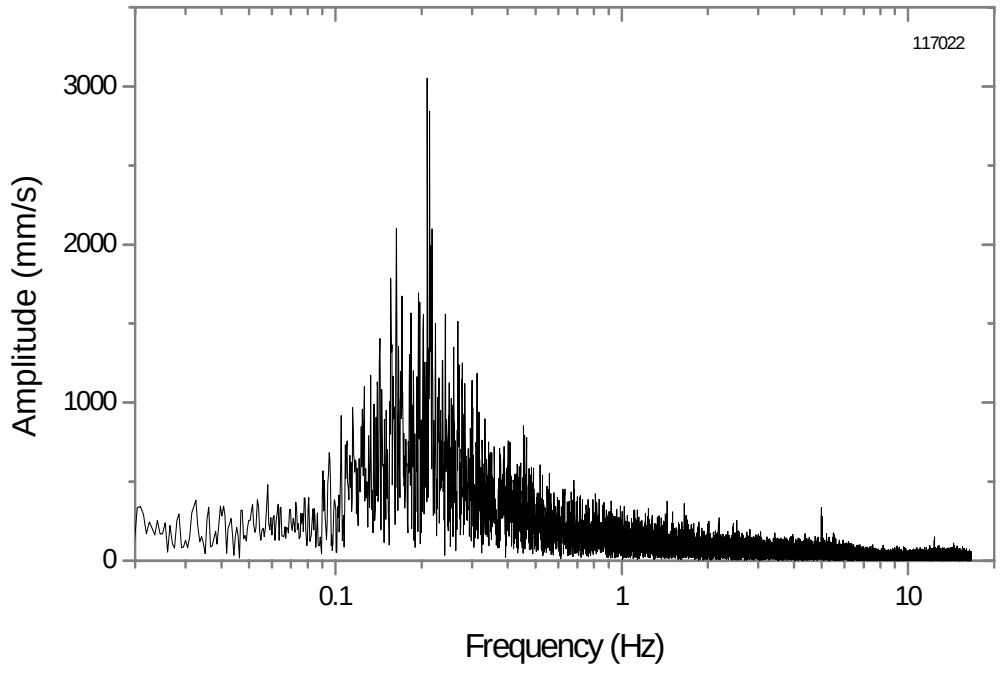

Figure A2.6: FFT Plot of Metal Level Fluctuation for Heat 117022.

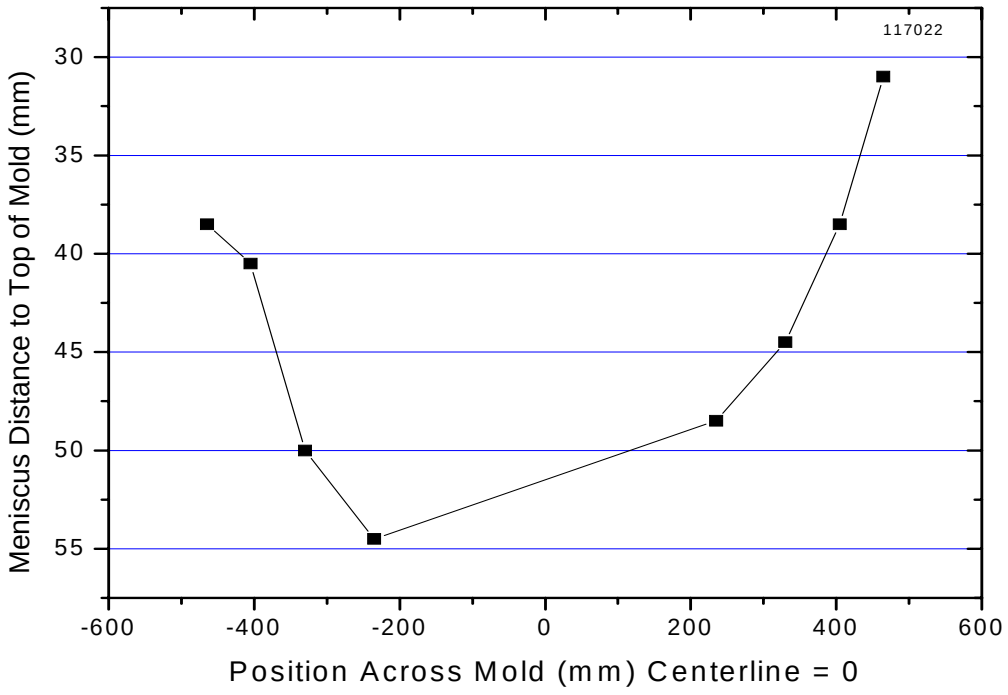

Figure A2.7: Meniscus Shape Profile for Heat 117022.

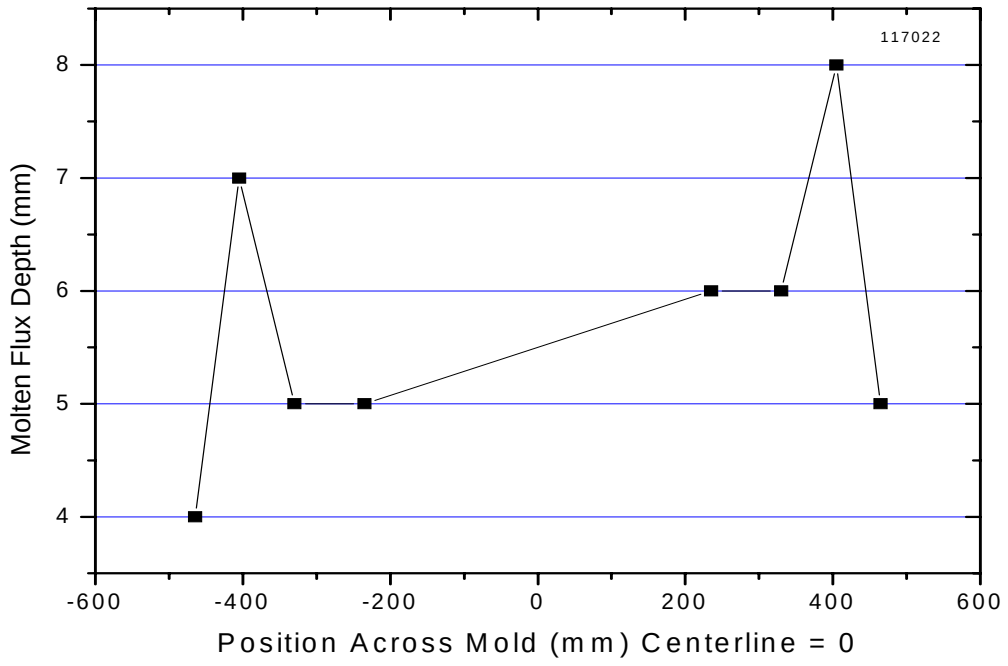

Figure A2.8: Molten Flux Depth Profile for Heat 117022.

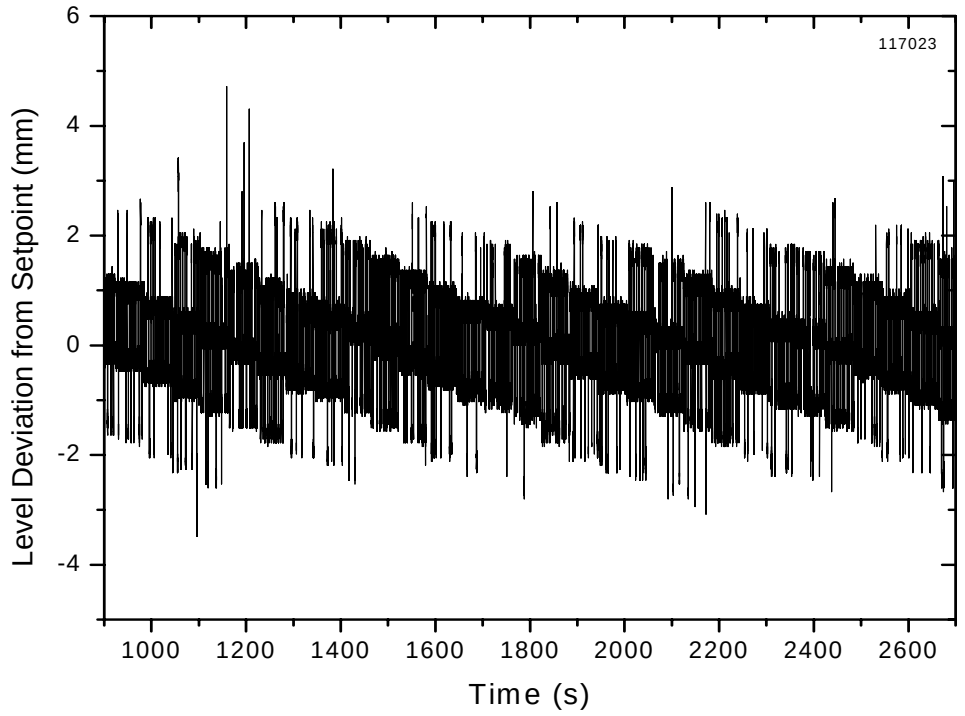

Figure A2.9: Plot of Metal Level Fluctuation from Setpoint for Heat 117023.

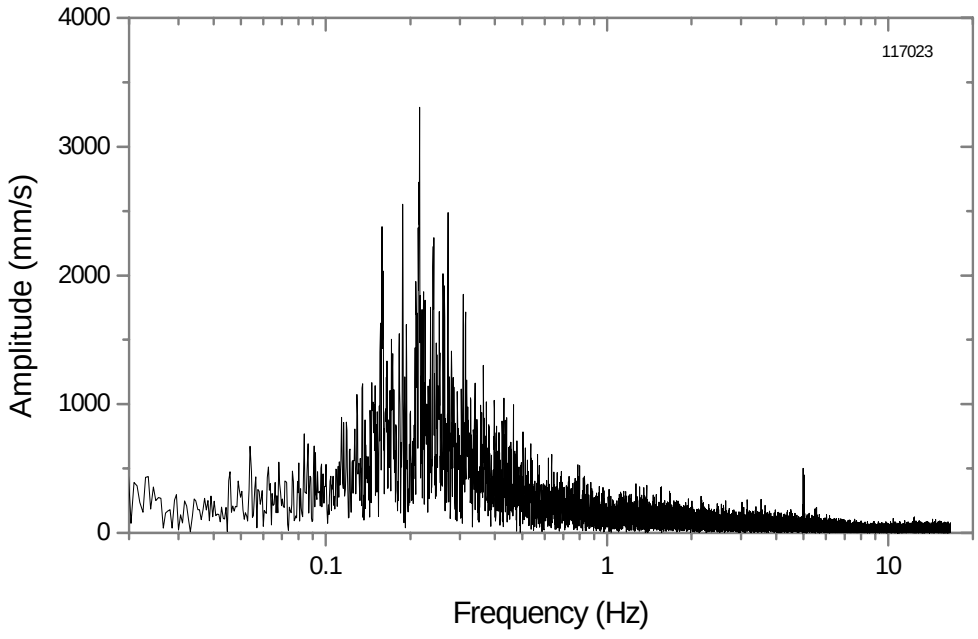

Figure A2.10: FFT Plot of Metal Level Fluctuation for Heat 117023.

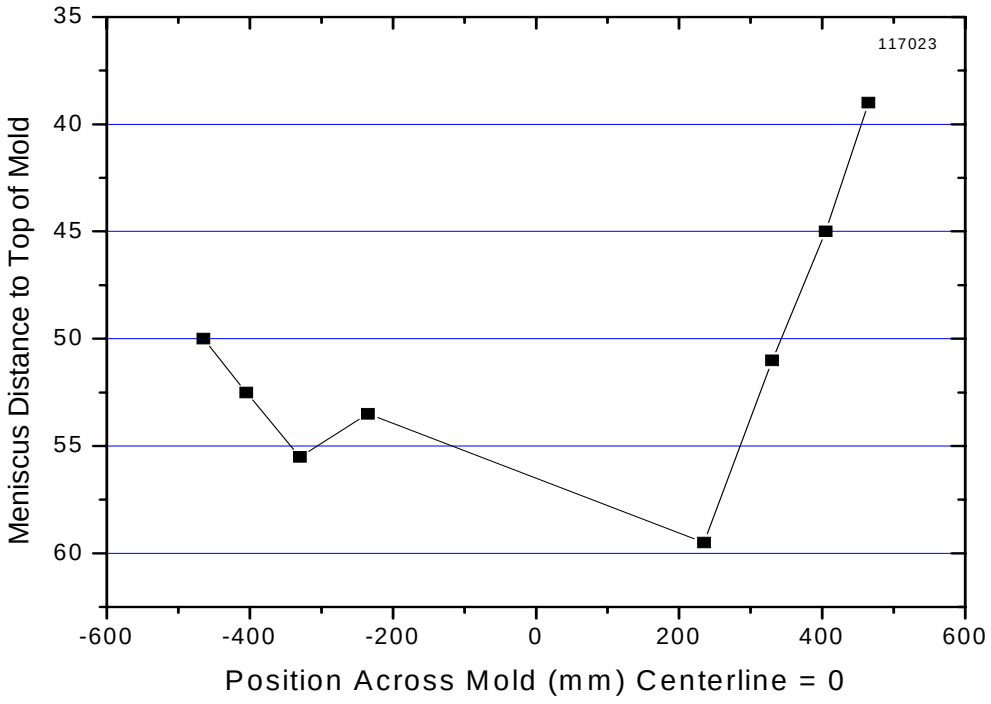

Figure A2.11: Meniscus Shape Profile for Heat 117023.

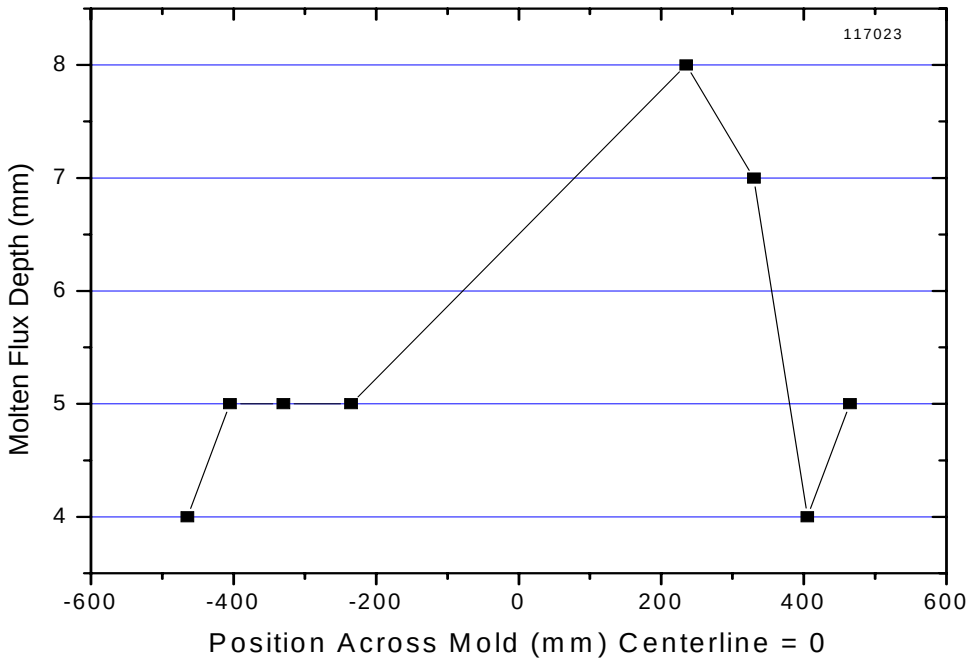

Figure A2.12: Molten Flux Depth Profile for Heat 117023.

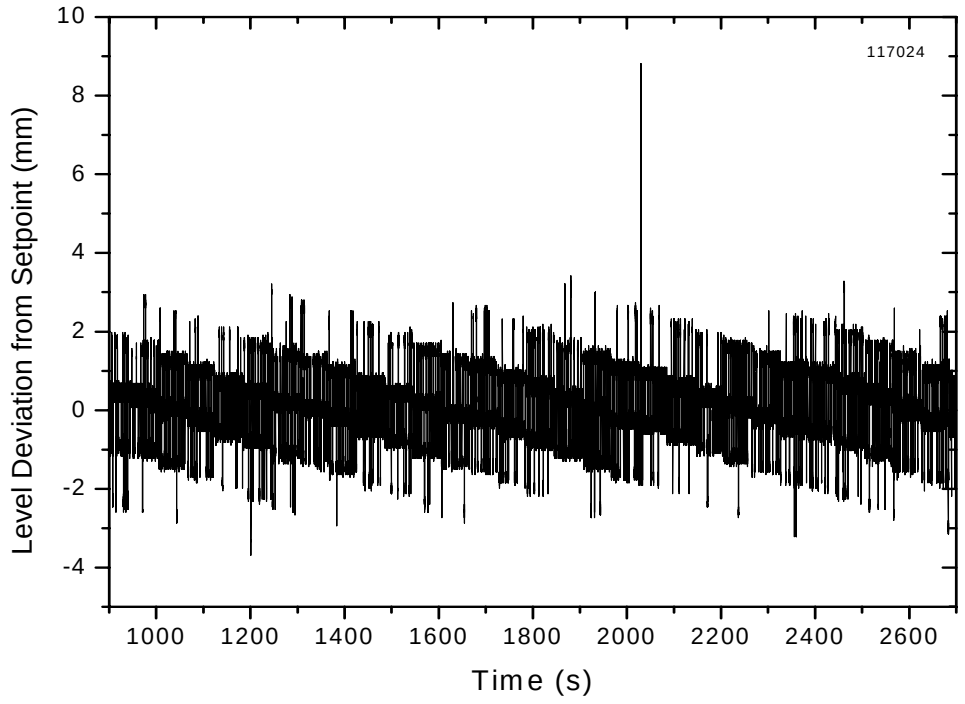

Figure A2.13: Plot of Metal Level Fluctuation from Setpoint for Heat 117024.

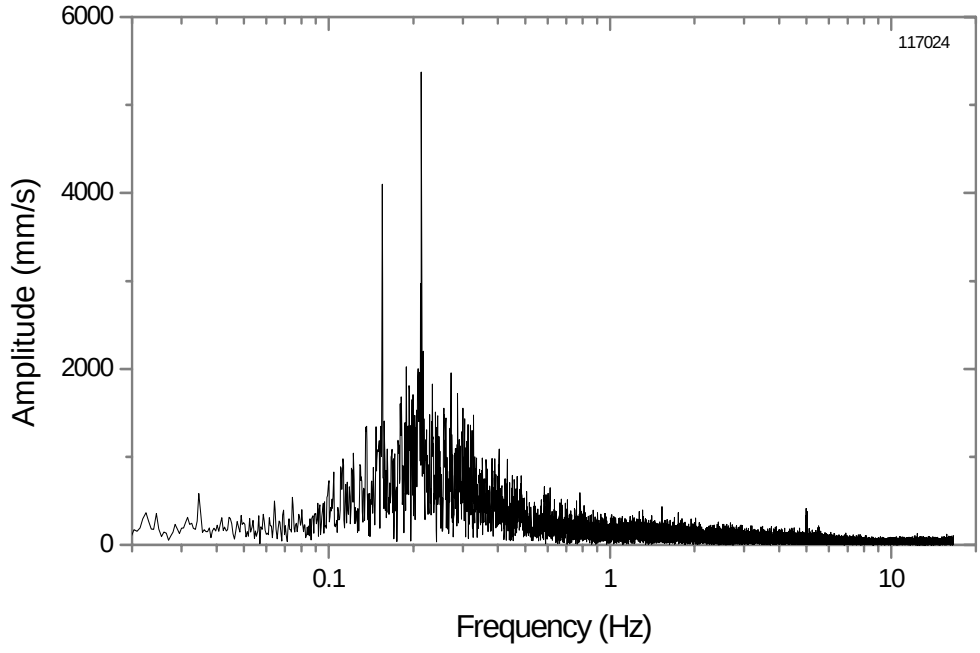

Figure A2.14: FFT Plot of Metal Level Fluctuation for Heat 117024.

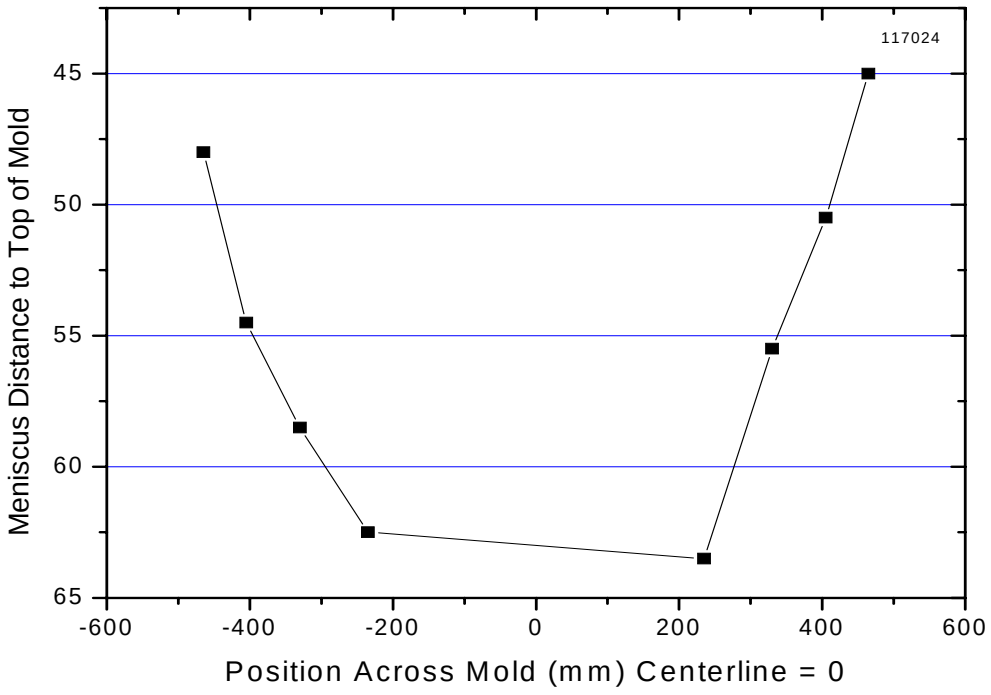

Figure A2.15: Meniscus Shape Profile for Heat 117024.

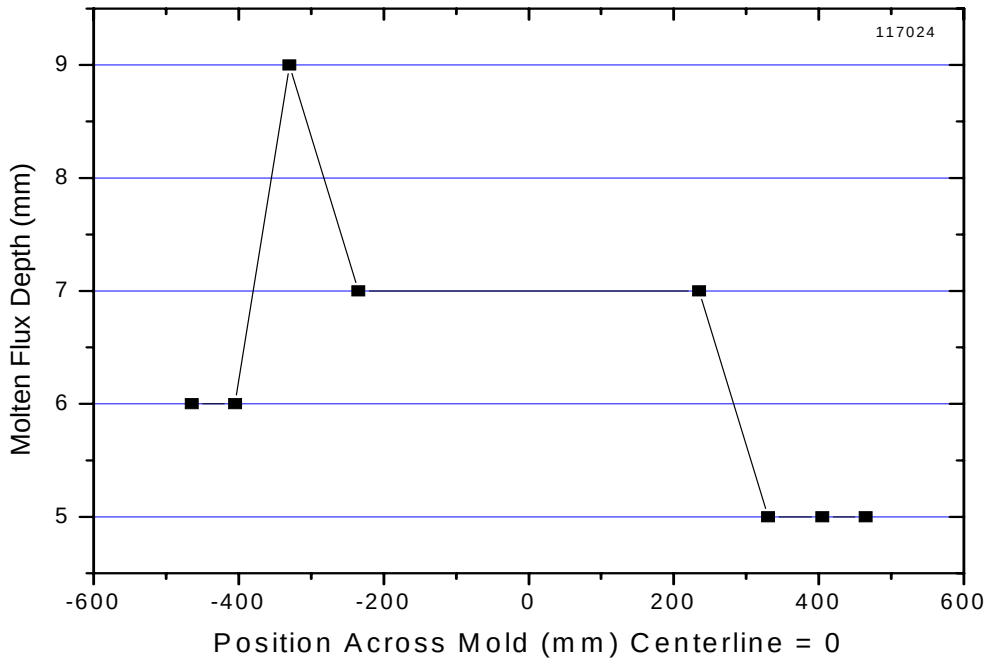

Figure A2.16: Molten Flux Depth Profile for Heat 117024.

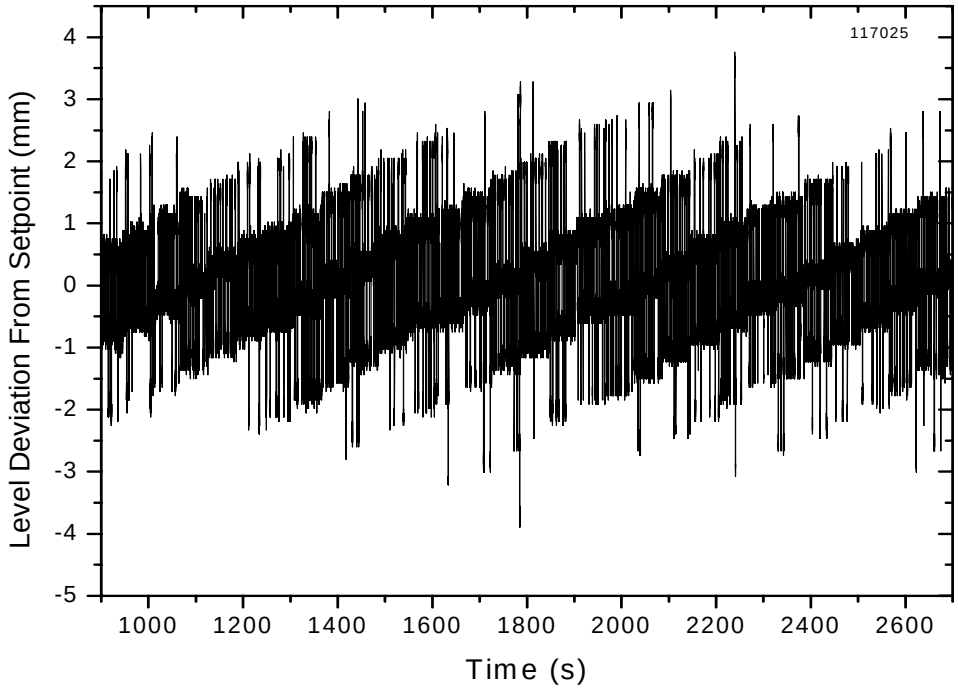

Figure A2.17: Plot of Metal Level Fluctuation from Setpoint for Heat 117025.

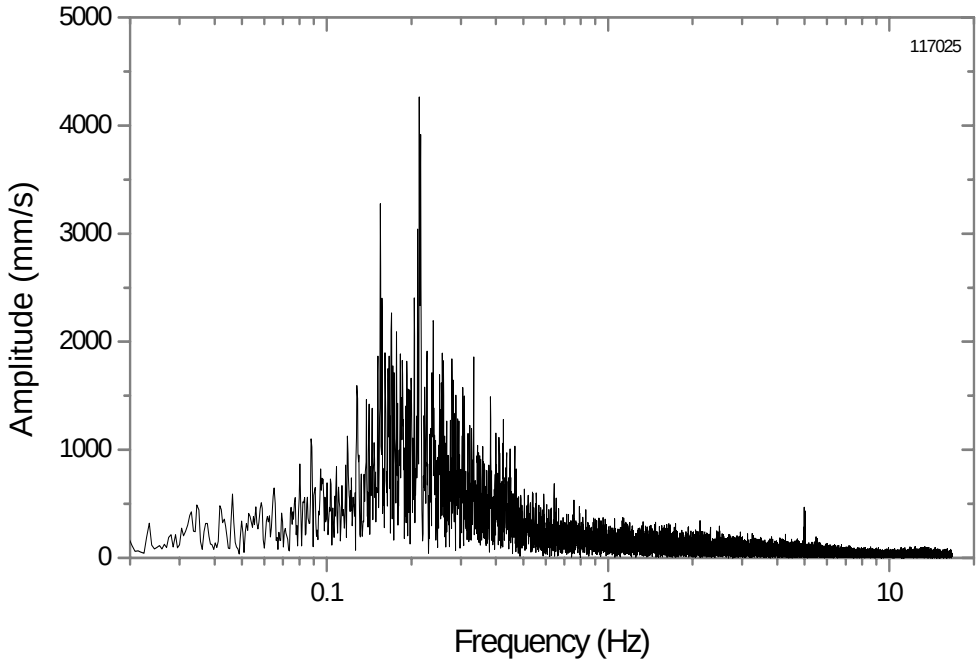

Figure A2.18: FFT Plot of Metal Level Fluctuation for Heat 117025.

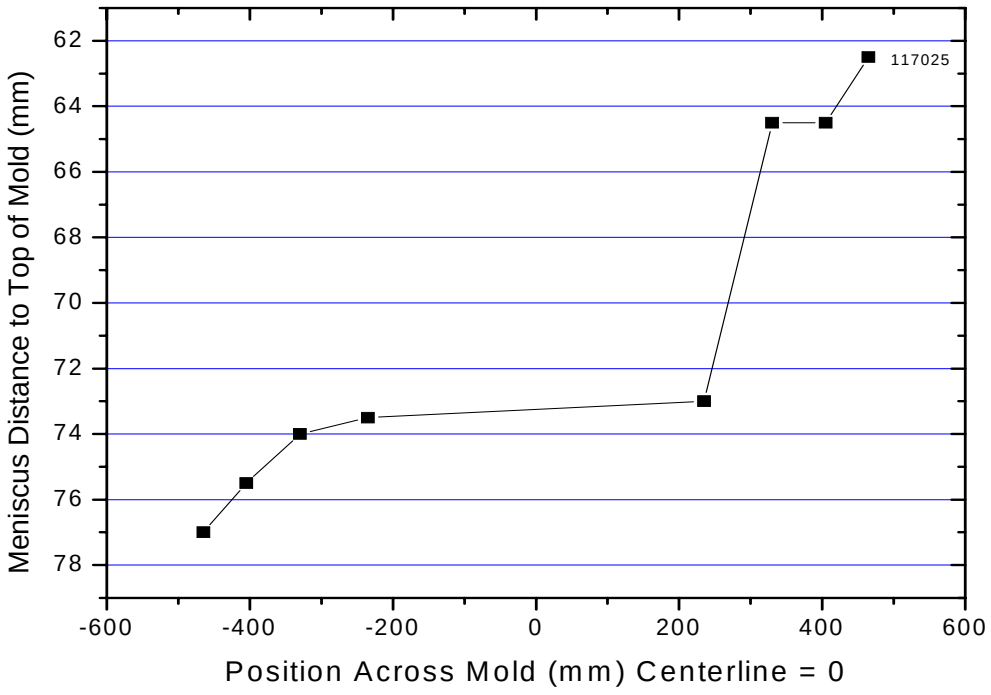

Figure A2.19: Meniscus Shape Profile for Heat 117025.

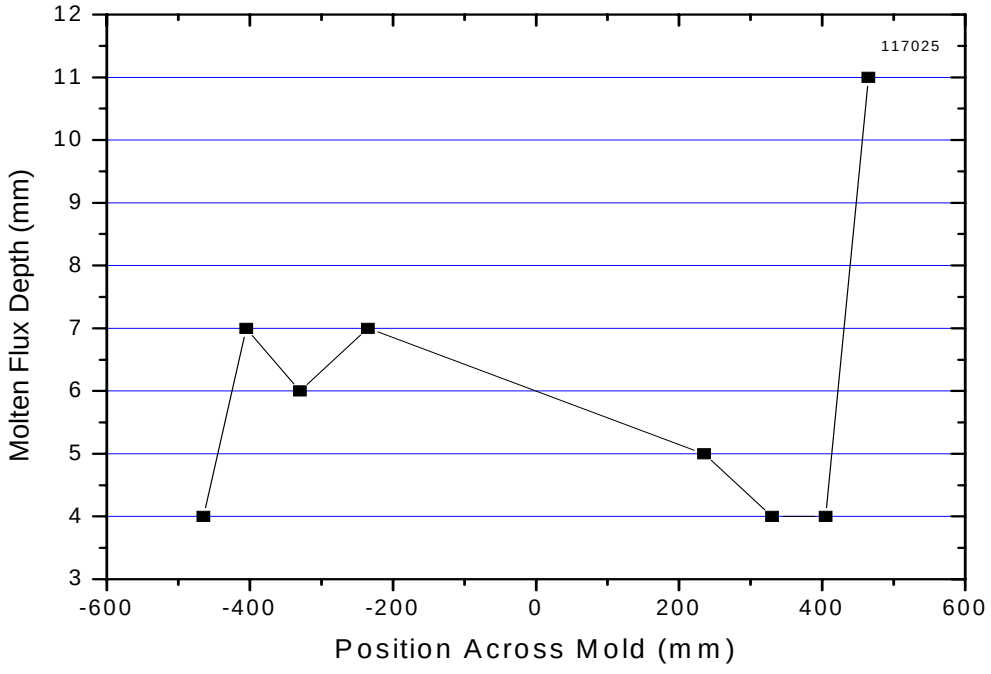

Figure A2.20: Molten Flux Depth Profile for Heat 117025.

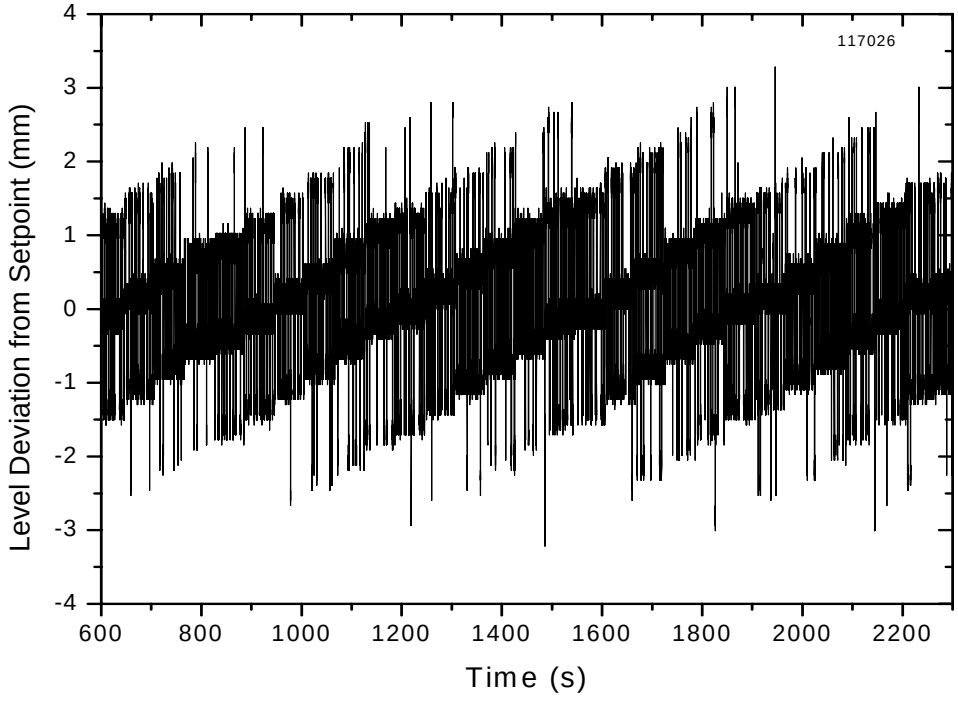

Figure A2.21: Plot of Metal Level Fluctuation from Setpoint for Heat 117026.

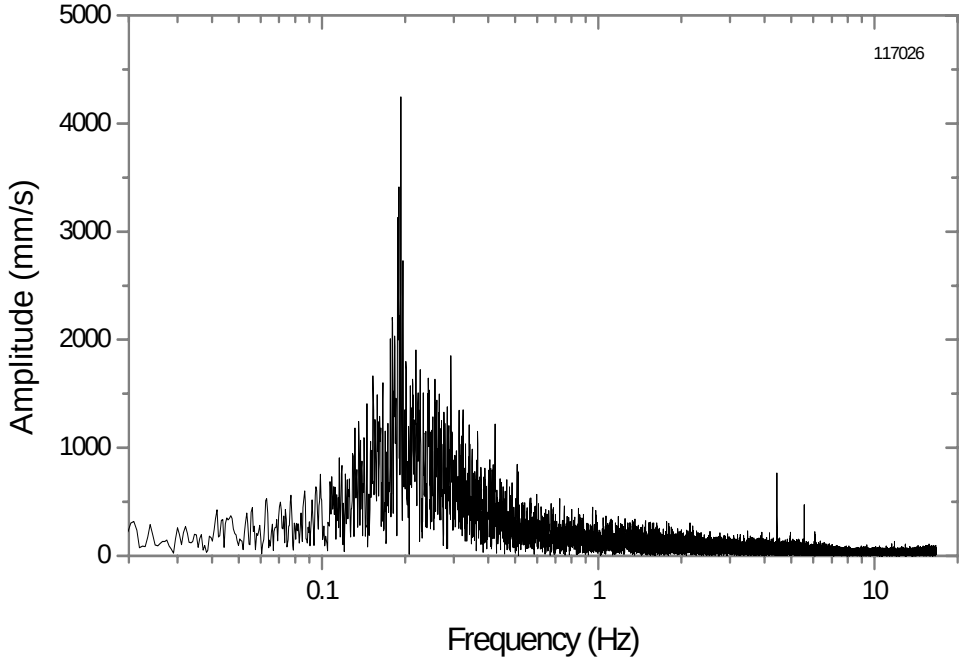

Figure A2.22: FFT Plot of Metal Level Fluctuation for Heat 117026.

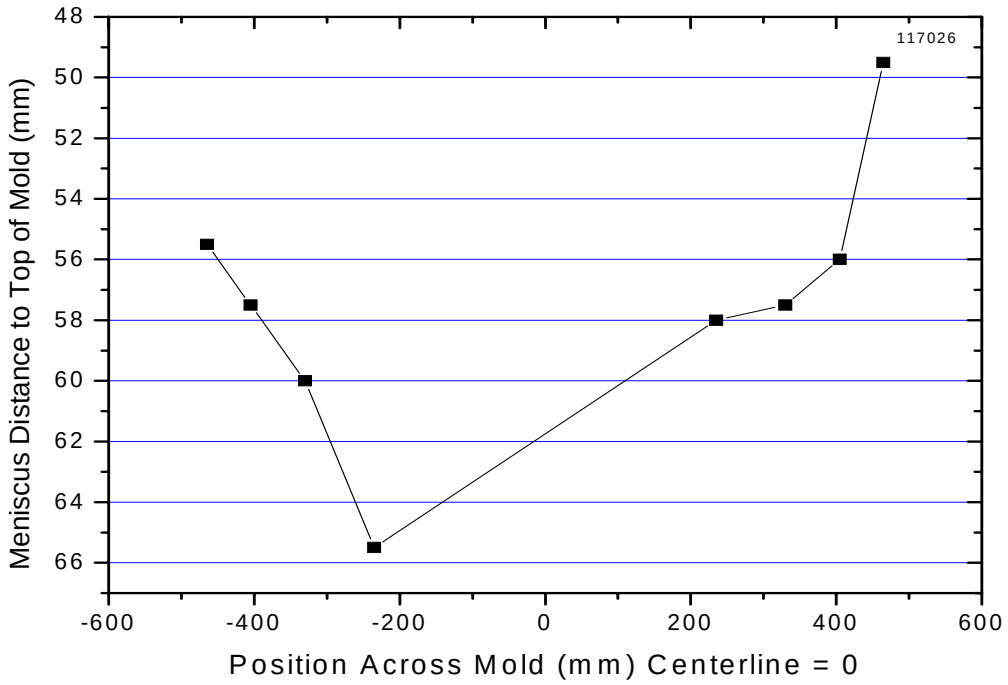

Figure A2.23: Meniscus Shape Profile for Heat 117026.

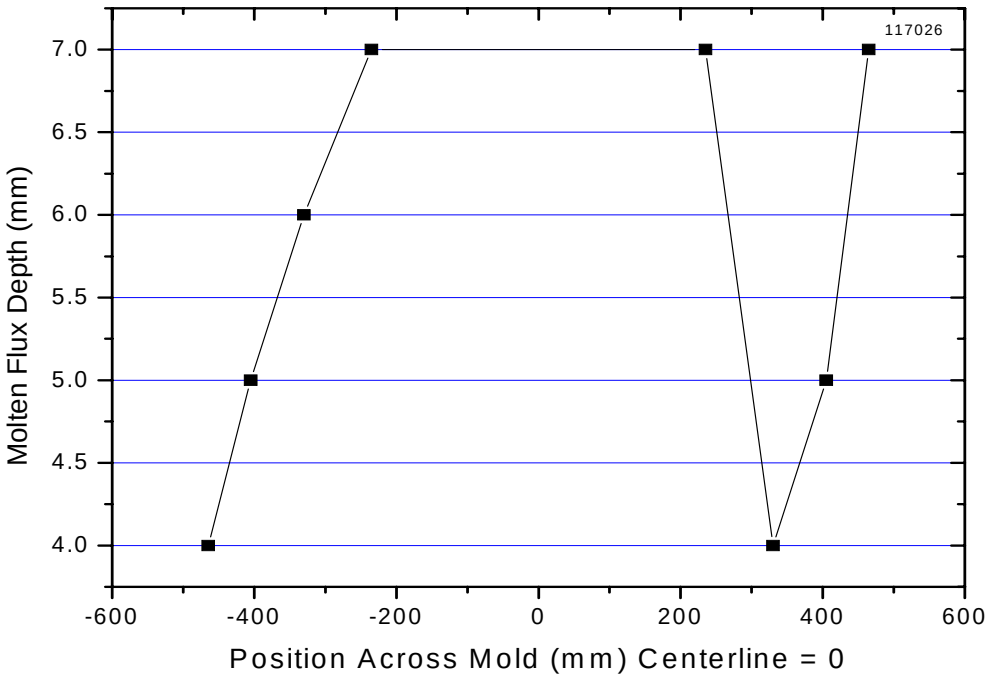

Figure A2.24: Molten Flux Depth Profile for Heat 117026.

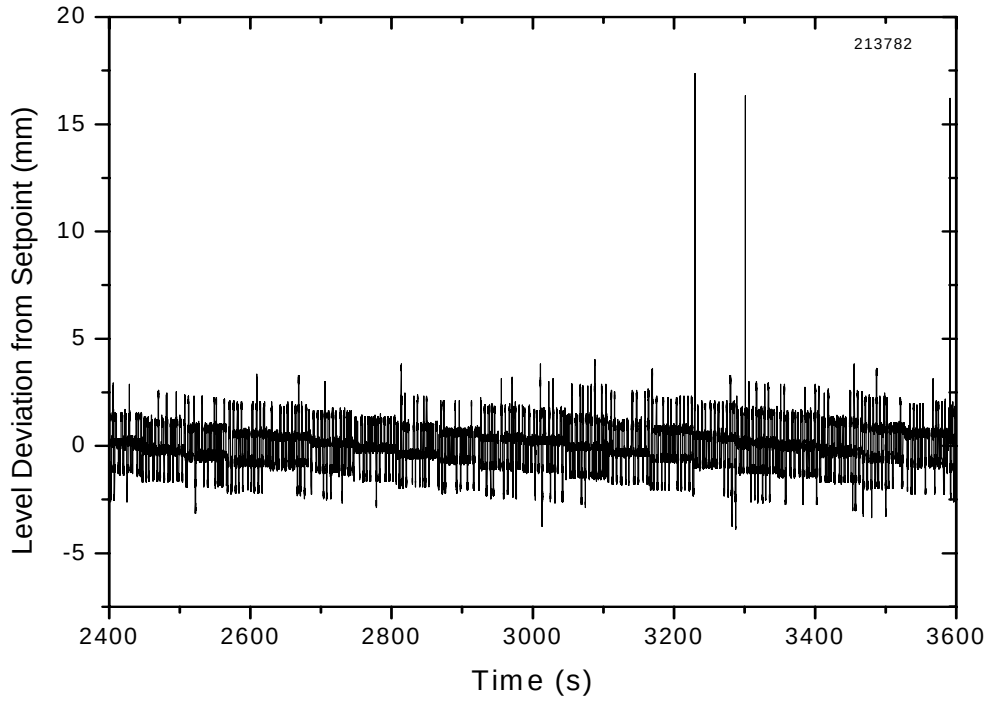

Figure A2.25: Plot of Metal Level Fluctuation from Setpoint for Heat 213782.

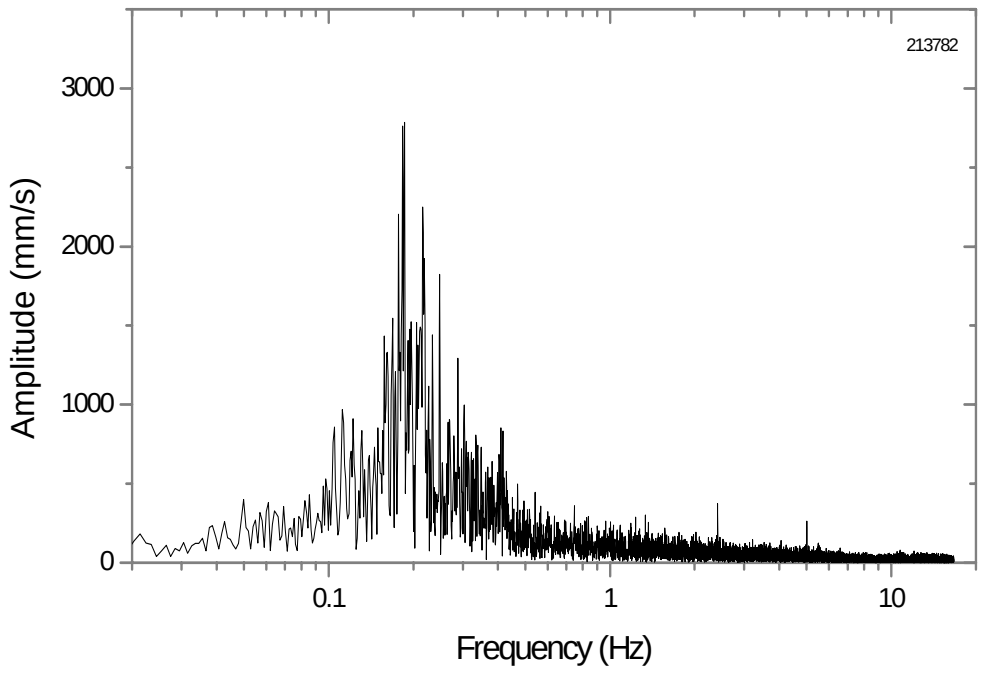

Figure A2.26: FFT Plot of Metal Level Fluctuation for Heat 213782.

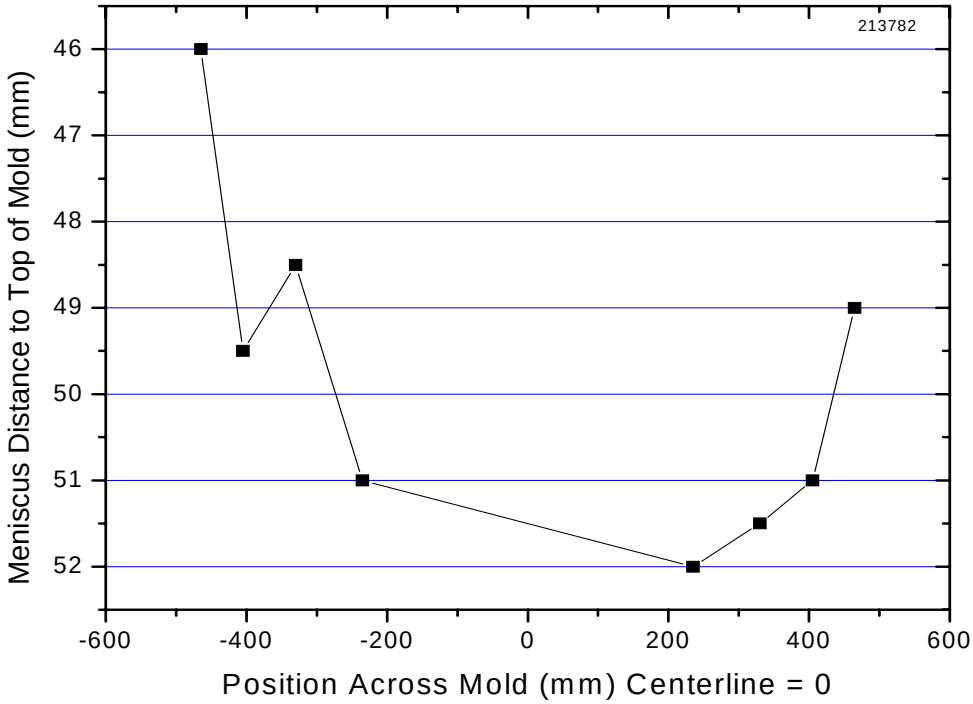

Figure A2.27: Meniscus Shape Profile for Heat 213782.

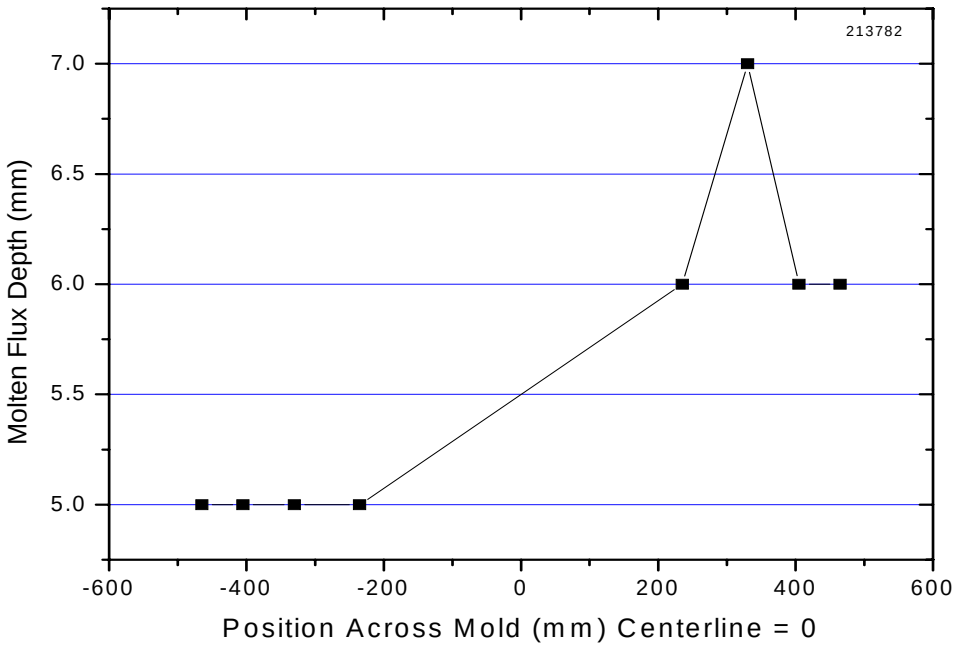

Figure A2.28: Molten Flux Depth Profile for Heat 213782.

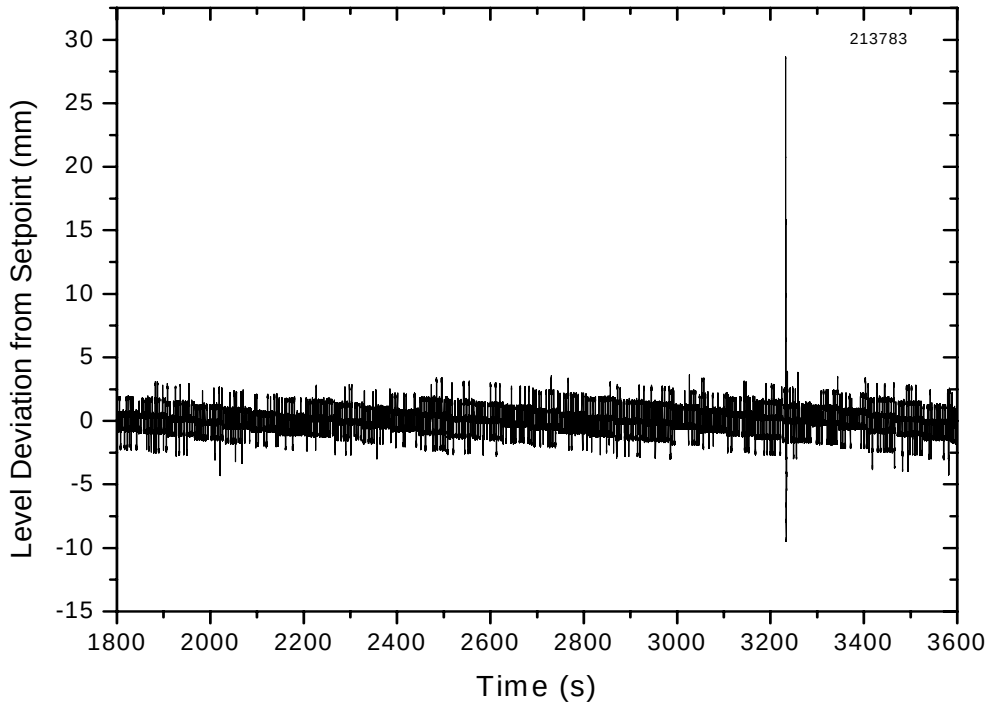

Figure A2.29: Plot of Metal Level Fluctuation for Heat 213783.

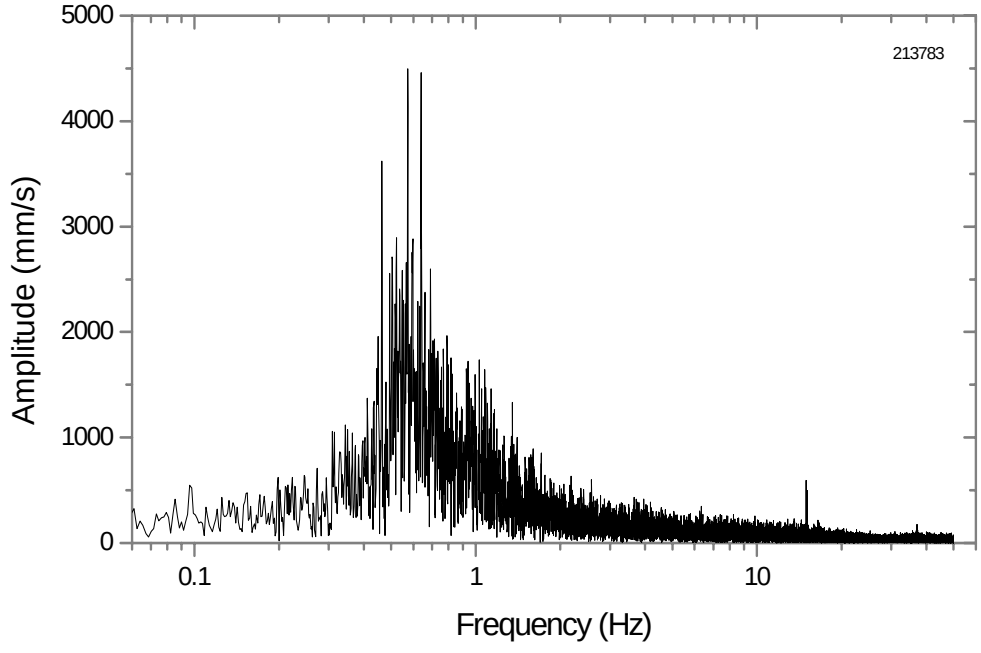

Figure A2.30: FFT Plot of Metal Level Fluctuation for Heat 213783.

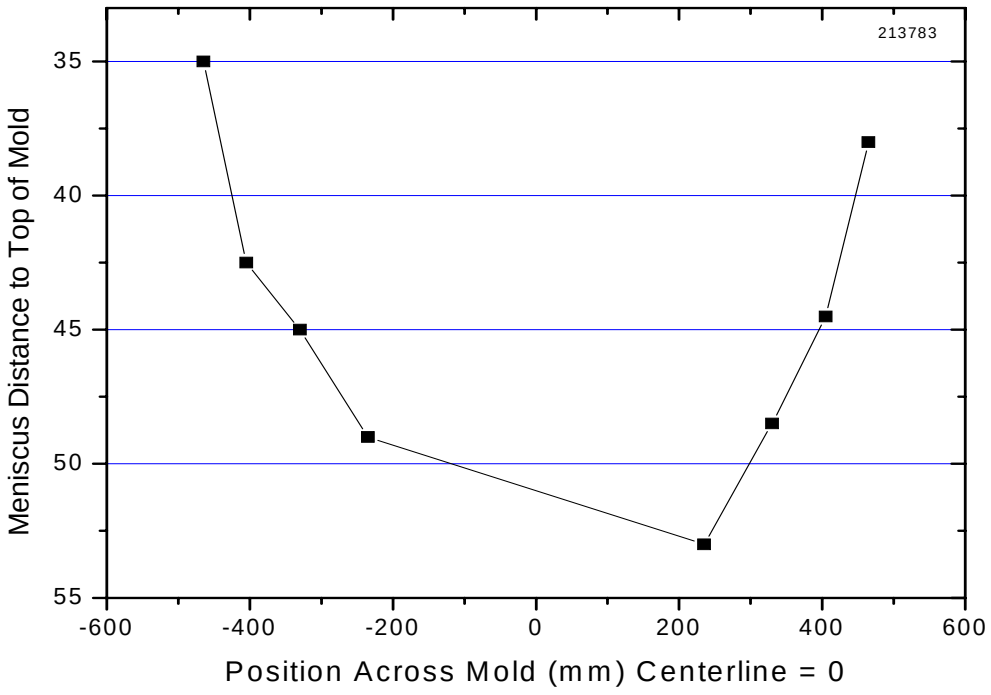

Figure A2.31: Meniscus Shape Profile for Heat 213783.

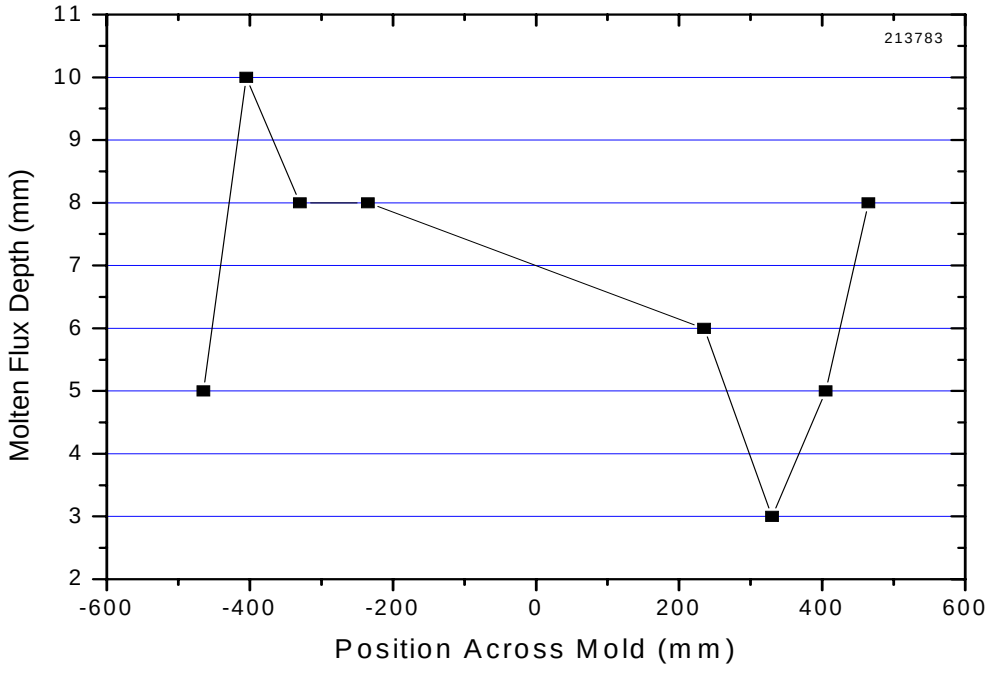

Figure A2.32: Molten Flux Depth Profile for Heat 213783.

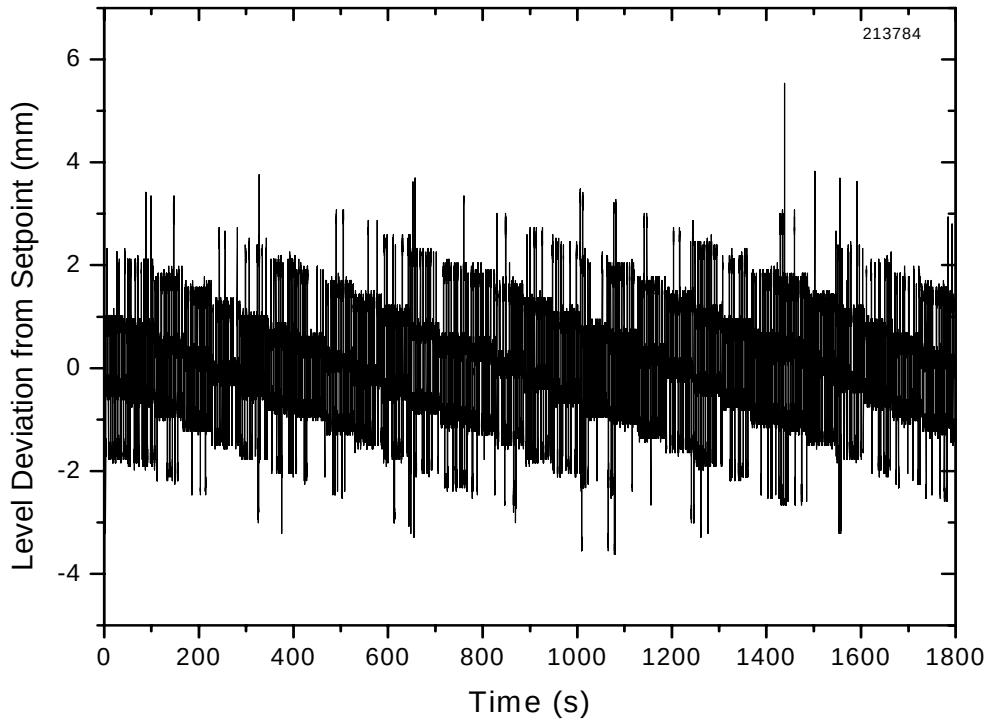

Figure A2.33: Plot of Metal Level Fluctuation from Setpoint for Heat 213784.

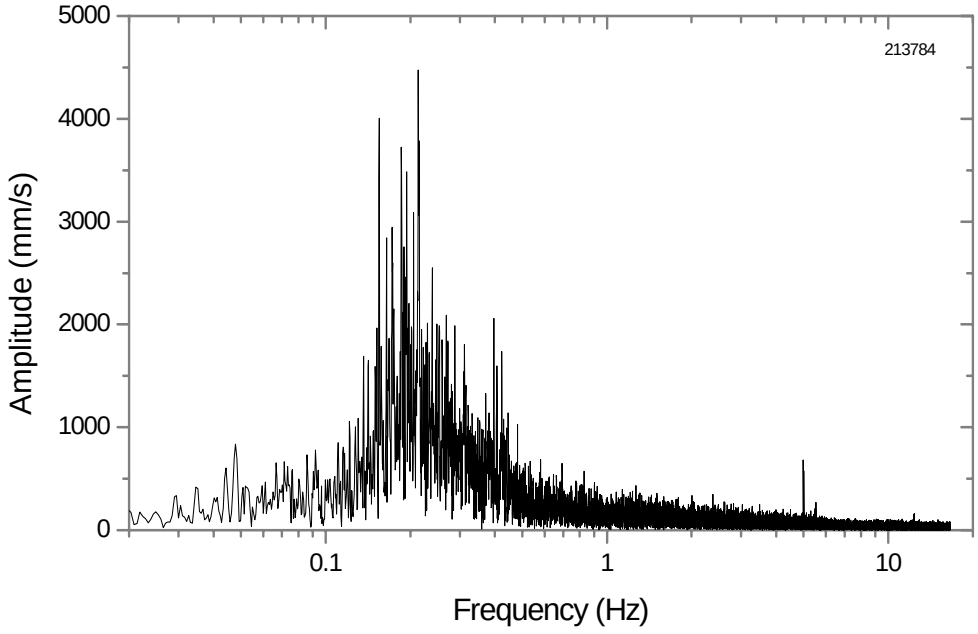

Figure A2.34: FFT Plot of Metal Level Fluctuation for Heat 213784.

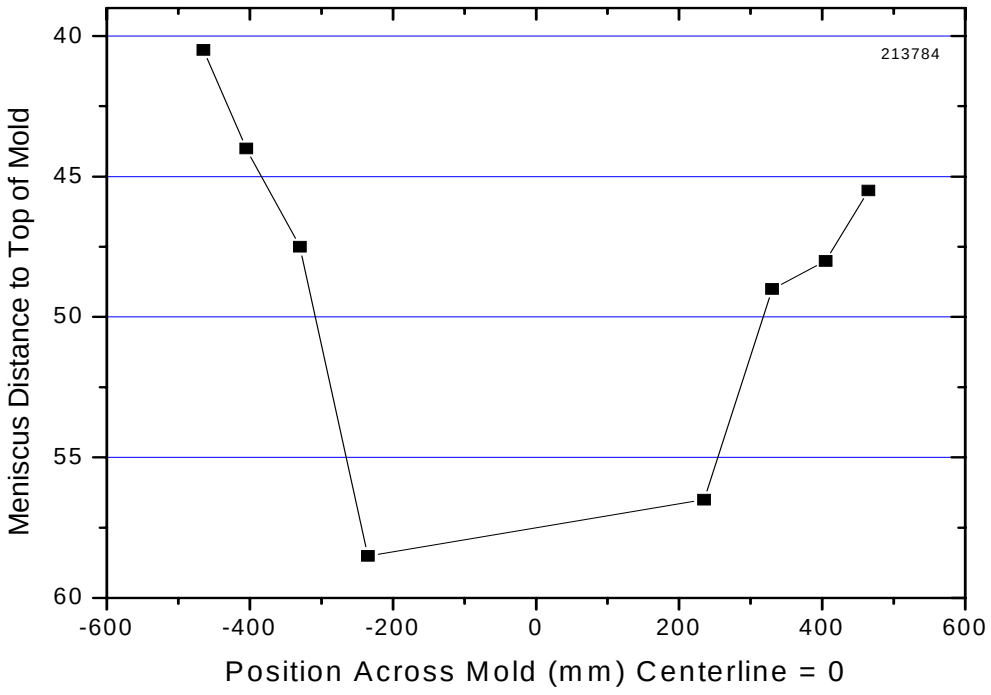

Figure A2.35: Meniscus Shape Profile for Heat 213784.

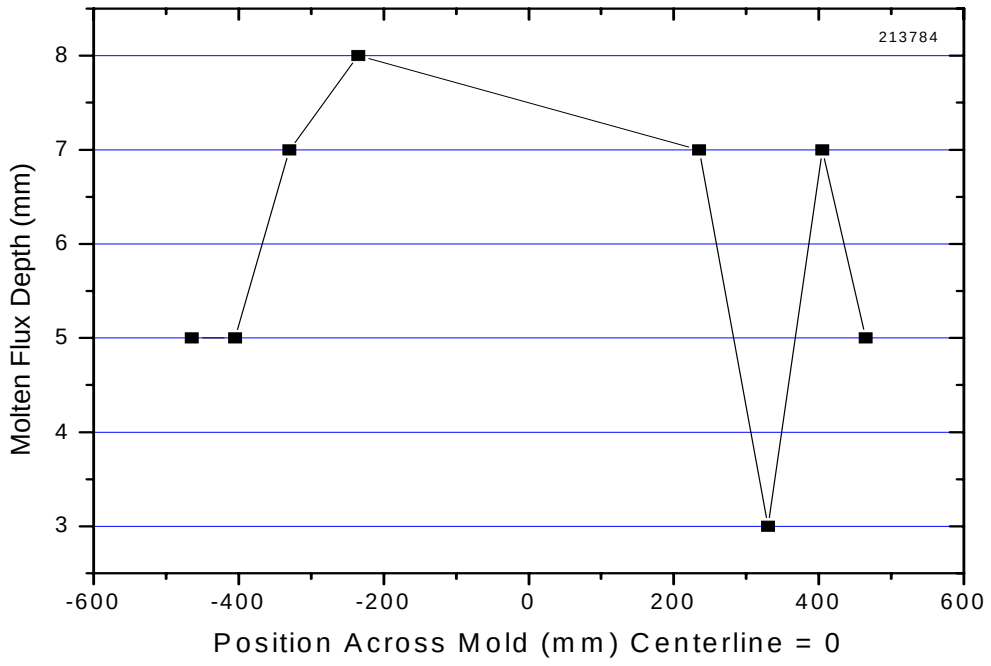

Figure A2.36: Molten Flux Depth Profile for Heat 213784.